ABSTRACT

Title of Document: NUMERICAL MODELING AND OPTIMIZATION OF SINGLE PHASE FLOW MANIFOLD-MICROCHANNEL PLATE HEAT EXCHANGER

Martinus Adrian Arie, Master of Science, 2012

Directed By: Professor Michael Ohadi, Mechanical Engineering

In recent years manifold-microchannel technology has received considerable attention from the research community as it has demonstrated clear advantage over state of the art heat exchangers. It has the potential to improve heat transfer performance by an order of magnitude while reducing pressure drop penalty equally impressive, when compared to state of the art heat exchangers for selected applications. However, design of heat exchangers based on this technology requires selection of several critical geometrical and flow parameters. This research focuses on the numerical modeling and an optimization algorithm to determine such design parameters and optimize the performance of manifold-microchannels for a plate heat exchanger geometry. A hybrid method was developed to calculate the total pumping power and heat transfer of this type of heat exchangers. The results from the hybrid method were successfully verified with the results obtained from a full CFD model and experimental work. Based on the hybrid method, a multi-objective optimization of the heat exchanger was conducted utilizing an approximation-based optimization

technique. The optimized manifold-microchannel flat plate heat exchanger showed superior performance over a Chevron plate heat exchanger which is a wildly used option for diverse applications.

NUMERICAL MODELING AND OPTIMIZATION OF SINGLE PHASE MANIFOLD-MICROCHANNEL PLATE HEAT EXCHANGER

By

Martinus Adrian Arie

Thesis submitted to the Faculty of the Graduate School of the
University of Maryland, College Park, in partial fulfillment
of the requirements for the degree of
Master of Science
2012

Advisory Committee:
Professor Michael Ohadi, Chair
Professor Bao Yang
Professor Marino DiMarzo

Dedication

To my parents who have helped, encouraged, and supported me always

Acknowledgements

First and foremost I would like to thank my advisor Dr. Michael Ohadi and my mentor Dr. Amir Shooshtari for their guidance, help, encouragement, and support for the completion of my research. I will always carry what I learned from them with me throughout the rest of my life.

I also would like to thank Dr. Serguei Dessiatoun and Dr. Ebrahim Al-Hajri for their guidance and support during my course of study and research.

I would like to express my gratitude to Dr. Vikrant Chandramohan Aute and Dr. Khaled Hassan Saleh for providing sampling code which was quite helpful for the completion of my research.

Lastly, I am also grateful to my friends at Smart and Small Thermal Systems Laboratory (S2TS), especially Rohit Andhare, Harish Ganapathy, Vibhash Chandra Jha, Meera Mahadevan, Raphael Mandel, David Boyea, Josh Fody, Sascha Steinmayer, Dr. Kyosung Choo, and Markus Grundhoff, for providing a constructive and peaceful environment and also their helpful tips and suggestions regarding my research.

Table of Contents

List of Tables

List of Figures

Nomenclature

A	cross section area [m^2]
a	constant defined in Eq. (22) [s/m]
b	constant defined in Eq. (22) [-]
c	constant defined in Eq. (43) [Ws/m^4K]
d	constant defined in Eq. (43) [W/m^3K]
C_p	specific heat constant [J/kgK]
D	hydraulics diameter [m]
F	a factor that govern uniformity of the heat transfer density [-]
$\dot{F}$	regression function for metamodel [-]
f	Fanning friction factor [-]
k	thermal conductivity [W/mK]
k_{eff}	effective thermal conductivity [W/mK]
g	gravity [m^2/s]
H	height [m]
I	unit tensor [-]
h	heat transfer coefficient [W/m^2K]
L	length [m]
$LMTD$	Log Mean Temperature Difference [K]
$\dot{m}$	mass flow rate [g/s]
MAE	mean absolute error [%]
N	total number of constraint [-]
Nx	number of passes [-]
Ny	number of manifold channel [-]
Nz	number of stack [-]
Nu	Nusselt number [-]
n	total number of microchannels for a single pass [-]
P	pumping power [W]
P/V	pumping power density [W/m^3]
P_r	Prandtl number [-]
p	pressure [Pa]
Δp	pressure drop [Pa]
$\mathbb{P}$	parameter [m]
Q	heat transfer rate [W]
$Q/V\Delta T$	heat transfer density [W/m^3K]
Re	Reynolds number [-]
r_p	penalty coefficient [-]
T	temperature [K]
ΔT	base & inlet channel temperature difference [K]
t	thickness [m]
V	volume [m^3]
v	velocity [m/s]
W	width [m]
x,y,z	Cartesian coordinate system [-]

Δx	length of the control volume [m]
$\dot{x}$	dependent variables that deduce the metamodel function [-]
$\dot{y}$	predicted model function from metamodel [-]
$\dot{z}$	random process for metamodel [-]

Greek Symbol

α	$W_{chn}$to t_{fin} ratio [-]
β	chevron angle [degree]
$\dot{\beta}$	regression parameter [-]
γ	aspect ratio between width and height of the manifold channel [-]
μ	dynamic viscosity [N s/m^2]
υ	kinematic viscosity [m^2/s]
ρ	density [kg/m^3]
τ	shear stress [N/m^2]
$\bar{\bar{\tau}}$	stress tensor [N/m^2]
ħ	enthalpy [J/kg]
φ	enlarge factor [-]

Subscript

1	manifold 1
2	manifold 2
base	microgroove base
cfd	Computational Fluid Dynamic
chn	microchannel
fin	fin
in	microchannel inlet
out	microchannel outlet
mnd	manifold
sc	single microchannel
spsm	single pass single manifold
tot	total
w	wall

Superscript

‘	normalize variable

Chapter 1: Introduction

1.1. Background

Heat exchanger is one of the important innovations in human history. The main use of heat exchanger is to transfer heat from one medium into another. One of the most wildly used type of heat exchangers is the one that is functioned to transport heat between two fluids. It has numerous industrial or residential applications. For example, it is applicable to water heaters, cooling towers, waste heat recovery systems, food industry, refrigeration, heating, ventilation, and air conditioning (HVAC) and many others. The most common of such heat exchanger is plate heat exchanger as shown in Figure 1.

Figure 1: Plate heat Exchanger [1]

The main advantage of plate heat exchanger compared to other types is by stacking multiple plates together, as shown in Figure 2(a), the heat transfer area can be increase which increases its capacity while preserving the compactness. In this type of heat exchanger fluid is supplied to every plate by a round manifold system

positioned at opposite corners of each plate as shown in Figure 2(a). Two type of fluid is supplied, cold fluid and hot fluid, where the hot fluid flow across the hot sides (colored red) and the cold fluid flow across the cold sides (colored blue). Heat is transfer from the hot fluid to the cold fluid by convection and conduction via a plate, Figure 2(b), which divides each side. The distance between successive plates is usually very small in order to create uniform flow distribution in both the hot and cold sides by having high pressure flow. The plate usually made of stainless steel because it is strong, high resistance to corrosion, and relatively easy to manufacture compared to nickel and copper. However, the plate can also be made of copper, nickel, or other types of materials depending on the heat exchanger applications. There is no limit on how many stacks a plate heat exchanger can has. It mainly depends on the desired capacity of heat exchanger.

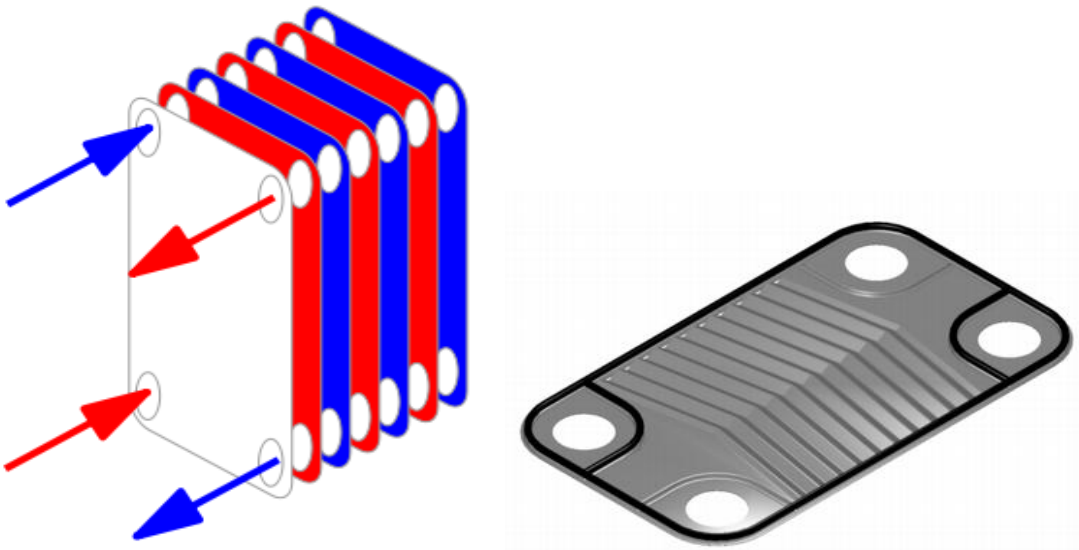

(a) (b)

Figure 2: **(a) Stacked plate heat exchanger [2], (b) A single plate of plate heat exchanger [3]**

1.2. Scope of Work

Despite its high heat capacity, the main disadvantage of plate heat exchanger is its high pumping power requirement due to a long and narrow flow path. The main focus of this study is to address this issue by development of a new plate heat exchanger design which is able to reduce the overall pumping power of the heat exchanger for the same or higher heat transfer performance through utilization of manifold-microchannel technology.

Manifold-microchannel technology takes advantage of good feature of microchannels while providing a manifold for precise flow distribution in the channels. By shrinking the channel dimensions into micron size, the heat transfer in microchannels is enhanced due to the increase in heat transfer area to volume ratio. A typical microchannel heat exchanger consists of a base and finned surface as shown in Figure 3. However, reduction in channel cross section area also increases the pressure drop which in turn increases pumping power.

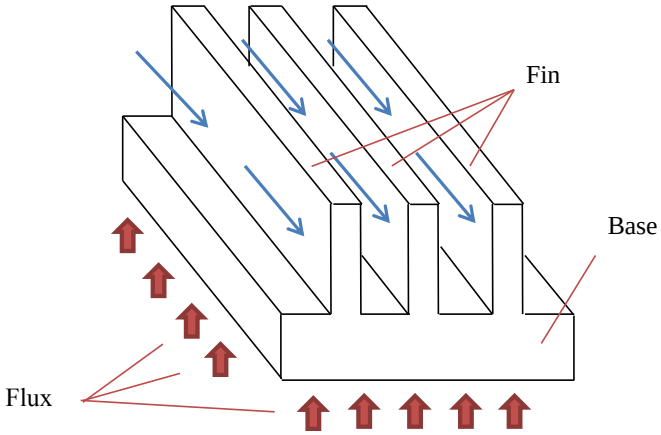

Figure 3: Microchannel heat exchanger

Manifold-microchannel technology can be implemented by adding a set of manifolds over the fins as shown in Figure 4. The flow enters via manifold channels, and then is distributed across microchannels where the major heat transfer takes place, and then travels back to the manifold channels as shown in Figure 4(b).

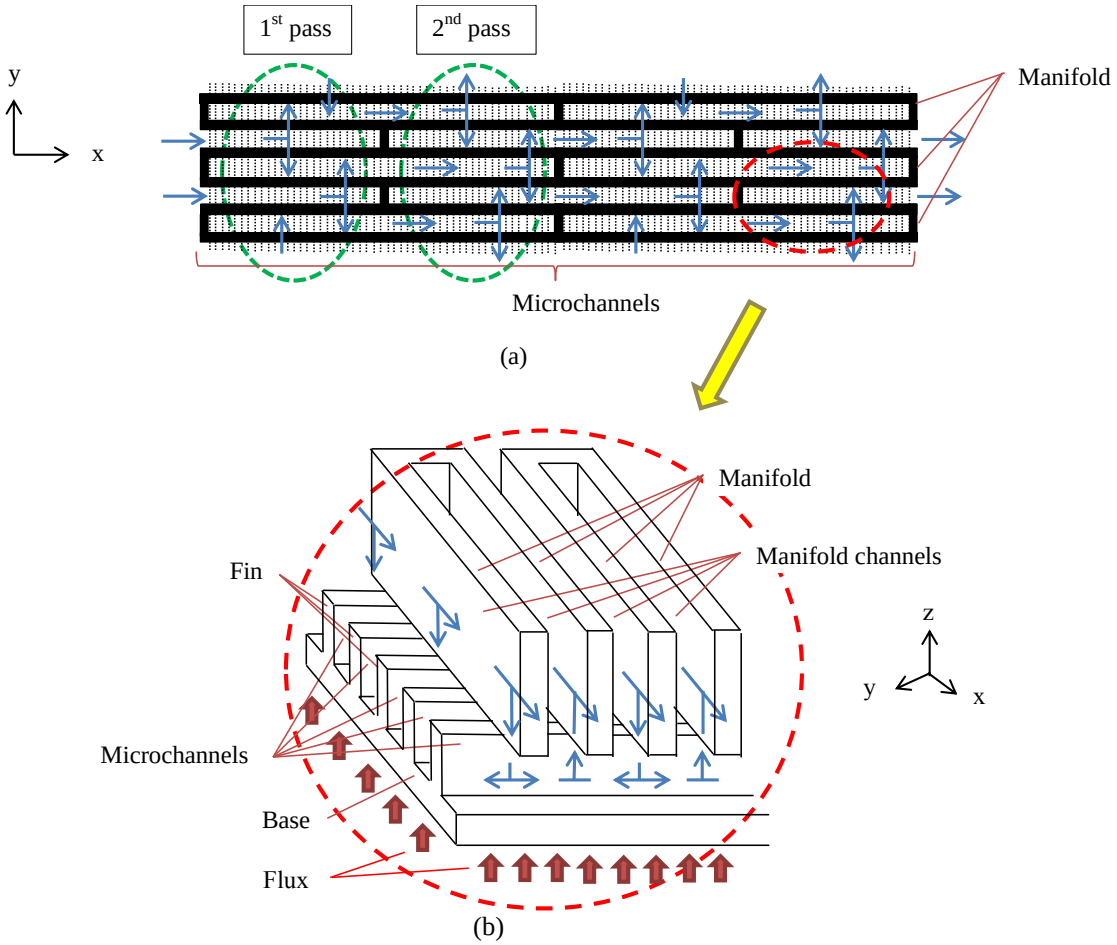

Figure 4: Manifold-microchannel plate heat exchanger: (a) Top view, (b) 3-D view

The flow at the manifold is further divided into multiple passes, as shown in Figure 4(a). The main purpose is to improve the uniformity of ΔT which is the Temperature difference between the inlet fluid temperature and microgroove base temperature ($\Delta T = T_{base} - T_{in}$) which in turn can improve the effectiveness of the heat

exchanger. Detailed literature survey of microchannel and manifold-microchannel will be presented in chapter 2.

In the past the manifold-microchannel technology has been successfully tested to deliver lower pumping power compared to traditional design for the same or higher heat transfer performance. It has also been shown that by separating the flow into shorter channels while keeping the sum of the lengths of the channels equal to the length of a conventional channel, pressure drop can be reduced by a factor of n^2, where n is the number of channel feeds. In addition, by dividing the flow into multiple passes and reducing the flow path length, the flow can redevelop which increase heat transfer due to the fact that developing flow has higher heat transfer [4].

Design of heat exchangers based on manifold-microchannel technology requires selection of several geometrical and flow parameters. In order to take advantage of the full potential of this technology, these parameters must be optimized properly. The current research includes development of a multi-objective optimization method for manifold-microchannel heat exchangers to determine the optimum parameters which yield maximum heat transfer and minimum pumping power.

The optimization process requires sample-testing of multiple heat exchanger designs to determine the optimum configuration. Performing multiple testing on manifold-microchannel heat exchanger experimentally requires tremendous amount of time and resources to manufacture multiple heat exchangers. However, CFD modeling software has become quite advanced in the past few years and makes it possible to simulate complex structures with high degree of accuracy. As a result, CFD

simulation is the preferred choice for sampling multiple manifold-microchannel heat exchangers.

Modeling a manifold-microchannel plate heat exchanger requires to consider both the manifold and microchannel sections due to interdependency of the flow in both sections. In addition, the pressure drop in the manifold also needs to be evaluated to calculate total pumping power of the system. This causes the full scale modeling process become challenging and requiring long computational time, especially for cases with large number of microchannels. Therefore, a numerical method which is able to simplify the problem and make it computationally feasible has to be developed.

1.3. Research Objectives

The main objective of this study is to develop a numerical optimization method which is able to predict the optimum performance of the manifold-microchannel plate heat exchanger by determining the optimum geometry and flow parameters and from there identifying their optimum range. For heat exchanger design, there are three main variables which determine its performance: heat transfer rate (Q), pumping power (P), and volume (V). Higher heat transfer rate is preferred for any heat exchanger. On the other hand, minimum volume and pumping power are preferred in order to minimize production and operation costs and increase system compactness.

Three-objective optimization is very complex and computationally expensive. A reduction in the number of objective functions can be achieved by defining the

objective functions as the ratios of heat transfer rate and pumping power to the volume of the manifold-microchannel. In addition, heat transfer rate depends on the temperature boundary condition imposed (i.e. ΔT). Therefore, it is more appropriate to divide heat transfer rate by the temperature difference. With this adjustment, the new optimization objectives now are to maximize ($Q/(V\Delta T)$) and minimize (P/V). For simplicity these two terms are called heat transfer density and pumping power density, respectively, from here on.

In order to accomplish the main objective, another objective to develop a numerical method which is able to predict heat transfer density and pumping power density of manifold-microchannel plate heat exchanger in a short computational time needs to be defined. This objective is very important for the broader goal of the project because as mentioned in the previous section, the full heat exchanger CFD simulation will require significant computational time. In addition, in order to perform multi-objective optimization, hundreds of simulation run are needed which make the problem become infeasible to be solve due to long computational time. Therefore, it is essential to develop a method that while computationally affordable, it can predict the thermal and hydrodynamic performance of the manifold-microchannel heat exchanger.

1.4. Approach

To speed up the optimization process, a numerical method which is able to quickly predict the performance of manifold-microchannel plate heat exchanger was developed. The method is an expansion of the work by Maharudrayya et al. [5] which

was originally developed for modeling of flow in a manifold attached to a number of long straight channels. The current manifold flow model considers the effect of U-shape flow in short microchannels and in combination with CFD microchannel models, it estimates the heat transfer and pressure drop of entire manifold-microchannel heat exchanger and can be applicable for high number of microchannels. A detailed description on the method will be described in chapter 3.

For the multi-objective optimization, a metamodel based optimization was implemented. The method includes a sampling process which utilizes the numerical method developed before, a metamodel to predict the behavior of the function from the sampling results, and a multi-objective optimization to calculate the optimum performance using the metamodel results. A detailed description on the optimization method will be described on chapter 4.

The outline of this thesis is as follow: Chapter 2 of the thesis provides an introduction to the manifold microchannel plate heat exchangers and heat exchanger optimization, followed by detailed survey of the relevant literature. Chapter 3 discusses the numerical method to calculate heat transfer density and pumping power density. The explanation of the optimization method employed in this study is given in Chapter 4 and are followed by the details of optimization results and discussion in chapter 5. This includes comparison of the results with chevron plate heat exchanger and validation of the numerical method by CFD simulation and experimental work. Conclusions and future work are discussed in chapter 6 of the thesis.

Chapter 2: Literature Study

2.1. Introduction to Plate Heat Exchanger

The study of plate heat exchanger has been started as early as 1878 by Dracehe from Germany or by Malvezia from France in 1895 [6]. However, the first commercially successful design was achieved by Dr. Richard Seligman in 1923 [7]. Ever since plate heat exchangers have been studied thoughtfully due to its numerous applications, compactness and high heat transfer performance. Some of the earlier work related to plate heat exchanger will be discussed in this section.

One of the early works to study the performance of plate heat exchanger was carried out by McKillop and Dunkley who developed a correlation to determine heat transfer coefficient of plate heat exchanger [8]. Another work worth mentioning was by Tauscher and Mayinger who successfully enhanced heat transfer in plate heat exchanger by adding rib roughened surface and reported that with this improvement Nusselt number (Nu) up to 50 and pressure drop less than 80Pa is possible [9]. Several type of plate heat exchanger has been developed such as chevron, corrugated, and many others [10].

Muley and Manglik have shown that for chevron plate heat exchangers, increasing chevron angle (β) can increase Nu up to a factor of 3 with a price of increase in friction factor (f) up to a factor of 9 [11]. Similarly, Gherasim et al. studied heat transfer and pressure drop on chevron plate heat exchanger and reported Nu between 30 and 50 and f between 3 and 10 are possible for Reynold number (Re) between 400 and 1400 [12, 13].

Khan et al. studied heat transfer on corrugated plate heat exchanger and reported higher Nu than chevron plate due to larger heat transfer surface area and increased in turbulence level [14]. The Nu range is reported between 20 and 160 for Re between 400 and 2500 for three difference Chevron angles. In another study, Luan et al. present a new corrugated heat exchanger design and reported that up to 50% reduction on flow resistance is possible with price of 25% reduction in heat transfer coefficient compared to chevron heat exchanger [15].

Durmuş et al. investigated heat transfer and pressure drop in three difference type of plate heat exchangers: flat, asterisks, and corrugated and conclude that corrugated plate heat exchanger performed best in term of heat transfer, but yield the highest pressure drop while flat plate heat exchanger has the poorest performance, but has the lowest pressure drop [16].

Abu-Khader reported a summary of the recent advances of plate heat exchanger including their thermal and hydrodynamic characteristics, two-phase performances, fouling, and corrosion in plate HX [10]. In addition, Ayub has summarized several earlier works on analytical correlations of Nu and f for plate heat exchanger [17].

All of the plate heat exchangers share the same disadvantage which is high operational pumping power due to a long and restricted flow path causing large pressure drops. In order to reduce pumping power while keeping heat transfer optimum, manifold-microchannel technology has been introduced. The literature survey on manifold-microchannel technology will be presented in the next section.

2.2. Introduction to Manifold-microchannel Heat Exchanger

Manifold-microchannel heat exchangers can be perceived as offspring of microchannel heat exchangers. The application of microchannel in heat exchangers was first proposed by Tuckerman and Pease in 1983 [18]. Since then microchannel heat exchangers have been studied thoroughly due to their high heat transfer capability. The summary on microchannel technology development was reported by Phillips for technology up to 1990 [19], by Hassan et al. for technology from 1990 up to date [20], and by Khan and Fartaj from 1983 up to date [21].

Manifold-microchannel technology was first studied by Harpole and Eninger in 1991 who found that heat transfer coefficient in the order of 100W/cm^{2}K and pumping power of 1 or 2 bar is possible for laminar flow in a manifold-microchannel heat exchanger [22]. Since then, there have been multiple studies on manifold-microchannel heat exchangers mostly for electronic cooling applications. However, most of the previous studies focused on small scale designs where the flow was entering from top of the manifold, as shown in Figure 5, while for larger scale manifold-microchannel plate heat exchanger the flow has to enter from the side as shown in Figure 4. In addition, most of those modeling works on the manifold-microchannel heat exchanger only considered modeling a single microchannel segment which typically consisted of microchannel, fin, and base, as shown in Figure 6 [23-25] or only a single manifold-microchannel segment which consist of microchannel, fin, base, manifold channel inlet and outlet, as shown in Figure 7, [4, 26]. This simplification is possible due to symmetry condition on all microchannel

and manifold channel for the case of top flow entrance configuration. Several works based on this configuration will be discussed next.

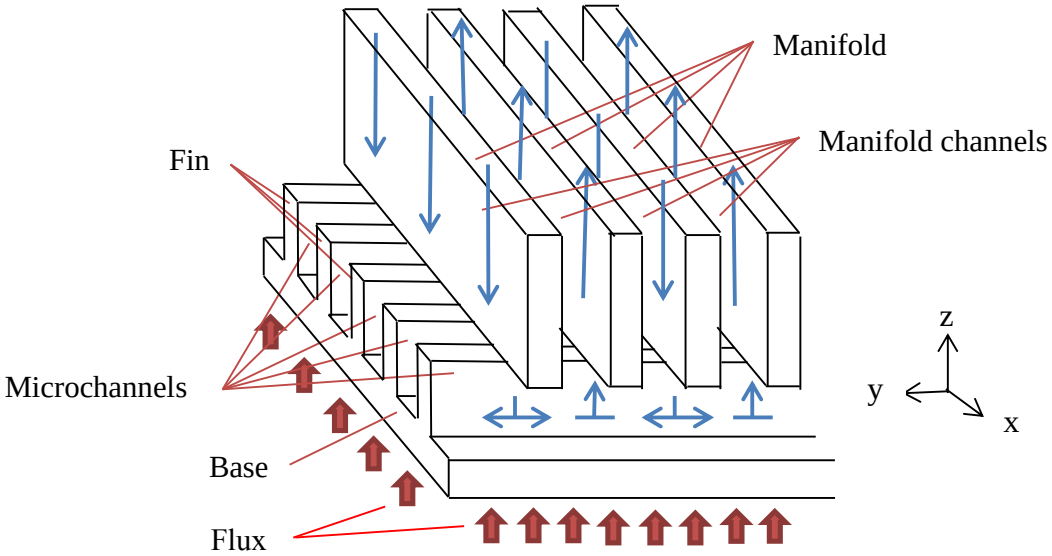

Figure 5: Manifold-microchannel heat exchanger with flow entrance from top of the manifold

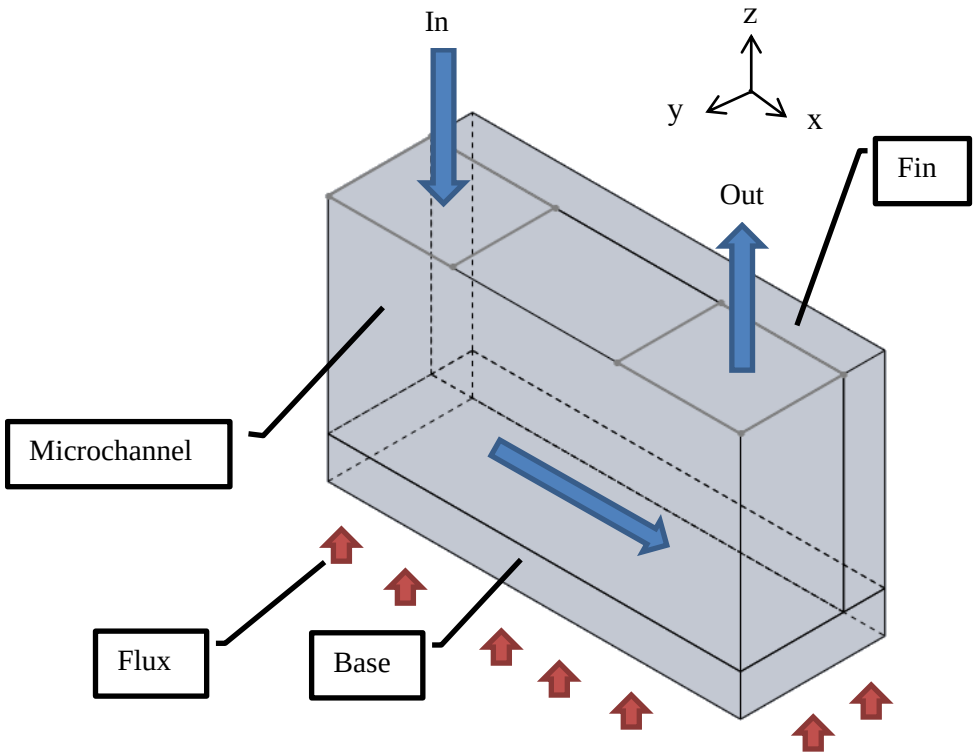

Figure 6: Single microchannel segment (For top flow entrance)

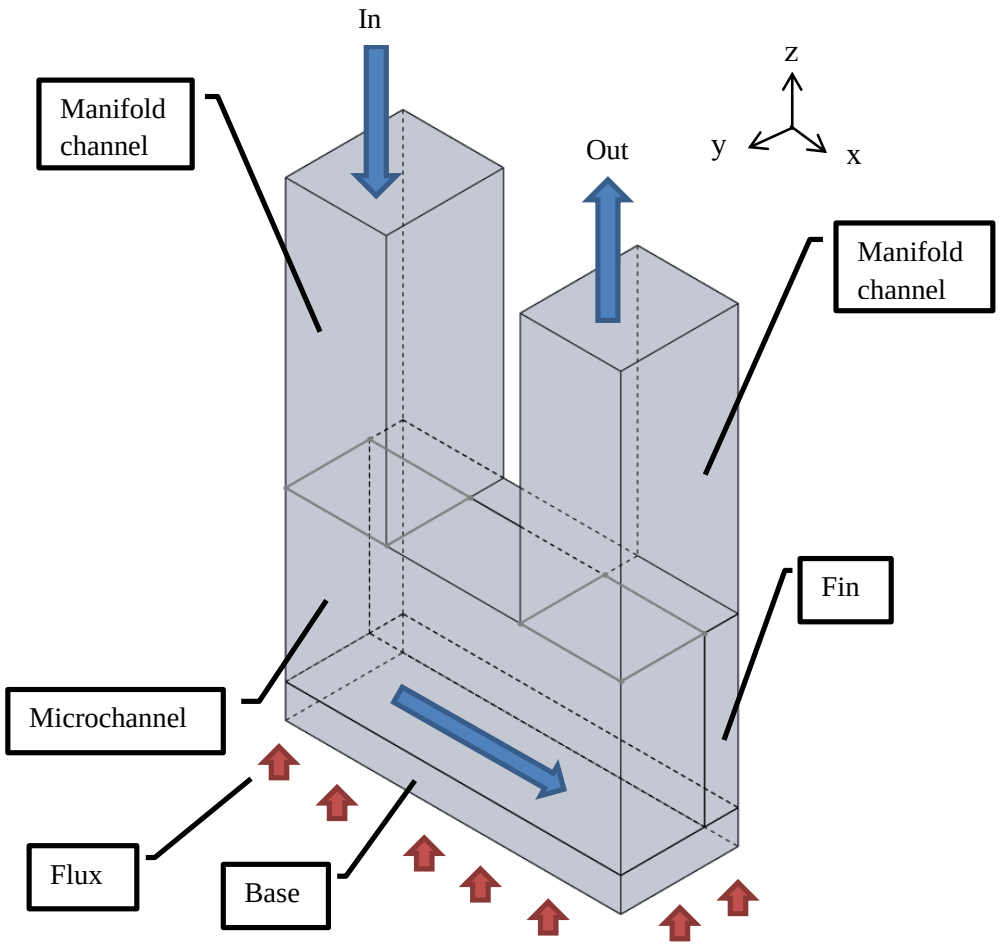

Figure 7: Single manifold-microchannel segment (For top flow entrance)

Copeland et al. conducted a 3-D CFD simulation on manifold-microchannel heat sink using water as working fluid and silicon fin and base [23]. The model only considered a single microchannel and assumed uniform laminar flow distribution in all channels. Pressure drop in the range of 47 - 12,260 Pa and thermal resistance of 0.25 - 1.85^{o}C/W were observed.

Ng and Poh also carried out a 3-D CFD simulation on manifold-microchannel heat sink considering only a single microchannel and assuming uniform laminar flow distribution in all channels [24, 25]. Water as working fluid and silicon fin and base were used. A parametric study was performed to investigate the effect of geometrical

and flow properties on Nu, f, pressure drop, and thermal resistance. Pressure drop between 45 - 10,209Pa and thermal resistance of 0.53 - 6.66^{o}C/W were observed.

Cetegen conducted 3-D numerical multi-objective optimization of manifold-microchannel heat sink [4]. The simulation considers a single manifold-microchannel segment. The inlet and outlet manifold channels provided better flow distribution in the inlet and outlet of the microchannel. Copper and water were used as fin material and working fluid. The result shows that manifold-microchannel heat sink can have 72% higher heat transfer coefficient than traditional microchannel heat sink or 306% higher than jet impingement heat sink for the same pumping power.

Ryu et al. also conducted a 3-D numerical optimization of manifold-microchannel heat sink by optimizing heat transfer coefficient using CFD simulation [26]. The simulation only considered a single manifold-microchannel segment. Copper and water were used as fin material and working fluid. The results showed that manifold-microchannel can minimize thermal resistance by half compared to traditional microchannel heat sink and improve temperature uniformity on the channel. However, no work on optimizing pumping power or pressure drop was presented.

Kim et al. did experimental testing on manifold-microchannel for forced air cooling using a full model consists of manifold and multiple microchannels [27]. Fin and base is made of silicon and air is used as working fluid with laminar flow configuration. The experiment revealed that 35% reduction on thermal resistance compared to microchannel heat sink is possible.

In the case of manifold-microchannel with side entrance flow, as shown in Figure 6, both manifold and microchannel need to be modeled due to coupled relation between manifold and microchannel. In addition, in order to correctly calculate the pressure drop in the manifold all of the microchannel need to be modeled since the flow in manifold is no longer symmetric. A number of works have been done to simulate this problem with using CFD, but those works are only limited to low number of microchannel (n). Some of these works will be discussed in the following.

Wang et al. performed a 3-D CFD simulation on both the manifold and microchannel section of the heat exchanger for 30 numbers of microchannels using copper fin and water as working fluid [28]. The result showed that manifold-microchannel design could increase heat transfer by 75% and delivered better temperature distribution compared to microchannel heat sink.

Kermani et al. did an experimental study on a manifold microchannel heat sink using water as working fluid and silicon as fin and base material for cooling concentrated solar cells [29]. The experiment found that heat transfer coefficient of 65.5kW/m^{2}K can be achieved for flow rate of 1.1g/s and heat flux of 75W/cm^2.

Escher et al. conducted an experimental and numerical work on manifold-microchannel heat sink using water as working fluid and silicon as fin and base material [30]. In order to simplify the modeling problem, the microchannel section was considered as porous media with an anisotropic permeability to account for resistant due to microchannel. The result of the simulation to some degree agreed

with experimental results and Thermal Resistance of 0.09 cm^2K/W with corresponding pressure drop of 0.22bar is possible for a system on a 2 x 2 cm^2.

Boteler et al. carried out a CFD numerical investigation on single pass plate manifold microchannel heat exchanger with considering both the manifold and microchannel section for 2 to 20 number of microchannel [31]. The fin and base were made of silicon and water was used as working fluid. The result showed that manifold-microchannel heat exchanger yield 97% reduction on pressure drop and better temperature distribution compared to conventional microchannel heat sink.

2.3. Introduction to Heat Exchanger Optimization

Numerous heat exchanger optimization efforts with different objectives and optimization methods have been reported in literature. A summary of selected works are presented here.

Ryu et al. conducted single-objective heat sink optimization to minimize thermal resistance using random search technique with optimization variables consisting of channel width, fin width, channel height, and pressure drop [32].

Gopinath et al. conducted multi-objective optimization of heat sink to find the optimum chips spacing which yield minimum junction temperature and length using genetic algorithm [33].

Sharma et al. conducted multi-objective optimization of heat sink to minimize failure rate and exergy destruction utilizing exergy based optimization with optimization variables of inlet flow velocity and temperature [34].

Türkakar and Okutucu-Özyurt conducted single-objective optimization on a microchannel heat sink to minimize thermal resistance with optimization variables of pumping power, channel width, and fin width using analytical optimization model [35].

Some of the heat exchanger optimization works utilized metamodel based optimization to save computation time. A selected number of these works will be explained below.

Amanifard et al. conducted multi-objective optimization on microchannels to maximize (Nu) and minimize pressure drop [36]. Three optimization variables were considered: the aspect ratio between channel height and hydraulic diameter, the aspect ratio between heat exchanger height and hydraulic diameter, and Re. The optimization was performed by applying a neural network based metamodel and genetic algorithm for multi-objective optimization.

Husain and Kim conducted multi-objective microchannel heat sink optimization to minimize thermal resistance and pumping power [37]. A response surface approximation base method was incorporated for metamodel and evolutionary algorithm based method was used for multi-objective optimization. The ratio of

channel width to channel height and ratio of fin width to channel height were considered as optimization variable.

Moreover, Husain and Kim also conducted multi-objective optimization utilizing multiple surrogate base metamodel: Kriging, neural network, and response surface approximation in conjugate with evolutionary algorithm based multi-objective optimization [38]. In this study three geometrical aspect ratio were considered as optimization variable with the objective to minimize thermal resistance and pumping power.

Saleh et al. carry out multi-objective microchannel heat sink optimization to minimize maximum channel temperature and maximizing heat density [39]. Kriging based metamodel and genetic algorithm were used for optimization. Flow velocity, 3 geometrical variables, and 3 thermal variables were considered as optimization variables.

For the problem of manifold-microchannel plate heat exchanger optimization with sidewise flow inlet, Figure 4, there is no such work was done in the literature. The closes work was for optimization of manifold-microchannel heat exchanger with top flow configuration, Figure 5, like done by Cetegen [4]. The optimization objective is to maximize heat transfer coefficient and minimize pumping power with optimization variables of 4 geometrical variables and inlet flow rate. Kriging based metamodel and genetic algorithm were used for the multi-objective optimization. For this case the problem is much simpler due to symmetry in both manifold and microchannel which require only simulate a single manifold-microchannel section as shown in Figure 7.

2.4. Summary

In the first part of this chapter an introduction to plate heat exchanger was discussed and some of earlier work on plate heat exchanger and also multiple plate heat exchanger designs and their performance was reviewed. The summary of the literature survey can be found in Table 1.

In the second part of this chapter an introduction to microchannel-manifold heat exchanger was given and several of earlier works on microchannel and manifold-microchannel heat exchangers were presented. As noted, most of the simulation works on manifold-microchannel designs were for cases where the flow was entering the manifold from the top and the effect of the flow maldistribution in the manifold was not a significant issue. Also some limited previous works were conducted for the cases where the flow was entering the manifold from the side, but those works were only for those designs with limited number of microchannels. A summary of the literature survey on manifold-microchannel heat exchangers can be found in Table 2.

The last part of this chapter discussed an introduction to heat exchanger optimization. As pointed out, in the past multiple works have been done on heat exchanger optimization considering either single or multiple objectives. Some of the works utilized metamodel combined with multi-objective optimization to reduce the computational time. A summary of the literature survey on this subject can be found in Table 3.

Table 1: Summary of plate heat exchanger literature survey

Authors	Year	Type of Plate Heat Exchanger	Major findings
Tauscher and Mayinger [9]	1997	Plate heat exchanger with rib roughened surface	Nu up to 50 and pressure drop less than 80Pa were possible
Muley and Manglik [11]	1998	Chevron plate heat exchanger	In the case of chevron plate heat exchanger increase in chevron angle can increase Nu up to a factor of 3 with a price of increasing f up to a factor of 9
Ayub [17]	2003	Various	Summary of existing correlation to calculate f and Nu for plate heat exchanger
Luan et al. [15]	2008	Corrugated plate heat exchanger	Up to 50% reduction on flow resistance is possible with price of 25% reduction in heat transfer coefficient compared to chevron heat exchanger
Durmuş et al. [16]	2009	Flat, asterisks, and corrugated plate heat exchanger	Corrugated plate heat exchanger yield the best performance with respect to heat transfer coefficient while flat heat exchanger has the lowest pressure drop.
Khan et al. [14]	2010	Corrugated plate heat exchanger	Nu range between 20 and 160 for Re between 400 and 2,500 were reported
Gherasim et al. [12, 13]	2011	Chevron plate heat exchanger	Nu between 30 and 50 and f between 3 and 10 were possible
Abu-Khader [10]	2012	Various	Summary of the recent advances of plate heat exchanger

Table 2: Summary of Manifold-microchannel literature survey

Authors	Year	Numerical or Experimental Work	Fin Base Material (FBM) and Working Fluid (WF)	Flow inlet direction in manifold	Microchannel treatment for simulation	Major Finding
Harpole, G. M., and Eninger, J. E [22]	1991	Analytical and numerical work of a single microchannel section	FBM: Silicon WF: 80% water/20% methanol	Top	Single microchannel	Heat transfer coefficient in the order of 100W/cm^{2}K and pumping power of 1 or 2 bar is possible
Copeland et al. [23]	1997	3-D CFD simulation of a single microchannel section	FBM: Silicon WF: Water	Top	Single microchannel	Pressure drop between 47 - 12,260Pa and thermal resistance of 0.25 - 1.85^{o}C/W are observed
Kim et al. [27]	1998	Experimental work of full manifold-microchannel model	FBM: Copper WF: Air	Top	-	35% reduction on thermal resistance compared to microchannel heat sink is possible
Ng & Poh [24, 25]	1999	3-D CFD simulation of a single microchannel section	FBM: Silicon WF: Water	Top	Single microchannel	Pressure drop between 45 - 10,209Pa and thermal resistance of 0.53 - 6.66^{o}C/W are observed
Ryu et al. [26]	2003	3-D CFD optimization of single microchannel and including inlet & outlet manifold region	FBM: Silicon WF: Water	Top	Single microchannel	Thermal resistance of 0.0196, 0.0232, and 0.031^{o}C/W are possible for pumping power of 2.56W
Wang, Y., & Ding, G. F. [28]	2008	3-D CFD simulation of a single manifold and microchannels section	FBM: Copper WF: Water	Side	30 microchannels	Better temperature distribution with 75% increase in heat transfer compared to microchannel heat sink

Kermani et al. [29]	2009	Experimental work of full manifold-microchannel model	FBM: Silicon WF: Water	Side	-	Heat transfer coefficient of 65.5kW/m^{2}K can be achieved for flow rate of 1.1g/s and heat flux of 75W/cm^2
Cetegen [4]	2010	3-D CFD simulation of a single microchannel section	FBM: Copper WF: Water	Top	Single microchannel	Manifold-microchannel heat sink can have 72% higher heat transfer coefficient than traditional microchannel heat sink or 306% higher than jet impingement heat sink for the same pumping power
Escher et al. [30]	2010	Full model experimental work & 3-D CFD simulation of a single manifold and microchannels section	FBM: Silicon WF: Water	Side	Substitute microchannel with porous media for simplification	Thermal Resistance of 0.09cm^{2}K/W with corresponding pressure drop of 0.22bar is possible for a system on a 2 x 2 cm^2
Boteler et al. [31]	2012	3-D CFD simulation of a single manifold and microchannels section	FBM: Silicon WF: Water	Side	2-20 microchannels	More uniform temperature distribution and 97% reduction of system pressure drop was detected compared to microchannel heat sink

Table 3: Summary of the heat exchanger optimization literature survey

Authors	Year	Multi/single objective	Optimization Variables	Optimization objective	Metamodel based?	Method
Ryu et al. [32]	2002	Single	Channel width, fin width, channel height, and pressure drop	Minimize thermal resistance	no	Random search technique
Gopinath et al. [33]	2005	Multi	Displacement of chips on the heat sink	Minimum junction temperature and length	no	Genetic algorithm
Amanifard et al. [36]	2008	Multi	2 geometrical aspect ratio & Re	Maximize (Nu) and minimize pressure drop	Yes (Neural network)	Genetic algorithm
Husain and Kim [37]	2008	Multi	The ratio between channel width and channel height & ratio between fin width and channel height	Minimize thermal resistance and pumping power	Yes (Response surface approximation base method)	Evolutionary algorithm
Husain and Kim [38]	2010	Multi	3 geometrical aspect ratio	Minimize thermal resistance and pumping power	Yes (Kriging, neural network, and response surface approximation)	Evolutionary algorithm
Saleh et al. [39]	2010	Multi	Flow velocity, 3 geometrical variables, and 3 thermal variables	Minimize maximum channel temperature and maximizing heat density	Yes (Kriging)	Genetic algorithm
Cetegen [4]	2010	Multi	Flow velocity and 4 geometrical variables	Minimize pumping power and maximize heat transfer coefficient	Yes (Kriging)	Genetic algorithm
Sharma et al. [34]	2011	Multi	Inlet flow velocity and temperature	Minimize failure rate and exergy destruction	no	Exergy based optimization
Türkakar and Okutucu-Özyurt [35]	2012	Single	Pumping power, channel width, and fin width	Minimize thermal resistance	no	Analytical optimization models

Chapter 3: Numerical Method

3.1. Introduction

In Section 1.2 the background and concept of manifold-microchannel plate heat exchanger was described. As explained in Section 1.3, the performance of a heat exchanger can be characterized by its pumping power density (P/V) and heat transfer density ($Q/(V\Delta T)$). In order to analyze the performance and identify optimum designs, both of these parameters need to be calculated. This chapter describes the numerical methodology used to calculate these parameters for manifold-microchannel plate heat exchangers.

3.2. Model Description

A multi pass manifold-microchannel plate heat exchanger consists of numerous flow paths and it is far too complex to be entirely modeled. Therefore, in order to simplify the model, only a portion of a heat exchanger consisting of a single pass and a single manifold (SPSM) will be modeled. The computational domain is shown in Figure 8.

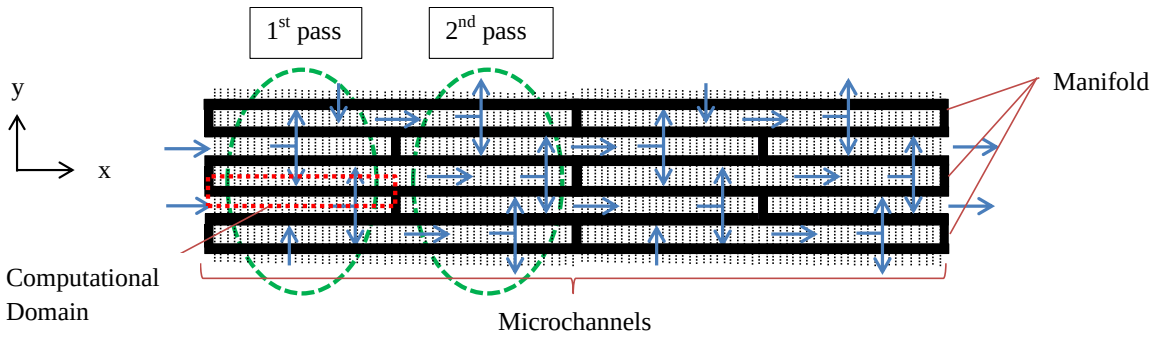

Figure 8: Computational Domain for SPSM

A SPSM model simulation's results can be expanded into whole plate surface by considering the total number of passes (Nx) and manifold channels (Ny). It also can be further expanded into multiple stacks problem by considering total number of stacks (Nz). To achieve this, three simplifying assumptions are considered:

1. Mass flow rate in all manifold channels and stacks (i.e. in y and z directions) is uniform.
2. $\Delta T = \left(T_{surf} - T_{in}\right) = LMTD/2$ remains constant over all passes. This assumption is a fair approximation for counter flow heat exchangers.
3. Geometry and volume remain unchanged from one pass into another.

Based on the above assumptions, pumping power density (P/V) and heat transfer density ($Q/(V\Delta T)$) for a SPSM model are equivalent to their corresponding values for the entire system. Therefore, the total pumping power (P_{tot}), heat transfer rate (Q_{tot}), and volume (V_{tot}) of the whole heat exchanger, can be calculated as a function of SPSM model's pumping power (P_{spsm}), heat transfer rate (Q_{spsm}), and volume (V_{spsm}) as:

$$P_{tot} = P_{spsm} N_x N_y N_z \quad (1)$$

$$Q_{tot} = Q_{spsm} N_x N_y N_z \quad (2)$$

$$V_{tot} = V_{spsm} N_x N_y N_z \quad (3)$$

P_{spsm} and Q_{spsm} can be calculated as::

$$P_{spsm} = P/V * V_{spsm} \quad (4)$$

$$Q_{spsm} = Q/(V\Delta T) * V_{spsm} * \Delta T \quad (5)$$

where $P/V = (P/V)_{spsm}$ is pumping power density and $(Q/V\Delta T) = (Q/V\Delta T)_{spsm}$ is heat transfer density which are calculated from SPSM model. The next section will explain how P/V and $Q/V\Delta T$ are calculated.

3.3. Heat Transfer Density Calculation

The heat transfer density can be calculated by performing CFD simulation on a SPSM model like the one shown in Figure 9(a). However, a model with a high number of microchannels is difficult to construct and will require a tremendous amount of computational time to simulate the heat transfer, flow field, and perform the optimization. The model can be simplified by modeling a single manifold-microchannel like shown in Figure 9(b). The additional manifold segments in this model of size $(L_{mnd}/2)$ are added in order to include the entrance and exit effects.

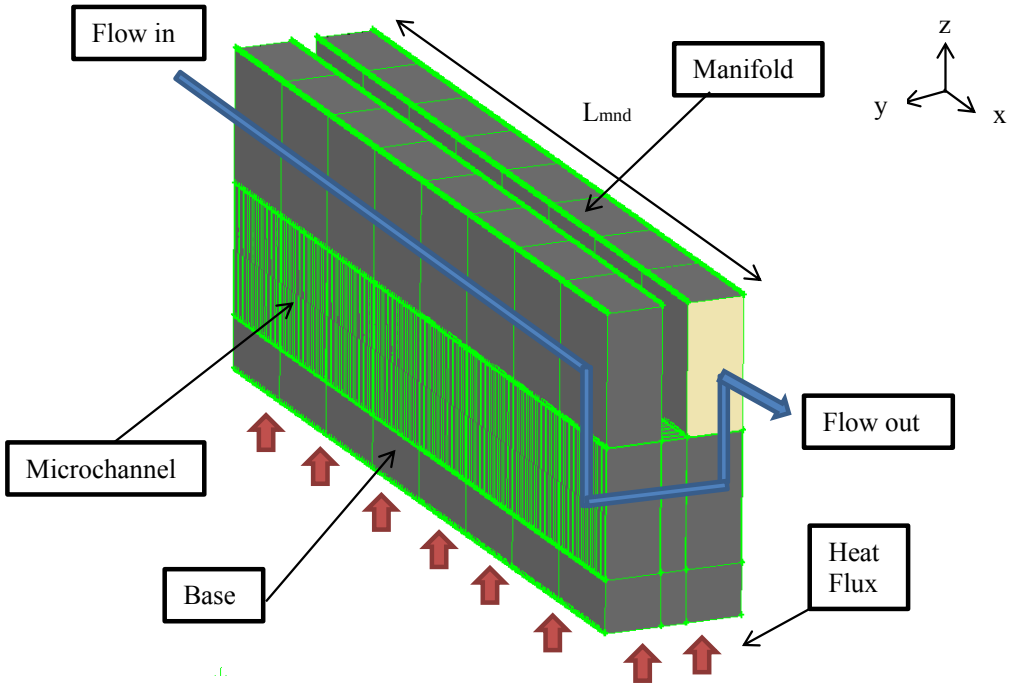

(a)

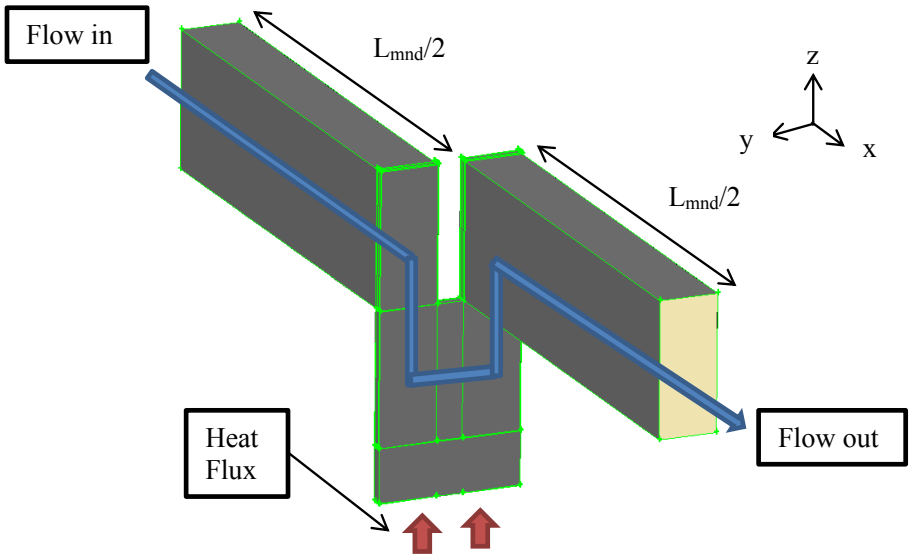

(b)

Figure 9: (a) single pass and a single manifold (SPSM) model, (b) Single manifold-microchannel model

In order to extend the heat transfer results from the single manifold-microchannel model, Figure 9(b), to the SPSM model, Figure 9(a), some simplifying assumptions are needed. First, it has been assumed that the manifold is made from non-thermally conductive material. Therefore, no heat transfer takes place from manifold walls and all the heat transfers only through microchannel base or fins. Secondly, as a first-order approximation, it has been assumed that for the u-shape flow in microchannel a linear relationship between the heat transfer density and mass flow rate, $\dot{m}$, exists. Based on these assumptions, the average heat transfer density over all microchannels in SPSM model is the same as the one for the single manifold-microchannel model as long as the mass flow rate of the single manifold-microchannel model is the same as the average mass flow rate of all microchannels in SPSM mold model. In summary:

$$\overline{Q/(V\Delta T)_{spsm}} = Q/(V\Delta T)_{sc} \text{ As long as } \quad \dot{m}_{chn} = \dot{m}_{mnd}/n \qquad (6)$$

where $\dot{m}_{chn}$ is fluid mass flow rate for the single manifold-microchannel model, $\dot{m}_{mnd}$ is total mass flow rate entering the manifold and n is the total number of microchannels in a SPSM model. In Section 3.5 it will be explained how single manifold-microchanel model is used to calculate heat transfer density term.

3.4. Pumping Power Density Calculation

In order to calculate total pumping power density, the total pressure drop in the system needs to be calculated first. Unlike heat transfer calculation, pressure drop calculation is more complex due to additional pressure drop in the manifold region which cannot be calculated using single manifold-microchannel model. Maharudrayya et al. has successfully developed analytical solutions for flow distribution and pressure drop in z-shape parallel channel configuration, like shown in Figure 10, by considering the pressure drop in both manifolds and microchannels [5]. The z-shape parallel channel is somewhat similar with SPSM model shown in Figure 9(a). However, Maharudrayya et al. solution only works for long straight channel with fully develop flow while in our case the microchannel length is very short and the flow follows a U-shape path as seen in Figure 9(b). A hybrid method based on an extension of Maharudrayya et al.'s work by considering short channel combined by a single manifold-microchannel CFD simulation is introduced to calculate the total pressure drop in manifold and microchannel.

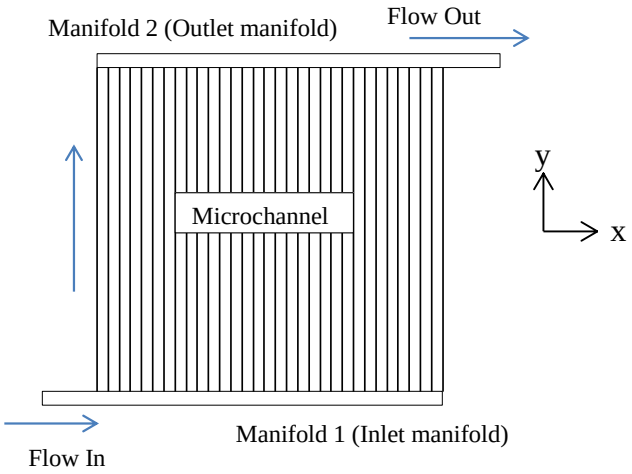

Figure 10: Z-shape parallel channel (Top view)

In order to calculate the pressure drop in manifold, first, mass balance and momentum equation are derived assuming one-dimensional flow for the control volume shown in the Figure 11(a) for the inlet manifold (manifold 1).

Mass balance equation can be written as:

$$\rho A_{mnd} v_1 = \rho A_{mnd} \left(v_1 + \frac{dv_1}{dx_1} \Delta x_1 \right) + \rho A_{chn} v_{chn} \tag{7}$$

where v_1 is flow velocity at the inlet manifold, v_{chn} is flow velocity at the microchannel, $A_{mnd}$and A_{chn} are the cross sectional areas of the manifold channel and microchannel, and Δx_1 is the length of the control volume as shown in Figure 11 which can be calculated as: $\Delta x_1 = \frac{L_{mnd}}{n}$. The mass balance can now be written as:

$$A_{mnd} \frac{dv_1}{dx_1} = -\frac{n}{L_{mnd}} A_{chn} v_{chn} \tag{8}$$

where L_{mnd} is the manifold length which is calculated as: $L_{mnd} = (t_{fin} + W_{chn})n$

The momentum equation for the control volume in Figure 11(a) can be written as:

$$p_1 A_{mnd} - \left(p_1 + \frac{dp_1}{dx_1}\Delta x_1\right) A_{mnd} - \tau_w \mathbb{P} \Delta x_1 = \rho A_{mnd} \left(v_1 + \frac{dv_1}{dx_1}\Delta x_1\right)^2 - \rho A_{mnd} v_1^2 + \rho A_{chn} v_c v_{1c} \quad (9)$$

where p_1 is pressure at the inlet manifold channel, τ_w is wall shear stress, $\mathbb{P}$ is the perimeter of the manifold channel, and v_c and v_{1c} are the velocity components at the entrance of the microchannel normal to the entrance plane and along manifold (x direction), respectively as shown in Figure 11(a). Following Maharudrayya et al.'s approach the wall shear stress can be calculated by: $\tau_w = (f_{mnd}\rho v_1^2)/2$ where f_{mnd} is manifold's friction factor. The momentum equation then can be simplified into the form of:

$$\frac{d}{dx_1}(\rho v_1 v_1) = -\frac{dp_1}{dx_1} - \frac{f_{mnd}\rho v_1^2 \mathbb{P}}{2A_{mnd}} - \frac{\rho A_c n}{A_{mnd} L_{mnd}} v_c v_{1c} \quad (10)$$

As Maharudrayya et al.'s discussed, for the case of laminar flow, the inertia term (the last term in the right) is much less than the friction term due to viscosity dominance for low Re. As a result, the inertia term can be neglected and eq. (11) can be written in the form of:

$$\frac{d}{dx_1}(\rho v_1 v_1) = -\frac{dp_1}{dx_1} - \frac{f_{mnd}\rho v_1^2 \mathbb{P}}{2A_{mnd}} \quad (11)$$

By applying the same concept the mass balance and momentum equations for outlet manifold (manifold 2), Figure 11(b), can be written in the form of:

Mass balance:
$$A_{mnd}\frac{dv_2}{dx_2} = \frac{n}{L_{mnd}} A_{chn} v_{chn} \quad (12)$$

Momentum equation:
$$\frac{d}{dx_2}(\rho v_2 v_2) = -\frac{dp_2}{dx_2} - \frac{f_{mnd}\rho v_2^2 \mathbb{P}}{2A_{mnd}} \quad (13)$$

Then the mass balance and momentum equation on inlet and outlet manifold are normalized using eq. (14) - (16) to obtain dimensionless form of mass balance and momentum equations for inlet and outlet manifolds in the form shown in eq. (17) - (20):

$$x' = \frac{x}{L_{mnd}} \tag{14}$$

$$v' = \frac{v}{v_{in}} \tag{15}$$

$$p' = \frac{p}{\rho v_{in}^2} \tag{16}$$

$$\frac{dv_1'}{dx'} = -\frac{nA_{chn}}{v_{in}A_{mnd}} v_{chn} \tag{17}$$

$$\frac{dv_2'}{dx'} = \frac{nA_{chn}}{v_{in}A_{mnd}} v_{chn} \tag{18}$$

$$2v_1' \frac{dv_1'}{dx'} + \frac{dp_1'}{dx'} + \left(\frac{\mathbb{P}(fRe)_{mnd}L_{mnd}\mu}{2A_{mnd}\rho D_{mnd}v_{in}}\right) v_1' = 0 \tag{19}$$

$$2v_2' \frac{dv_2'}{dx'} + \frac{dp_2'}{dx'} + \left(\frac{\mathbb{P}(fRe)_{mnd}L_{mnd}\mu}{2A_{mnd}\rho D_{mnd}v_{in}}\right) v_2' = 0 \tag{20}$$

$$v_1' + v_2' = 1 \tag{21}$$

Where v_{in} is the inlet fluid velocity to the manifold. More details on derivation of the mass balance and momentum equation can be found in Maharudrayya et al [5].

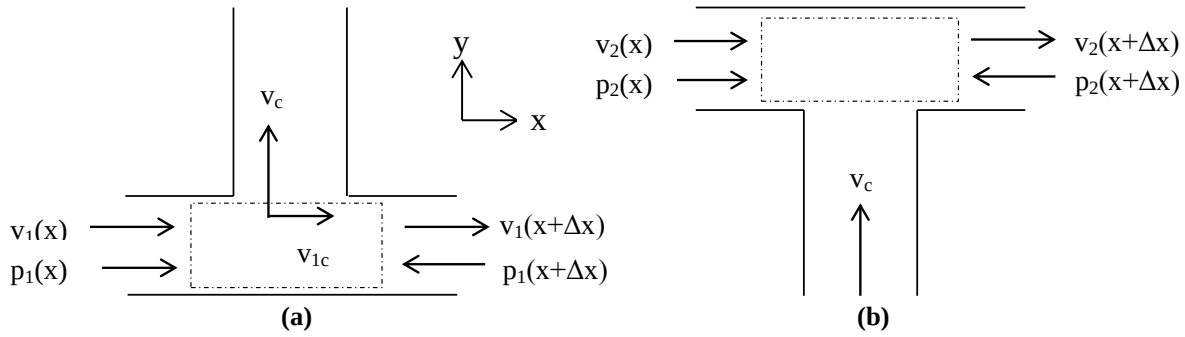

Figure 11: (a) Manifold 1 control volume (Inlet manifold), (b) Manifold 2 control volume (Outlet manifold)

In Maharudrayya et al.'s method, the pressure difference between the first and second manifold (Δp_{12}) was assumed to be equal to the pressure drop in the microchannel (Δp_{chn}) which was calculated by fully developed flow correlation. This assumption holds due to long channel assumption. For fully developed flow, friction factor times Reynolds (fRe) is known which is only a function of channel geometry and does not vary with velocity. However, for the case of short channel and with U-shape flow path like the case of manifold-microchannel plate heat exchanger, the assumption may no longer be valid.

A study was conducted to investigate if fRe remains constant for U-shape short microchanels. The result of this study is shown in Figure 12. As seen, fRe_{12} varies linearly with channel velocity (v_{chn}) indicating that fully developed flow correlation can no longer be used. Moreover, for short channel Δp_{12} is not necessary equal to Δp_{chn}. The manifold cross section area can be much larger than the microchannel like shown in Figure 13. Consequently, there will be additional pressure drop due to vertical flow in manifold which need to be taken into account.

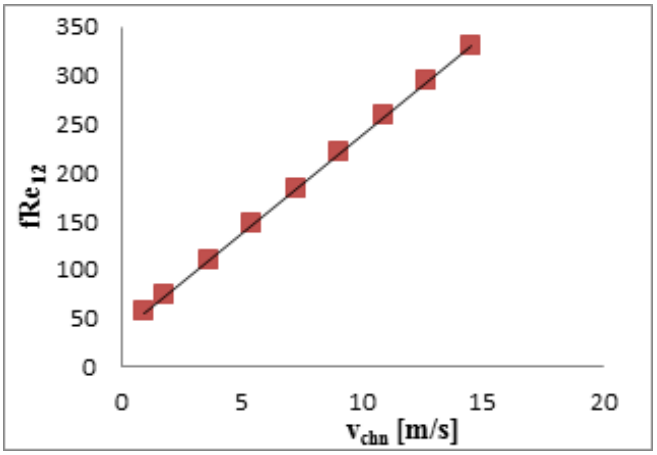

Figure 12: fRe12 v.s. vchn plot

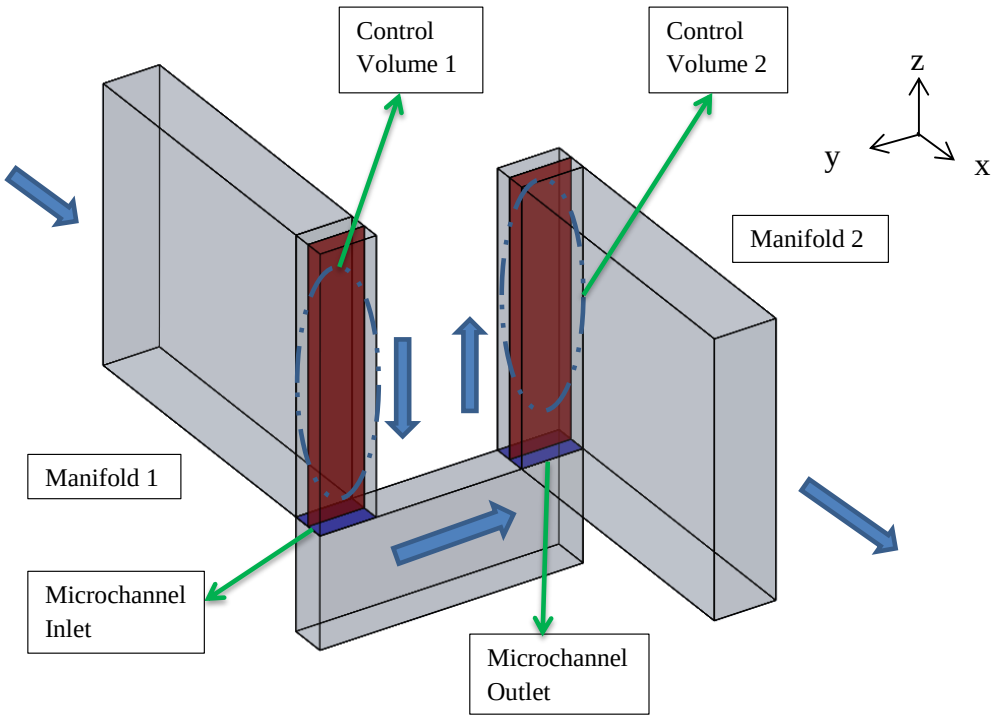

Figure 13: Single manifold-microchannel model control volume

Our survey on previous works indicated that no analytical pressure drop correlation for developing flow in a U-shape channel has been reported in the literature. However, our investigation shows that as a first order approximation for the range of parameters in our study, a linear relationship between fRe_{12} and velocity can be assumed. Figure 12 shows the CFD result from a case study where linear relationship between fRe_{12} and microchannel averaged velocity is evident. Therefore, this relationship can be shown as:

$$fRe_{12} = av_{chn} + b \tag{22}$$

where a and b are two constants which depend on geometrical parameters. For a given geometry these two constants are determined from single manifold-microchannel CFD simulation by calculation of fRe_{12} for two different v_{chn} values. The detail of this procedure is given in next section. With this assumption, Eq. (22)

can be further expanded and normalized using eqs. (14) - (16) to calculate normalized pressure drop between manifold 1 and 2 as

$$\Delta p_{12}{}' = (a v_{chn}^2 + b v_{chn}) \frac{2\mu L_{chn}}{D_{chn}^2} \frac{1}{\rho v_{in}^2} \tag{23}$$

By combining eq. (17) - (21) with eq. (23) the ordinary-differential equation that governs the normalized velocity at inlet manifold (v_1') is calculated as:

$$\frac{d^2 v_1'}{dx'^2}\left(K_3 \frac{dv_1'}{dx'} - 1\right) + 2K_1 \frac{dv_1'}{dx'} + 2K_1 K_2 v_1' - K_1 K_2 = 0 \tag{24}$$

where:

$$K_1 = \left(\frac{NA_{chn}\rho v_{in}}{A_{mnd}}\right)\left(\frac{D_{chn}^2}{2\pi L_{chn} b}\right) \qquad K_2 = \frac{\mathbb{P}(fRe)_{mnd} L_{mnd}\mu}{2A_{mnd}\rho D_{mnd} v_{in}} \qquad K_3 = \left(\frac{a}{b}\right)\left(\frac{2A_{mnd} v_{in}}{NA_{chn}}\right)$$

For K_2 calculation, $(fRe)_{mnd}$ inside the manifold can be calculated using fully developed flow correlation, eq. (25): [40]

$$(fRe)_{mnd} = 24 * (1 - 1.3553\gamma + 1.9467\gamma^2 - 1.7012\gamma^3 + 0.9564\gamma^4 - 0.2537\gamma^5) \tag{25}$$

Where γ is the aspect ratio between width and height of the manifold channel. The boundary condition in the inlet and the end of the channel for eq. (25) are determined by eq. (26) below:

$$v_1'(x' = 0) = 1 \text{ and } v_1'(x' = 1) = 0 \tag{26}$$

Note that, if fRe_{12} is independent of velocity (a=0), the ordinary differential equation in eq. (24) will become linear which was the one proposed by Maharudrayya et al. for the case of system of manifolds and long channels [5]. An analytical solution for a non-linear differential equation in the form of Eq. (24) is challenging to obtain. Therefore, the differential equation and the boundary conditions are solved

numerically using Matlab toolbox bvp4c. Despite the fact that this equation is solved numerically, the computational runtime is significantly lower than the one needed for 3-D CFD simulation of the flow in manifold.

After calculating v_1', microchannel flow velocity can be calculated by rearrange eq. (17) into the form of:

$$v_{chn} = -\frac{A_{mnd} v_{in}}{n A_{chn}} \frac{dv_1'}{dx_1'} v_{in} \tag{27}$$

Next the pressure drop between manifold 1 and 2 for any location can be calculated by inserting v_{chn} value into eq. (23).

The pressure drop along inlet manifold channel can be calculated by rearranging eq. (19) into the form of eq. (28), calculating the derivative of the normalize pressure drop $(\frac{dp_1'}{dx_1'})$, integrating it over x' and multiply the result with (ρv_{in}^2) to obtain dimensional p_1 as shown in eq. (29):

$$\frac{dp_1'}{dx_1'} = (-2v_1' \left(\frac{dv_1'}{dx_1'}\right) - k_2 v_1') \tag{28}$$

$$p_1 = \left(\int_0^{x'} \left(\frac{dp_1'}{dx_1'}\right) dx'\right) \rho v_{in}^2 \tag{29}$$

The integration of eq. (29) is carried out by assuming the pressure at the inlet $p_1'(x' = 0)$ is 0. Based on this assumption, the pressure drop along the inlet manifold (Δp_1) is equal to p_1.

The total pressure drop for a SPSM model is calculated as the sum of pressure drop at manifold 1 (calculated from eq. (29)) and the pressure drop at the last microchannel as:

$$\Delta p_{spsm} = \Delta p_1(x' = 1) + \Delta p_{12}(x' = 1) \quad (30)$$

And the total pumping power and pumping power density is calculated as:

$$P_{spsm} = \dot{m}_{mnd} * \Delta p_{spsm}/\rho \quad (31)$$

$$P/V = \frac{P_{spsm}}{V_{spsm}} \quad (32)$$

Where V_{spsm} is the volume of a SPSM model.

3.5. Single manifold-microchannel Model

For the single manifold-microchannel simulation, commercial CFD code Fluent 6.3.26 and mesh generation Gambit 2.4.6 was utilized to calculate the heat flux and pressure drop inside the microchannels by solving the continuity, momentum, and energy equations shown in Eqs. (33) - (36) [41]:

$$\nabla.(\rho\vec{v}) = 0 \quad (33)$$

$$\nabla.(\rho\vec{v}\vec{v}) = -\nabla p + \nabla.(\bar{\bar{\tau}}) \quad (34)$$

$$\nabla.\left(\vec{v}(\rho C_p T)\right) = \nabla.\left(k_{eff}\nabla T\right) \quad (35)$$

where $\bar{\bar{\tau}}$ is stress tensor which can be expressed as:

$$\bar{\bar{\tau}} = \mu\left[(\nabla\vec{v} + \nabla\vec{v}^T) - \frac{2}{3}\nabla.\vec{v}I\right] \quad (36)$$

More specifically the goal of this modeling is three things. The first is to determine the heat transfer density, $Q/(V\Delta T)_{sc}$ which is calculated by assuming the mass flow rate is uniformly distributed over all microchannels (see eq. 6). The second item is to determine coefficients *a* and *b* given in eq. (22) as $fRe_{12} = av_{chn} + b$. To do so, it is necessary that pressure drop (or fRe_{12}) is calculated for two different microchannel velocities (v_{chn}) and from there these two coefficients can be determined. The last

one is to calculate the linear equation that relates $Q/V\Delta T$ with v_{chn} to check for maldistribution which will be discussed on section 3.3.

The computational domain and boundary condition of the model is shown in Figure 14 below. The manifold channel inlet is set to mass flow rate boundary condition and constant inlet temperature (e.g. T_i =293K). The manifold channel outlet boundary condition is set to a constant pressure (e.g. $p_{out} = 0$). The boundary condition on the base is set to a uniform constant temperature (e.g. T_{base}=318K). To reduce computational domain, only half section of the manifold is modeled and symmetry boundary condition is applied.

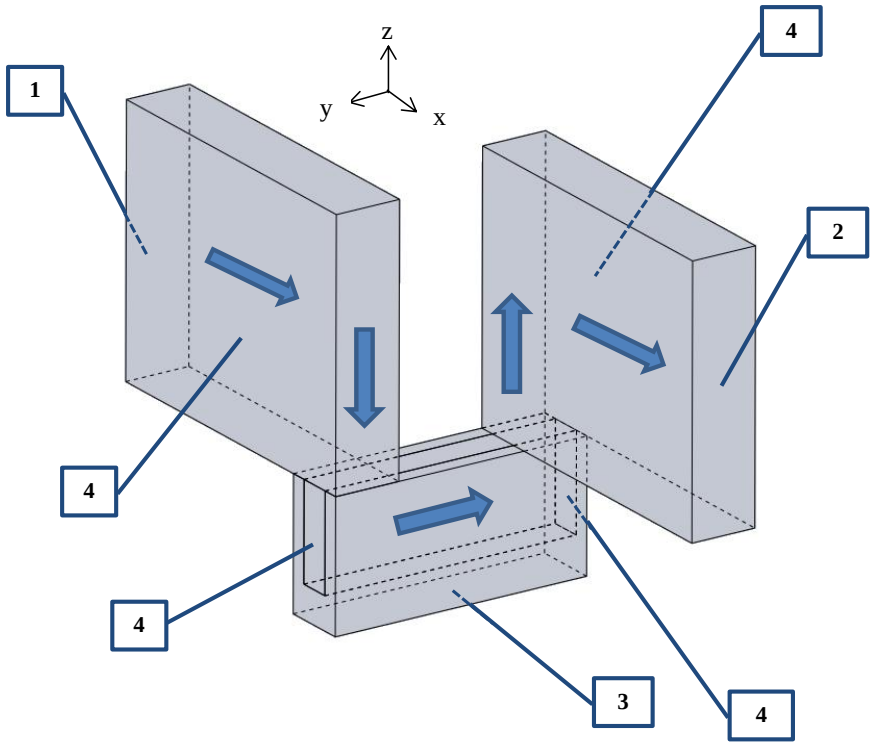

Figure 14: Computational domain and boundary conditions: mass flow inlet and constant temperature (1), constant pressure outlet (2), constant surface temperature (3), and symmetry plane (4)

3.6. Summary

In summary, the heat transfer density and pumping power density of the entire heat exchanger can be represented by their corresponding values calculated from a SPSM model. For heat transfer density calculation, the SPSM model can be further simplified into a single manifold-microchannel model as long as linear relation between heat transfer density and flow velocity is assumed. For pumping power density the calculation is more complex due to additional pressure drop in the manifold. A hybrid method was introduced to calculate the pressure drop both in microchannel and manifold.

Chapter 4: Optimization's Method, Objective, Variables, and Constrains

4.1. Introduction

In order to be able to fully utilize manifold-microchannel plate heat exchanger potentials, the optimum dimensions which yield optimum performance must be calculated. In the previous chapter, single manifold-microchannel model and hybrid methods were introduced to calculate the heat transfer density and pumping power density of the heat exchanger. The same method is applied to calculate the performance of the heat exchanger in the sampling process required for optimization. This chapter will discuss in detail the optimization method utilized as well as the optimization objectives, variables, and constrains.

4.2. Optimization Method

The optimization process can be very expensive computationally considering that it requires executing the simulation code thousands of times. Therefore, approximation assisted optimization was applied for the optimization process. This method reduces the number of CFD simulations by using a metamodel, derived from sampling results, to predict the behavior of the system. This method has been applied in the past by some other researchers as well such as Cetegen, Kim et al, Farhang-mehr et al, and Abdelaziz et al [4, 42-45]. In summary, the method consists of four main stages: Design of Experiment (DOE), metamodel creation, multi-objective optimization, and metamodel validations. The summary of the method flowchart is shown in Figure 15.

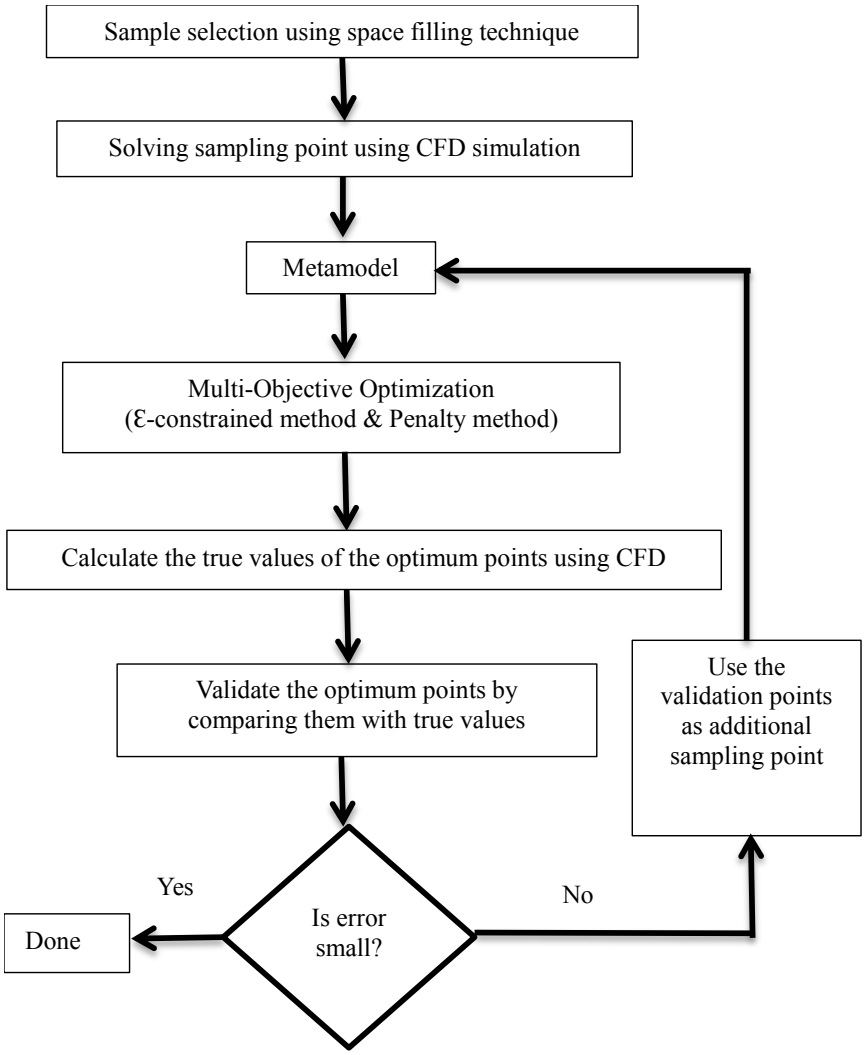

Figure 15: Approximation assisted optimization flowchart

The purpose of DOE is to determine sampling data for the metamodel. The sampling points were selected using space filling method developed by Aute *et al.* [46]. The space filling method is based on maximum entropy method which is able to obtain reasonable representation of the response space. For each of the sampling points, the objective functions were directly calculated using the hybrid method mentioned in chapter 3. The DOE is the most time consuming step of the process due to the need to simulate multiple sample points using CFD.

After DOE, the metamodel function was created based on sampling data points from DOE and then used to approximate the objective functions over a feasible domain. Kriging based metamodel was chosen because of its advantage to solve non-linear problem which depend on multiple variables. It has been widely used to approximate a system behavior [4, 39, 47-49]. Kriging metamodel is able to use known information of a system to predict the behavior of the system. This is a significant advantage especially for predicting heat exchanger performance where its performance depends on multiple variables such as, geometrical, thermal, and flow properties. Kriging metamodel works by combining regression model and random process like shown in eq. (37) below:

$$\dot{y}(\dot{x}) = \dot{F}(\dot{\beta}, \dot{x}) + \dot{z}(\dot{x}) \tag{37}$$

where $\dot{y}(\dot{x})$ is the predicted function, $\dot{x}$ is dependent variables that deduces the metamodel function, $\dot{F}$ is the regression model which depends on regression parameter $\dot{\beta}$, and $\dot{z}$ is random process which has mean zero and nonzero covariance. Dace, a Kriging base metamodel toolbox on the matlab developed by Lophaven et al. was used in this study. A more detail description about Kriging metamodel and Dace toolbox can be found in [50]. By utilizing his method, the number of required CFD simulations is reduced significantly. For example, 20000 numbers of solutions can be provided by the metamodel based on just 900 sampling points.

The metamodel function was used as an input function for the multi-objective optimization. The multi-objective optimization was performed using the Ɛ-constrained method which has been proven to be able to solve multi objective optimization problem as used by Sarker et al, Ziolkowski et al, and Takahama et al.

[51-53]. The concept of the Ɛ-constrained method is based on converting the multi-objective problem into a single-objective constrained optimization problem by setting one of the objectives as a constraint. By running the optimization multiple times and updating the constraint each iteration, the Pareto curve of the multi-objective optimization is created. The constrained single objective optimization was solved using penalty method as used by Ishizuka et al, Fletcher, Hu et al, and Lillo et al [54-57]. The concept of penalty method is on transforming the constrained problem of:

$$\text{Min } f(x) \text{ subject to } C_i(x) \leq 0 \text{ for } i=1 \text{ to } N \tag{38}$$

into a series of unconstrained problems in the form of:

$$\text{Min } \emptyset\left(x, r_p\right) = f(x) + r_p * \sum_{i=1}^{N} \min\left(0, C_i(x)\right)^2 \tag{39}$$

where r_p is the penalty coefficient and N is the number of constraints.

In order to check the accuracy of the metamodel, after performing multi-objective optimization and identifying the optimum points, the metamodel was validated by calculating the true value of the optimum points using CFD simulation and calculating their Mean Absolute Error (MAE) given as:

$$MAE = \frac{1}{N}\sum_{i=1}^{N}\left|\frac{f_{i,meta} - f_{i,cfd}}{f_{i,cfd}}\right| \tag{40}$$

where $f_{i,meta}$ is the result from the metamodel function and $f_{i,cfd}$ is its corresponding value calculated from the CFD simulation. Note that the MAE was always calculated only for the current optimum points. In case of large MAE, the metamodel was recreated by using the validation points as additional sampling points and new set of

optimum points are calculated. Since the additional sampling points are always in proximity of actual optimum points, the accuracy of metamodel increases in optimum region close to Pareto curve and the total sampling points needed are dramatically reduced. The process was repeated until a sufficiently low MAE is obtained. The target MAE for this optimization is to be less than 3%.

4.3. Optimization Objectives, Variables, and Constrains

The optimization objective is maximizing the heat transfer rate (Q) and minimizing the pumping power (P) and volume (V). The problem is simplified by reducing the three objectives into two which are: maximize heat transfer density $Q/(V\Delta T)$ and minimize pumping power density P/V which can be calculated by hybrid method explained in the chapter 3.

In total there are one flow variable, nine geometrical variables, and two material variables which can affect $P, Q,$ and V like shown in Table 4. For the material variables, only the fin-base material and working fluid need to be specified. The manifold was assumed to be made of a low thermal conductivity material so that the heat transfer from the manifold could be neglected. All of the geometrical variables are shown in Figure 16. Manifold length for a SPSM model can be expressed in terms of the number of microchannel in a SPSM model (n), fin thickness (t_{fin}) and microchannel width (W_{chn}) as:

$$L_{mnd} = n\left(t_{fin} + W_{chn}\right) \tag{41}$$

Table 4: List of variables

Flow Variable:	Inlet Reynolds number ($\boldsymbol{Re_{mnd}}$)
Geometrical Variables:	Manifold width (W_{mnd}) Manifold length (L_{mnd}) Manifold height (H_{mnd}) Microchannel width (W_{chn}) Microchannel height (H_{chn}) Microchannel inlet width (W_{in}) Microchannel exit width (W_{out}) Microchannel width to fin thickness ratio (α) Microgroove base height (H_{base})
Material Variables:	Fin & base material Working fluid

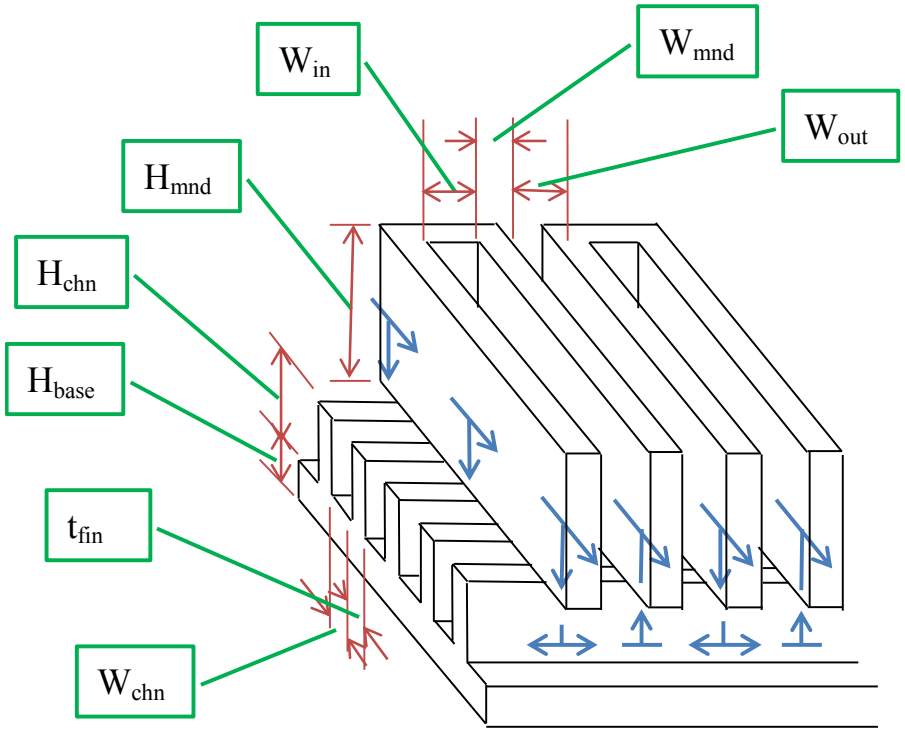

Figure 16: Depiction of geometrical variables

In the current study, microgroove base height was set as a constant at its minimum manufacturing constrained of 400μm to minimize thermal resistance on the microgroove. In addition, the microchannel inlet width was assumed to be the same as the microchannel exit width ($W_{in} = W_{out}$) for all cases because this configuration

hold the optimum performance as shown by Cetegen [4]. The range selection for the other variables will be discussed in the section 5.3. The base and fins were made of nickel or copper, while for the working fluid, water, which has the most favorable thermal properties, was chosen to calculate the highest possible performance the heat exchanger can achieve.

Maldistribution of fluid flow over microchannels can cause heat not to be transferred uniformly over entire surface of heat exchanger. A factor, F, was introduced to investigate the uniformity of the heat transfer on all of microchannels. F is defined as the ratio between the standard deviation and mean of heat transfer density of all microchannels as shown in eq. (42):

$$F = \frac{\sqrt{\frac{1}{n}\sum_{i=1}^{n}\left(\left(\frac{Q}{V\Delta T}\right)_i - \overline{\frac{Q}{V\Delta T}}\right)^2}}{\overline{\frac{Q}{V\Delta T}}} \tag{42}$$

Heat transfer density in each microchannel can be calculated based on the assumption of linear relationship with mass flow rate as explained in chapter 3.3. Based on this assumption, an equation in the form of eq. (43) can be constructed to calculate the variation of heat transfer density as a function of channel flow rate (or velocity) in each microchannel:

$$\left(\frac{Q}{V\Delta T}\right)_{chn} = cv_{chn} + d \tag{43}$$

Therefore, from the definition of F, it can be concluded that the higher its value, the larger the maldistribution. In order to minimize maldistribution, F is constrained to be less than 0.3. In addition due to manufacturing constrained, H_{chn}/W_{chn} is also constrained to be between 1 and 30.

4.4. Summary

In this chapter the optimization methodology was reviewed and the solution algorithm was introduced. In addition, the optimization objective, variables, and constrains were discussed in detail. In summary, approximation assisted optimization was utilized to determine optimum configuration of the heat exchanger. The approximation method includes Kriging based metamodel to predict the model behavior and ε-constrained and penalty method based multi-objective optimization.

Chapter 5: Results and Discussion

5.1. Introduction

In this section the optimization results based on the method described in the chapter 4 will be discussed. First, grid independency study results are discussed to obtain the reasonable grid size for CFD simulation of the single manifold-microchannel model. Then, parametric study results are discussed to determine optimization variable ranges. Next using the variable ranges selected from parametric study, the optimization is performed and the results are discussed. The optimization results then are compared with the performance of an existing plate heat exchanger, chevron plate heat exchanger, to determine how much improvement can be obtained. In addition, the characteristics of the optimize geometries are studied and discussed. Lastly, the numerical method is validated with comparison with full model CFD simulation for selected geometries and experimental results from a heat exchanger prototype.

5.2. Grid Independence Study

Grid independence analysis was performed for a selected case. The values of variables used in this case are given in Table 5. The number of computational elements was varied from 30,000 to 300,000. The percentage differences were calculated for heat transfer density and fRe_{12} for each number of elements with respect to their converged values (the one with 300,000 elements), and the results are plotted in Figure 17. As shown, heat transfer density shows lower dependency to the number of grid compared to fRe_{12}. A total of 150,000 elements, as shown in Figure 17, were chosen as the optimum element number for the rest of the study due to the

relatively low percentage difference (less than 1% difference for both cases) and acceptable convergence time. The highest number of element possible was not chosen in order to save computational time as much as possible, because for optimization the simulation needs to be repeated multiple times.

Table 5: Variables for grid independence test

Variables	Values
Re_{mnd}	500
H_{chn}	400µm
α	1
W_{chn}	40µm
W_{in}	1,200µm
H_{mnd}	1,750µm
W_{mnd}	400µm
n	150

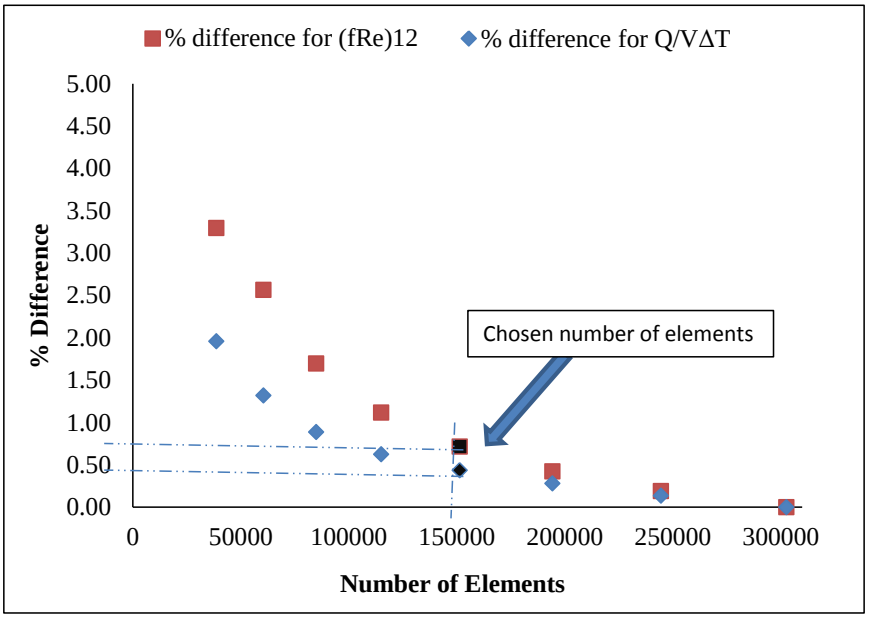

Figure 17: Grid independence study

5.3. Parametric Study

Before the optimization can be started, the ranges of the optimization variables, W_{chn}, H_{chn}, W_{in}, α, Re_{mnd}, H_{mnd}, W_{mnd}, and n, has to be defined. The lower limit of the

geometrical parameters most of the time was selected based on the typical manufacturing limitations, while for determining the upper limit a parametric study was conducted to identify the appropriate range. The idea was to set up a set of dimensions and change one parameter at a time. Each parameter was varied over a large range, and the variations of objective functions were studied. The results of the parametric study for heat transfer density and pumping power density can be seen in Figure 18.

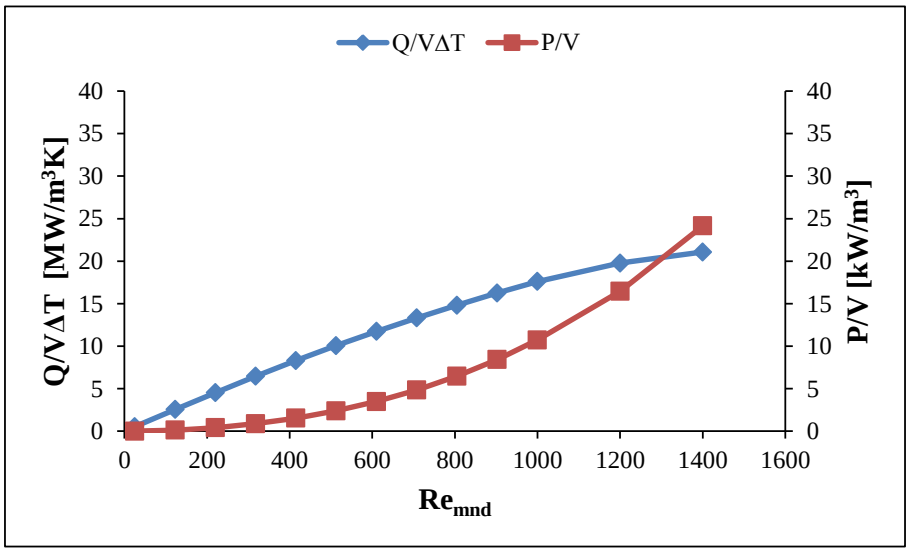

(a)

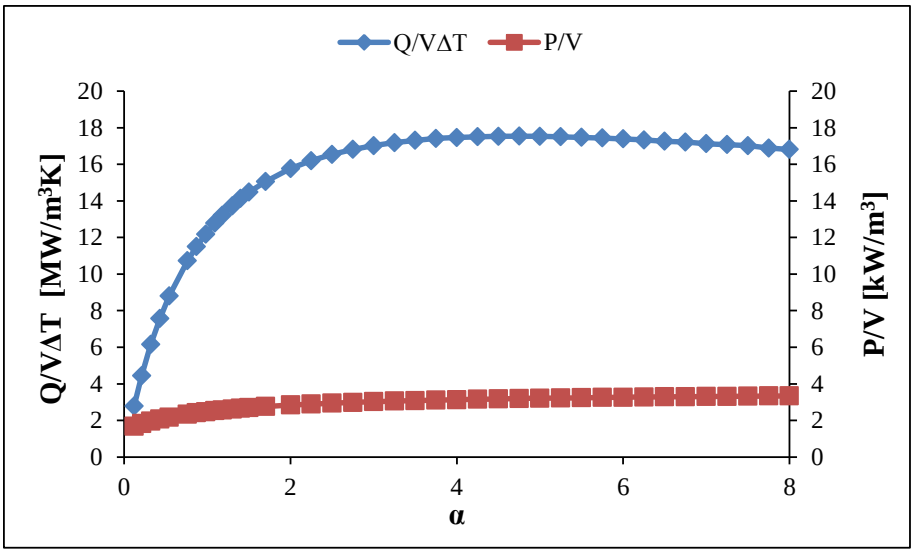

(b)

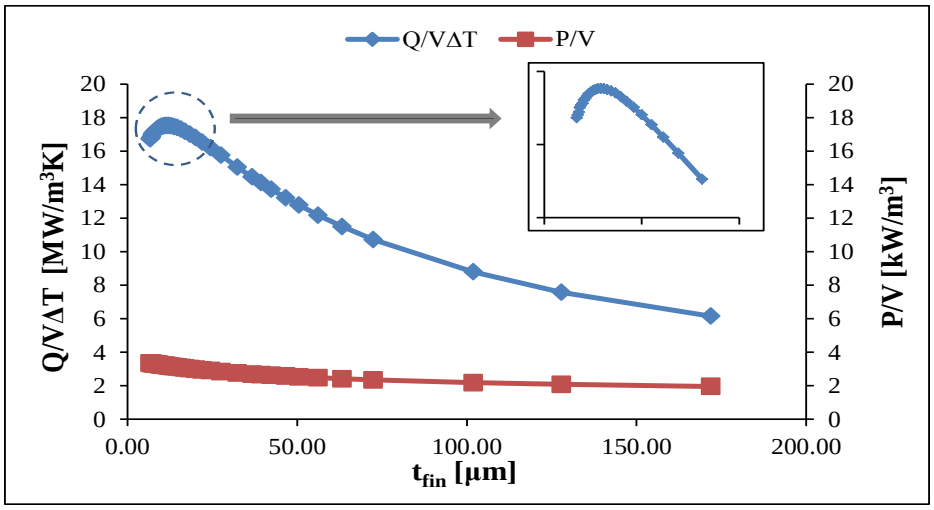
Q/VΔT
P/V
Q/VΔT [MW/m³K]
P/V [kW/m³]
t_fin [µm]
0.00
50.00
100.00
150.00
200.00

(c)

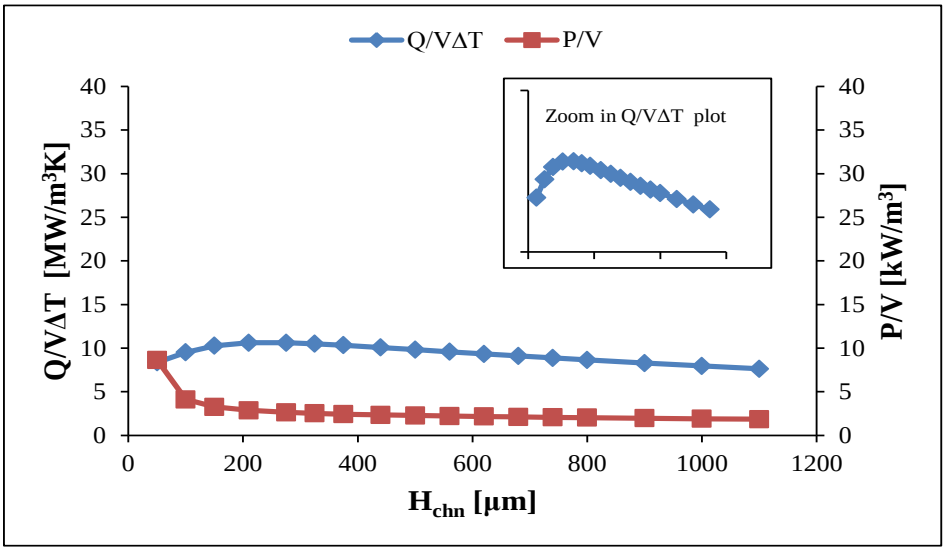
Q/VΔT
P/V
Zoom in Q/VΔT plot
Q/VΔT [MW/m³K]
P/V [kW/m³]
H_chn [µm]
0
200
400
600
800
1000
1200

(d)

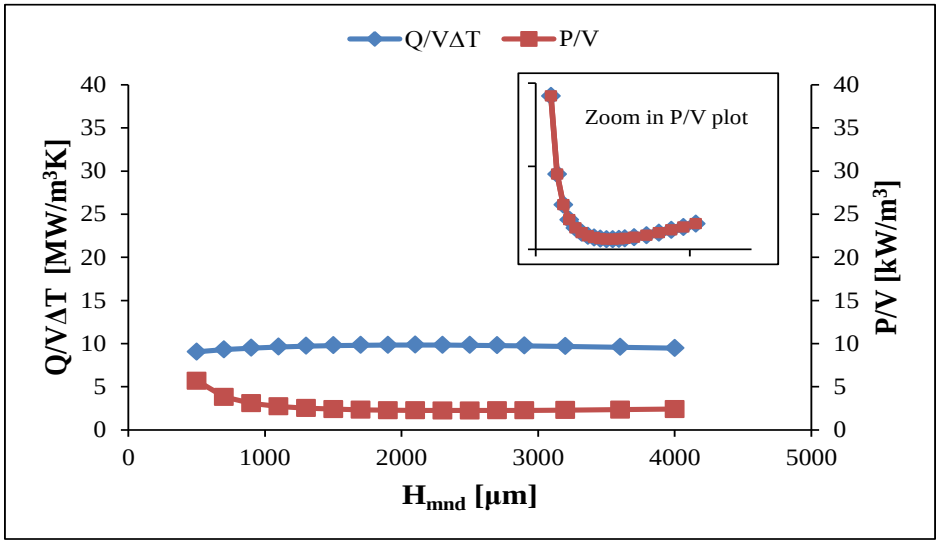
Q/VΔT
P/V
Zoom in P/V plot
Q/VΔT [MW/m³K]
P/V [kW/m³]
H_mnd [µm]
0
1000
2000
3000
4000
5000

(e)

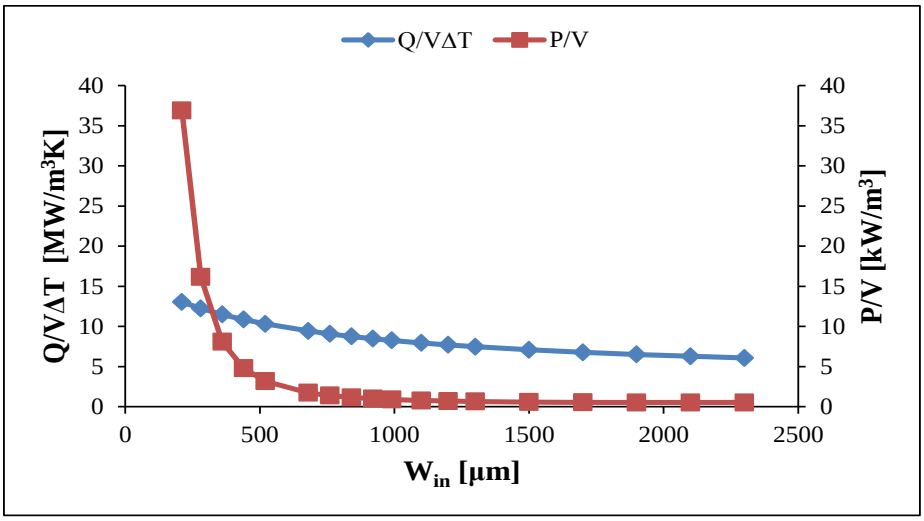
Q/VΔT
P/V
Q/VΔT [MW/m³K]
P/V [kW/m³]
W_in [µm]

(f)

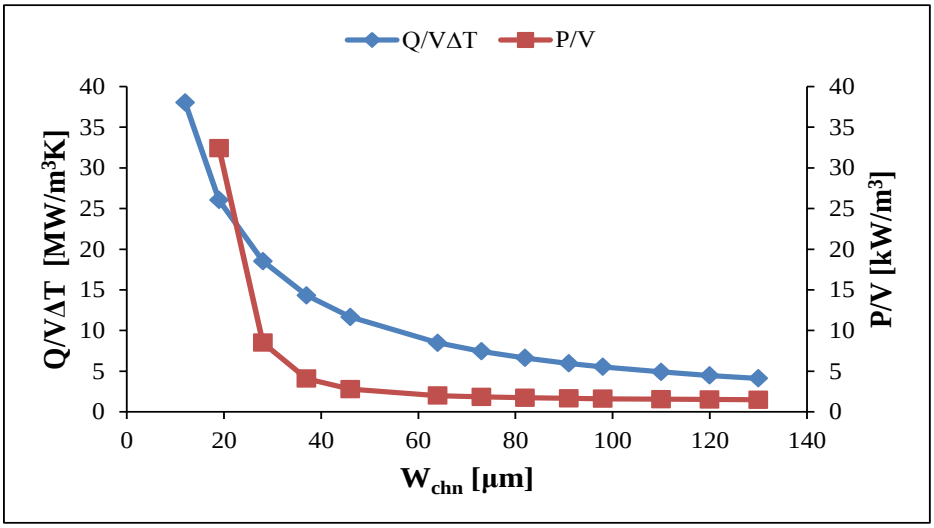
Q/VΔT
P/V
Q/VΔT [MW/m³K]
P/V [kW/m³]
W_chn [µm]

(g)

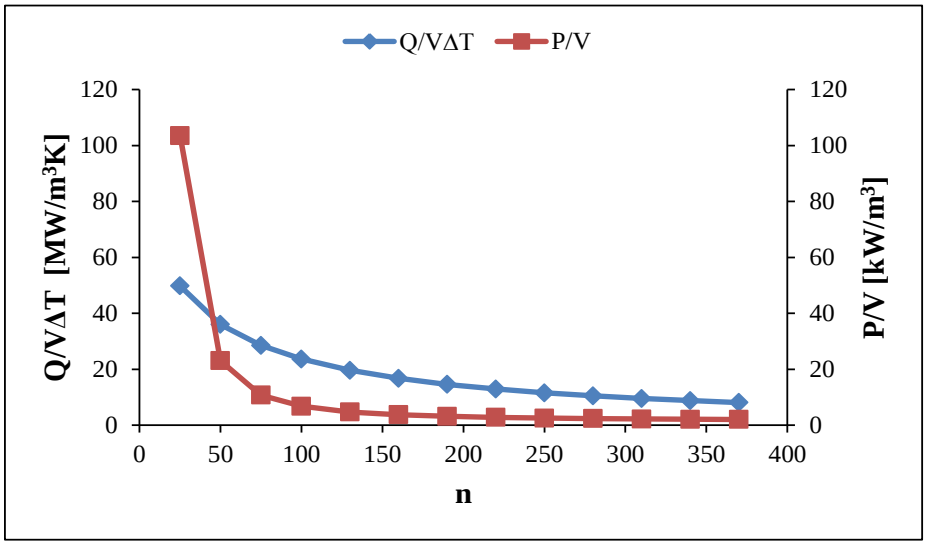
Q/VΔT
P/V
Q/VΔT [MW/m³K]
P/V [kW/m³]
n

(h)

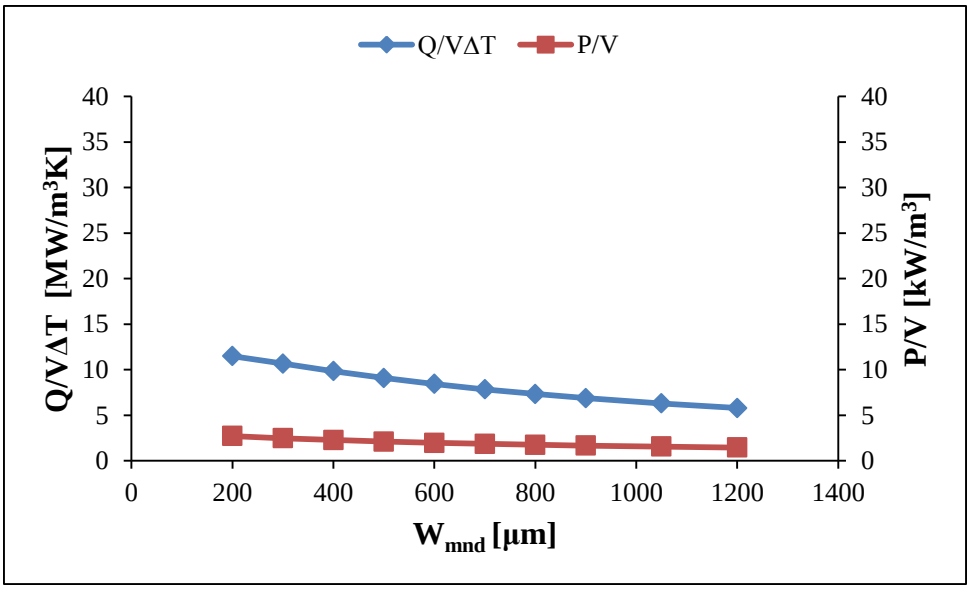

(i)

Figure 18: Parametric study results of P/V and Q/VΔT for (a) Re_{mnd}, (b) α, (c) t_{fin}, (d) H_{chn}, (e) H_{mnd}, (f) W_{in}, (g) W_{chn}, (h) n, and (i) W_{mnd}

From Figure 18(a), as Re_{mnd} increases, both pumping power and heat transfer density increase due to increase in mass flow rate. However, for high Re_{mnd}, pumping power density trend shows a steep increase, while for heat transfer density the increase remains moderate. Therefore, the upper limit of 1,000 was chosen for the Re_{mnd}. In addition, at low Re_{mnd} heat transfer density is very low so, the lower limit is set to 100.

Fin thickness (t_{fin}) is modified by changing the microchannel width to fin thickness ratio ($\alpha = W_{chn}/t_{fin}$) while setting microchannel width constant like shown in Figure 18(b)&(c). Fin thickness contribution to pumping power density is limited because the flow in microchannel is independent of fin thickness as the most of the pressure drop occurs in the microchannel. Heat transfer density increases as fin thickness increases because of the increase in fin efficiency. However, after it passes the optimum point it will start to decrease because from this point on the fin becomes too

large which increases the volume tremendously and reduces heat transfer density. In order to be able to capture the optimum fin thickness, α is varied from 0.2 to 2. The upper limit ratio of 2 is chosen because in the manufacturing point of view a large size fin is much easier to fabricate. In addition, fabrication of a thin fin is more costly and not too accurate.

The effect of microchannel height (H_{chn}) to pumping power density and heat transfer density are more difficult to predict. That is because an increase in microchannel height, for the same Re_{mnd}, will decrease the flow speed due to increase in cross section area, which in turn decreases heat transfer and pumping power. In addition, an increase in channel height also increases thermal resistance in the fin which also further reduces heat transfer. However, increase in microchannel height can also increase heat transfer due to an increase in surface contact area. The combined effect can produce a peak on heat transfer density as shown in Figure 18(d). In order to be able to capture the optimum height, microchannel height is varies from 200 to 1000μm where 200μm is the lower limit based on manufacturing limitation.

Similar trend is also observed for manifold height (H_{mnd}) as shown in Figure 18(e). The effect of manifold height on heat transfer density is limited due to the fact that most of the heat transfer is happening in the microchannel. On the other hand, manifold height contribution to pumping power density is more noticeable because, like microchannel height, an increase in manifold height, for the same Re, will decrease the flow speed which in turn decreases pumping power in manifold. However, an increase in manifold height will increase the vertical flow from the

manifold to microchannel as shown in Figure 13 before which in turn increase the pressure drop and pumping power. The combined effect can produce a minimum pumping power density as shown in Figure 18(e). In order to capture the optimum height, the manifold height is varied from 1,000 to 2,500μm.

Increase in microchannel width (W_{chn}) and inlet width (W_{in}) will decrease pumping power and heat transfer density as shown in Figure 18(f)&(g). This is because, for the same Re_{mnd}, increase in microchannel width and inlet width decrease the flow speed which in turn decrease pumping power and heat transfer density. For large microchannel width and inlet width, pumping power density relatively stays constant while heat transfer density keeps decreasing. As a result, the upper limit for microchannel width and inlet width are set to be 60μm and 2,000μm respectively while the lower limit is selected from manufacturing limitation as 20μm and 300μm respectively.

Similarly, as shown in Figure 18(h), with an increase in number of microchannel (n), pumping power and heat transfer density both decrease. For n > 300 pumping power decrease becomes insignificant while heat transfer density keeps on decreasing. This is because as the number of microchannel increases, the flow needs to be distributed into more microchannels which reduces mass flow rate delivered to each microchannel. For low number of microchannels around n = 80 , the rate of change of pumping power density will exceed that of heat transfer density at, so the number of microchannel is set to be between 80 and 300.

As manifold width (W_{mnd}) increases, pumping power relatively constant while heat transfer density decreases as shown in Figure 18(i). This is because an increase in manifold width increase pumping power and heat transfer by increase in flow length and heat transfer area respectively. However, volume is also increases. Both of these increases cancel out each other causing no significant change observed by increasing manifold width. As a result, manifold width is set as a constant of 400 μm for the entire optimization process based on the minimum manufacturing feasibility to obtain optimum heat transfer density. The summary of the lower and upper limit of all optimization variable are shown in Table 6 below.

Table 6: Optimization variables range

Variable	Lower limit	Upper limit
Re_{mnd}	100	1,000
H_{chn} [μm]	200	1,000
α	0.2	2
W_{chn} [μm]	20	60
W_{in} [μm]	300	2,000
H_{mnd} [μm]	1,000	2,500
n	80	300
W_{mnd} [μm]	400	400

5.4. Optimization Results

5.4.1. Manifold-microchannel Optimization Results

A manifold-microchannel plate heat exchanger design which had been fabricated and experimentally tested in our S2TS Laboratory by Andhare was used as a baseline for comparison with the optimization results [58]. The heat exchanger is developed as the

solution heat exchanger for absorption refrigeration and waste heat recovery applications. The design is based on ammonia hydroxide solution in both hot and cold sides as the working fluid. However, due to safety consideration, at this stage only water has been used for characterization purposes. The summary of the current design specifications is shown in Table 7.

Table 7: Summary of the specifications for the baseline design

Variable	Dimension
Re_{mnd}	1,160
H_{chn} [μm]	370
t_{fin} [μm]	40
W_{chn} [μm]	90
W_{in} [μm]	1,000
W_{mnd} [μm]	1,000
H_{mnd} [μm]	1,250
H_{base} [μm]	880
n	100
Nx	20
Ny	28
ΔT [K]	1.7
$Q/V\Delta T$ [MW/m^{3}K]	17.52
P/V [kW/m^3]	59.27
Δp [kPa]	116.9
Volume for a single stack (V) [cm^3]	39.58
Working fluid	Water
Base & fin material	Nickel

The optimization process was divided into two cases. For the first case, only the manifold section was optimized while the microchannel specifications were kept unchanged from corresponding values in baseline design as listed in Table 7. For the

second case, both the manifold and microchannel were optimized and all optimize variables were allowed to vary. In addition, in order to obtain maximum heat transfer, the fin and base material was replaced from nickel with copper which has higher heat transfer conductivity. The summary of these two optimization cases and optimization variables are shown in Table 8. The optimize results for both cases are compared with the baseline model to analyze and compare the improvement that can be obtained for optimize the manifold or optimize both manifold and microchannel.

Table 8: Optimization summary

	Case 1: Manifold optimization	**Case 2: Manifold-microchannel optimization**
Objective:	Max $Q/(V\Delta T)$ Min P/V	Max $Q/(V\Delta T)$ Min P/V
Optimization variable:	Re_{mnd} W_{in} H_{mnd} n	Re_{mnd} H_{chn} α W_{chn} W_{in} n H_{mnd}
Constrain:	$F < 0.3$ $1 < H_{chn}/W_{chn} < 30$	$F < 0.3$ $1 < H_{chn}/W_{chn} < 30$
Fin and base material:	Nickel	Copper
Working Fluid:	Water	Water

A total of 250 sampling points were selected initially using the space filling method. The sampling points were solved using CFD code on a Quad-core Intel Xenon CPU with memory of 6 GB. Four simulations were simultaneously conducted in parallel and the running time was around 45 minutes for every sampling point (Every sampling points need to be run twice for 2 difference channel velocity to calculate the

linear relation in eq. (22) and (43)). The multi-objective optimization produced 100-125 optimum points. The metamodel is recreated with additional sampling points until sufficiently low MAE was observed.

For manifold optimization, the metamodel need to be recreated twice before $MAEs$ for both pumping power density and heat transfer density were sufficiently reduced. The MAE and maximum error for the last iteration were calculated as 0.78% and 7.78% for pumping power density and 0.48% and 3.79% for heat transfer density respectfully. In total, 360 sampling points were required to reach the MAE target. At this stage the feasibility domain contained about 20,000 data pints calculated from metamodel. The optimization result is shown in Figure 19(a).

For manifold-microchannel optimization, more sampling points were needed to achieve the MAE target because more variables are involved. In total, the metamodel need to be recreated five times with 900 points solved. The MAE and maximum error for the last iteration were calculated as 2.65% and 12.2% for pumping power density and 0.65% and 2.23% for heat transfer density respectfully. At this stage the feasibility domain contained about 20,000 data pints calculated from metamodel. The optimization result is shown in Figure 19(b).

The MAE in pumping power density calculation is higher than that of heat transfer density. This is mainly because pumping power density is more strongly dependent on channel hydraulic diameter than heat transfer density. Channel hydraulic diameter depends on microchannel height (H_{chn}), microchannel width (W_{chn}), and inlet width (W_{in}). According to the parametric study results shown in Figure 18, both heat

transfer density and pumping power density varied rapidly with W_{chn}. However, heat transfer density variation is moderate with respect to H_{chn} and W_{in} while pumping power density show much more variation. These results explain why pumping power density shows a broader variation than heat transfer density. As shown in Figure 19, the range of pumping power density variation is more than twice that of heat transfer density variation. Nevertheless, in overall the MAE for both pumping power density and heat transfer density are in acceptable ranges (less than 3% for both cases), which indicates that the metamodel is sufficiently accurate.

Looking at the optimization results in Figure 19 there is no single optimum solution for the problem. This is due to the conflicting objectives of minimizing pumping power density and maximizing heat transfer density. Therefore, the solution is shown in the form of a Pareto plot. The "+" points represents the feasible domain obtained from metamodeling, while the "□ or ◊" points represent the optimum points. Both plots show that the optimum points are correctly positioned on the upper left region of the feasible domains, which agrees with the optimization objective. This shows that the optimization method can determine the optimum configurations for both cases with relatively low MAE. All of the optimum points and their corresponding geometry can be found in appendix A for case 1 and appendix B for case 2.

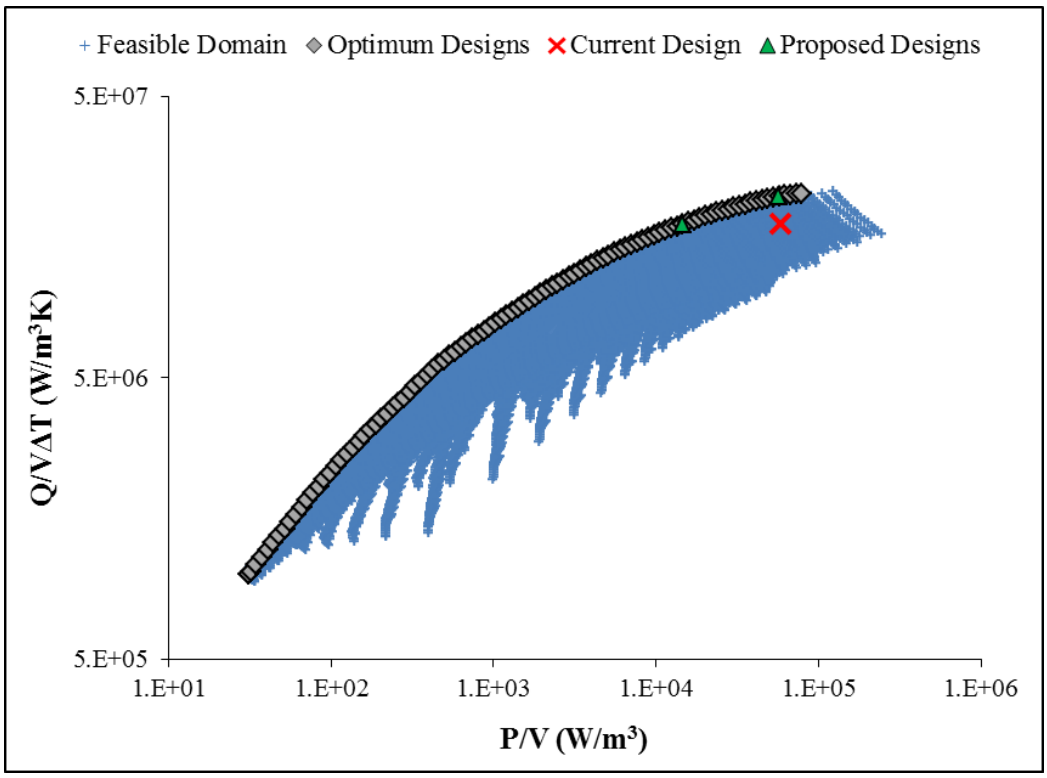
Feasible Domain
Optimum Designs
Current Design
Proposed Designs
5.E+07
5.E+06
5.E+05
Q/VΔT (W/m³K)
1.E+01
1.E+02
1.E+03
1.E+04
1.E+05
1.E+06
P/V (W/m³)

(a)

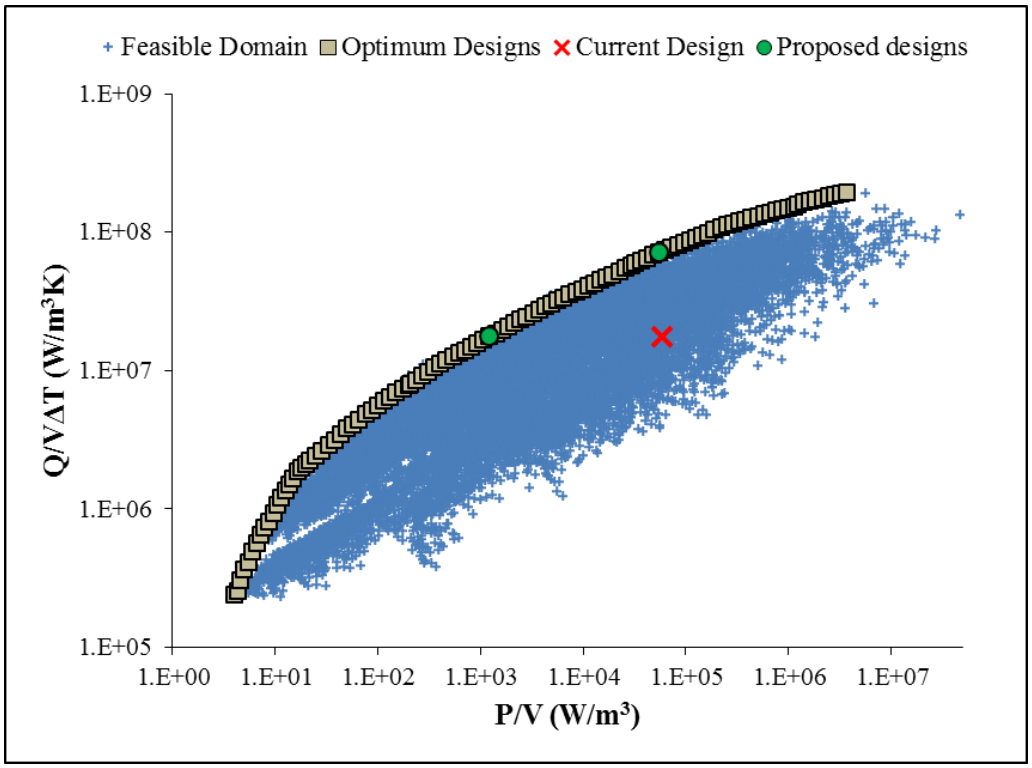
Feasible Domain
Optimum Designs
Current Design
Proposed designs
1.E+09
1.E+08
1.E+07
1.E+06
1.E+05
Q/VΔT (W/m³K)
1.E+00
1.E+01
1.E+02
1.E+03
1.E+04
1.E+05
1.E+06
1.E+07
P/V (W/m³)

(b)

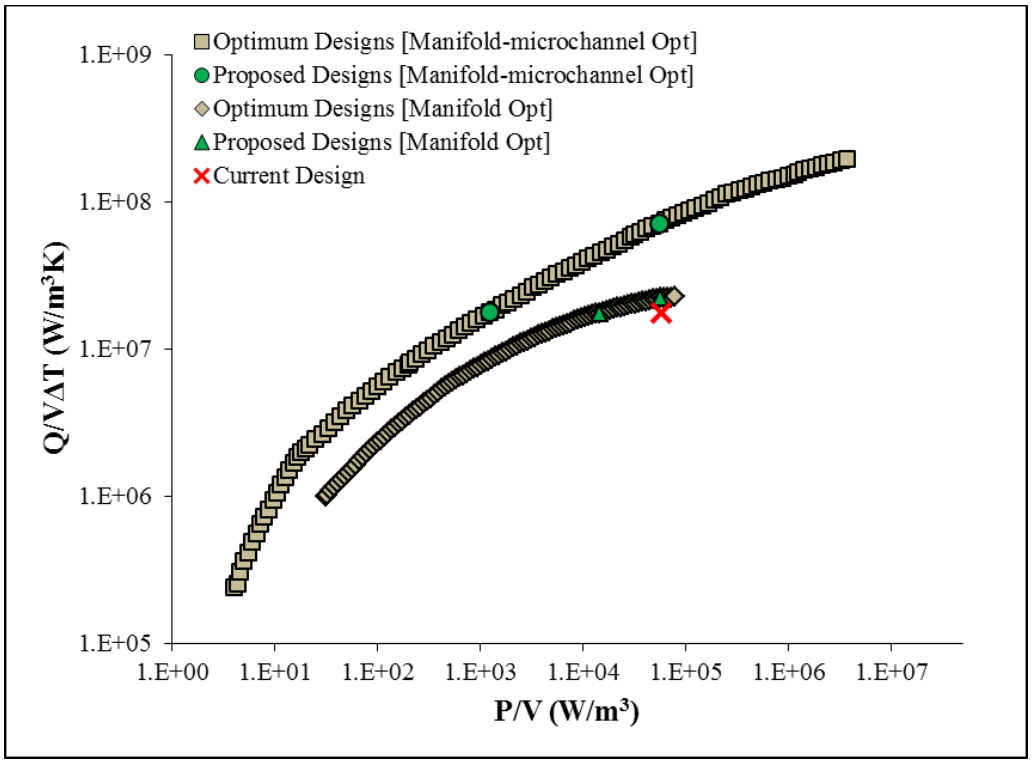

(c)

Figure 19: Optimization results: (a) Manifold optimization, (b) Manifold-microchannel optimization, and (c) Comparison between both cases

Comparing the optimization results for both cases, Figure 19(c), it is clear that optimizing both manifold and microchannel shows better results compared to the results obtained for optimizing manifold only. This seems logical because optimization of both manifold and microchannel geometries means fully utilizing the potential that the manifold- microchannel technology can offer.

The position of the current design ("x" point) with respect to the optimum points is also shown in Figure 19. To determine the improvement which can be obtained, note that two new designs are offered for each case: One which considers improvement in pumping power density while keeping heat transfer density constant and one that improves the heat transfer density while keeping pumping power density constant as

shown with in Figure 19. For manifold optimization (case 1), pumping power density can be reduced by a factor of 4 while maintaining the same heat transfer density or alternatively, heat transfer density can be increased 26% for the same pumping power density. As explained before, manifold-microchannel optimization (case 2) can achieve higher improvement compared to manifold optimization (case 1). For this case pumping power density can be reduced by a factor of 48 for the same of heat transfer density or alternatively heat transfer density can be increased 4 times for the same pumping power density. Reducing pumping power density may be more preferred than increasing heat transfer density considering that the factor of the pumping power density reduction is much higher than the factor of the increase in heat transfer density. The summary of the improvement with respect to both cases is shown in Table 9.

Table 9: Summary of improvement with respect to the current design

		$Q/V\Delta T$ [MW/m^{3}K]	P/V [kW/m^3]
Current Design		17.52	59.27
Optimize Design [Manifold Opt]	**Design 1 (Improve pumping power density) :**	17.59	14.67
	Design 2 (Improve heat transfer density) :	22.06	57.25
Optimize Design [Manifold-microchannel Opt]	**Design 1 (Improve pumping power density) :**	17.62	1.23
	Design 2 (Improve heat transfer density) :	71.33	54.99

5.4.2. Comparison with a Selected Type of Plate Heat Exchanger

In order to determine how much advantage manifold-microchannel can offer compared to other design, a comparison is made between the optimize results of the

manifold-microchannel optimization (case 2) with Chevron plate heat exchanger which is a widely used plate heat exchanger in industry. Multiple chevron plate heat exchanger correlations have been proposed in literature including correlations by Thonon [59], Kovalenko and Maslov [60], Cooper [61], Kumar [62], and Focke et al. [63]. The summary of chevron plate heat exchanger correlations can be found in Ayub [17]. Out of those correlations, the correlations by Focke et al. is one of the most widely used correlation and it yield the highest Nu compared to the others which make it the most suitable correlation for comparison. Based on the correlation the performance of Chevron plate is governed by Reynolds number (Re), Prandtl number (Pr), chevron angle (β), and constant coefficients as:

$$Nu = C_1 Re^m Pr^{0.5} \tag{44}$$

$$f = \frac{1}{4}\left(\frac{C_2}{Re^p} + C_3\right) \tag{45}$$

Where C_1, C_2, C_3, m, and p can be found in Table 10:

Table 10: List of constants for Focke et al. correlation [63]

β	Re	C_1	m	Re	C_2	p	C_3
60	120-1000	0.7	0.54	laminar	57.5	1	0.093
	1000-42000	0.44	0.64	3000-50000	0.8975	0.263	-
45	45-300	1.67	0.44	150-1800	91.75	1	0.3025
	300-2000	0.405	0.7	1800-30000	1.46	0.177	-
	2000-20000	0.84	0.6				
30	20-150	1.89	0.46	90-400	188.75	1	1.2575
	150-600	0.57	0.7	400-16000	6.7	0.209	-
	600-16000	1.112	0.6				

In order to calculate the corresponding Nusselt number (Nu) and fanning friction factor (f) for the optimization results, the hydraulic diameter of the manifold-microchannel plate heat exchanger need to be defined. The hydraulic diameter of the plat heat exchanger (D) can be calculated as:

$$D = 2H/\varphi \tag{46}$$

Where H is height of the channel and φ is enlarge factor which is the ratio between developed length and protracted length. A more detailed explanation about enlarge factor can be found in [17]. For the case of manifold-microchannel plate heat exchanger, the comparable channel high is equal to the manifold channel height (H_{mnd}) and φ is calculated as:

$$\varphi = \frac{2H_{mnd}+L_{chn}+0.5W_{in}+0.5W_{out}}{L_{chn}+0.5W_{in}+0.5W_{out}} \tag{47}$$

The corresponding (Nu) and (f) for the manifold-microchannel optimization results can then be calculated using eq. (48) & (49):

$$Nu = \frac{Dh_{base}}{k} \tag{48}$$

$$f = \frac{\Delta p_{tot} D}{L_{mnd}} \frac{1}{2\rho v_{mnd}^2} \tag{49}$$

The Nu and f calculated for SPSM model is equivalent to their corresponding values for multiple manifold and passes. This is because D remains identical in all manifold channels and passes due to the assumption of uniform manifold and microchannel geometry across the heat exchanger. In addition, base heat transfer coefficient (h_{base})

and flow velocity at manifold (v_{mnd}) are constant for the entire heat exchanger due to assumptions explained in section 3.2.

In addition, for the case of manifold-microchannel heat exchanger with multiple passes, the rate of change of total pressure drop increase due to additional passes is proportional to the increase of the manifold length (L_{mnd}). In calculation of f, both increase in turn will cancel each other, so f calculated for SPSM model is equivalent to their corresponding values for multiple passes.

The comparisons between both heat exchangers designs are shown in Figure 20(a) and (b) for Nusselt number and for friction factor, respectively. Manifold-microchannel model offer higher Nu compared to all Chevron plate designs for high Re while it yields the lower f. For low Re, Nu of manifold-microchannel model is just below the chevron plot of 30^o which is the highest out of the three angle. However, it still yields the lowest $f$among all designs. Unlike chevron heat exchangers, the optimum manifold-microchannel results depend on not only Re but also geometrical parameters, so a different Nu and f values are possible for the same Re which can explain the jump seen on the curve. In summary, this shows that optimized Manifold-microchannel design has potentially superior performance compared to Chevron plate in terms of Nu and f which are the widely used parameters to characterize plate heat exchanger.

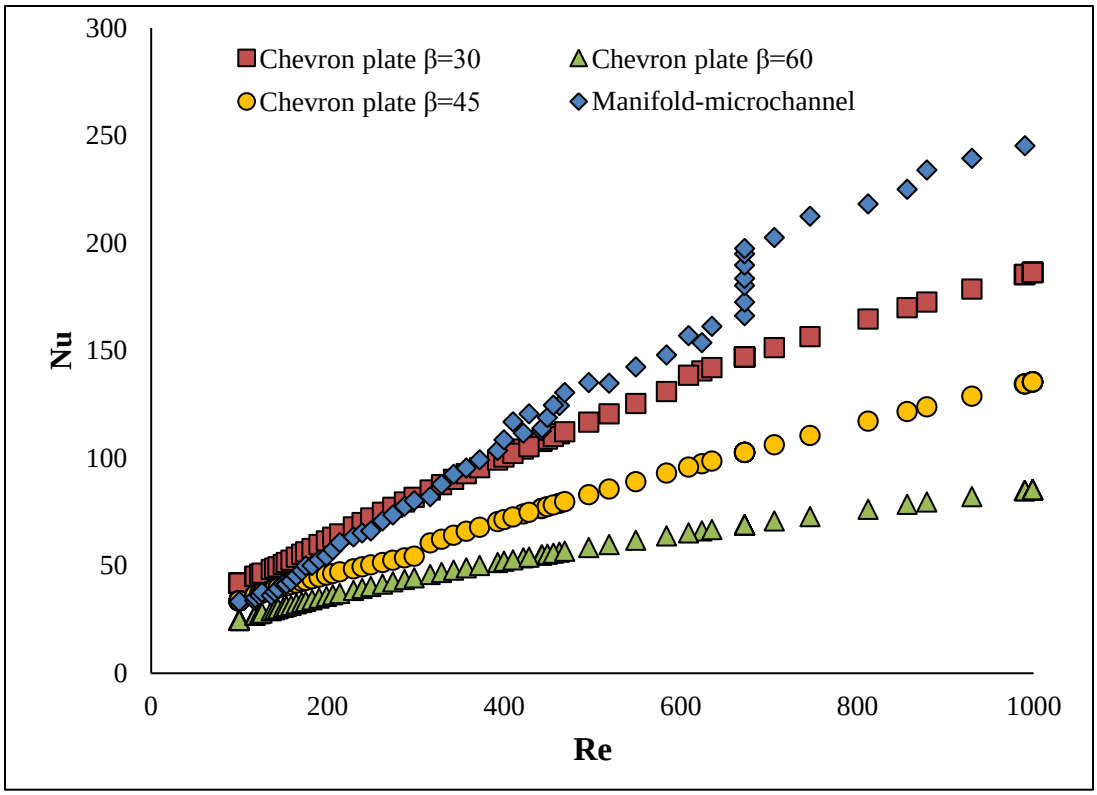

(a)

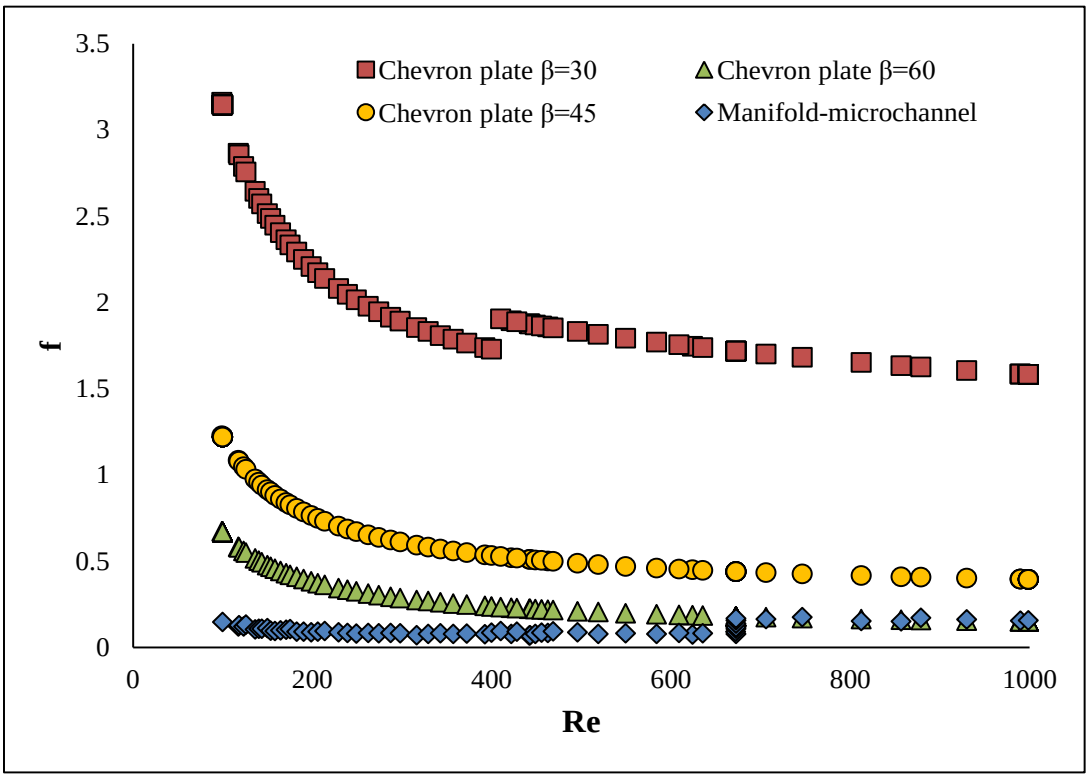

(b)

Figure 20: Optimization results comparison with Chevron plate heat exchanger: (a) Nu and (b) f

5.4.3. Specifications of optimum designs

The behavior of the optimum geometrical variables and flow parameters with respect to the optimum heat transfer density and pumping power density are presented in Figure 21. As seen, low pumping power density and heat transfer density are achieved by low (Re_{mnd}), low microchannel width to fin thickness ratio (α) which also equivalent to high fin thickness (t_{fin}), high manifold height (H_{mnd}), high microchannel height (H_{chn}), high microchannel width (W_{chn}), and high microchannel inlet width (W_{in}), and high number of microchannels (n). Overall, larger microchannel and manifold channel dimensions and smaller flow rate yield lower pumping power and heat transfer density. The other way around needs to be done to achieve high heat transfer density and high pumping power density. That is the microchannel and manifold channel need to be minimized while the flow rate needs to be maximized.

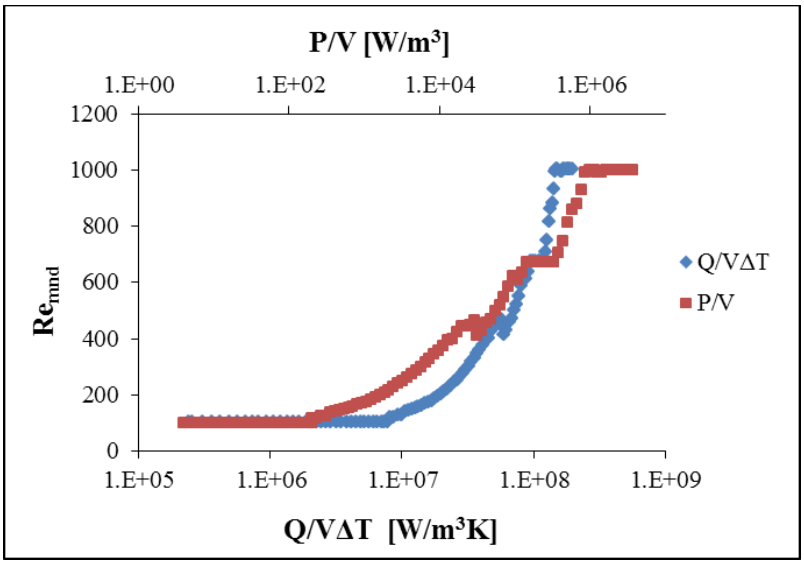

(a)

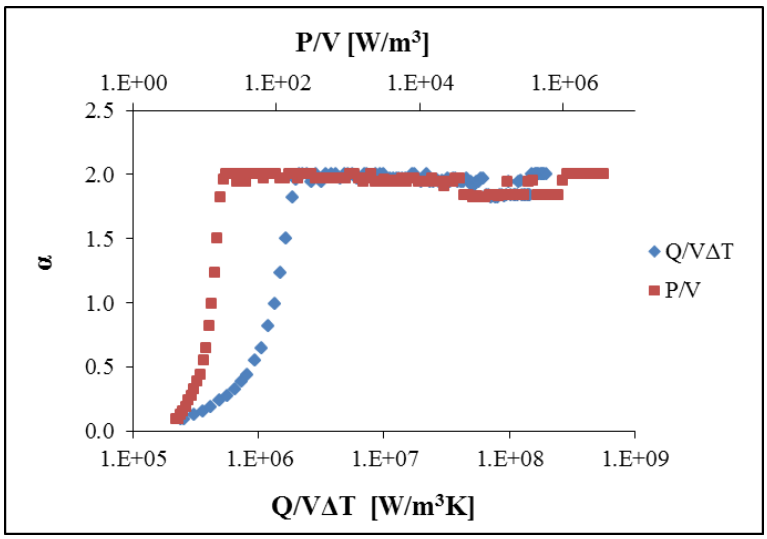
P/V [W/m³]
1.E+00
1.E+02
1.E+04
1.E+06
2.5
2.0
1.5
1.0
0.5
0.0
α
1.E+05
1.E+06
1.E+07
1.E+08
1.E+09
Q/VΔT [W/m³K]
Q/VΔT
P/V

(b)

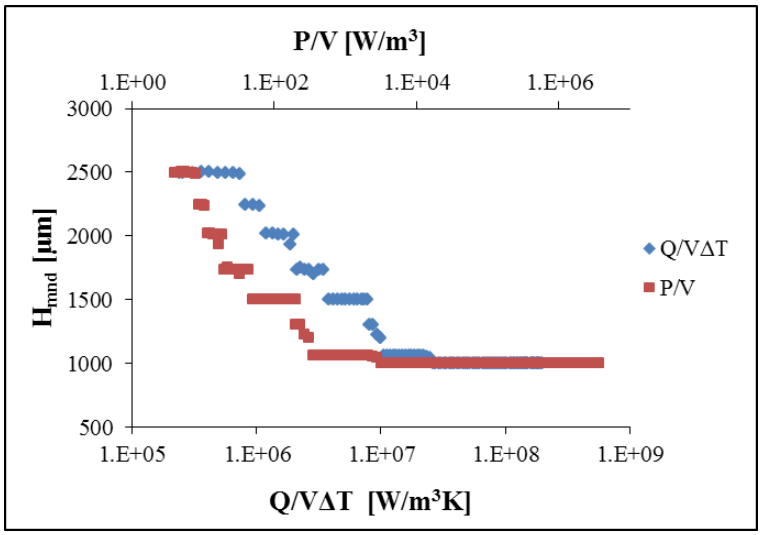
P/V [W/m³]
1.E+00
1.E+02
1.E+04
1.E+06
3000
2500
2000
1500
1000
500
H_mnd [µm]
1.E+05
1.E+06
1.E+07
1.E+08
1.E+09
Q/VΔT [W/m³K]
Q/VΔT
P/V

(c)

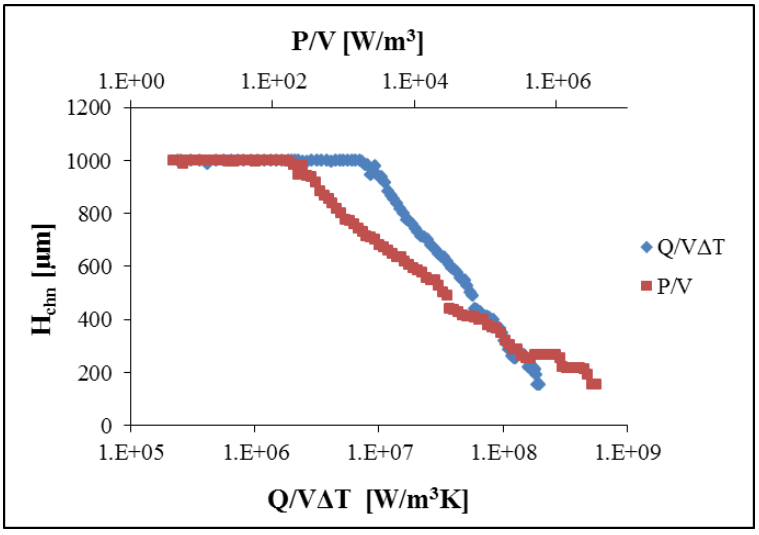
P/V [W/m³]
1.E+00
1.E+02
1.E+04
1.E+06
1200
1000
800
600
400
200
0
H_chn [µm]
1.E+05
1.E+06
1.E+07
1.E+08
1.E+09
Q/VΔT [W/m³K]
Q/VΔT
P/V

(d)

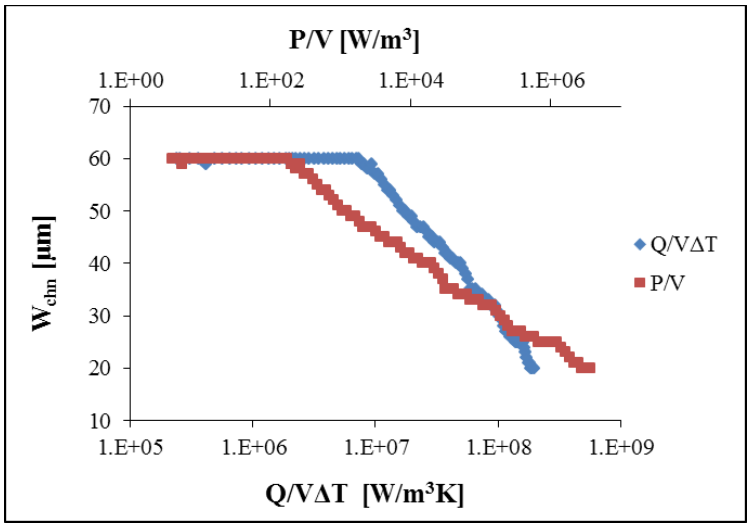

(e)

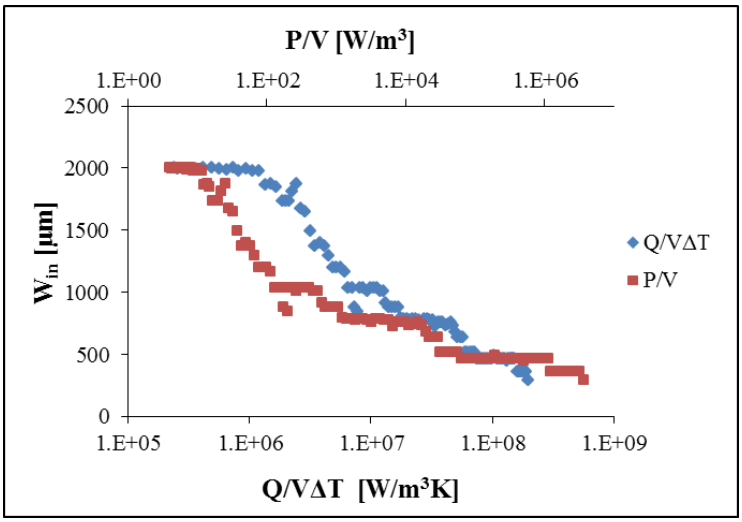

(f)

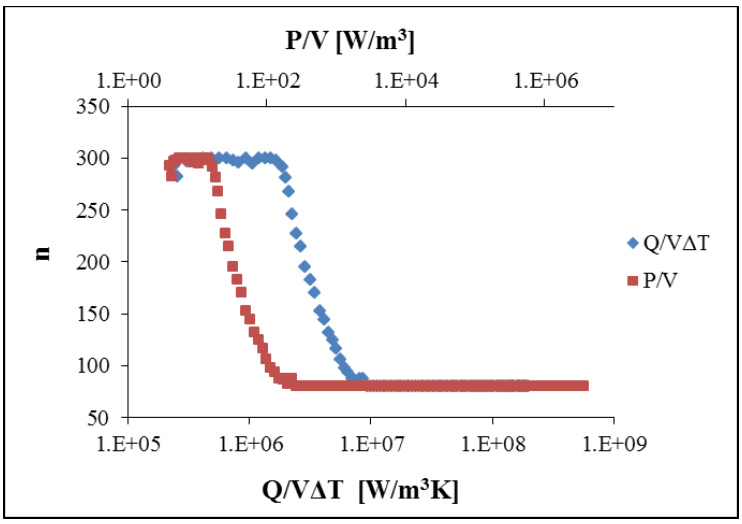

(g)

Figure 21: Variation of manifold-microchannel optimum variables with respect to Q/VΔT and P/V for: (a) Re_{mnd}, (b) α, (c) H_{mnd}, (d) H_{chn}, (e) W_{chn}, (f) W_{in}, and (g) n

Examining the optimum geometry and flow variables in Figure 21, it can be seen that all variables are varied from their lower limit to their upper limit or the other way around. When a variable hits its lower or upper limit, it will stay in the limit even as pumping power density and heat transfer density is changing. For example, for the case of Re_{mnd}, as shown in Figure 21(a), it stays at its lower limit even though pumping power density and heat transfer density are changing. Similarly for the case of H_{chn}, shown in Figure 21(d), as pumping power density and heat transfer density decrease, eventually H_{chn} reaches its upper limit and it remains at that limit. The above trends are possible because pumping power density and heat transfer density depend on all seven variables. Unlike for parametric study where only one variable changes each time, all of the optimum points shown in Figure 21 have different geometry and Re_{mnd}. So even if some of the variables remain constant, a variation in pumping power density and heat transfer density can still be observed due variation of the other variables.

As Re_{mnd} increases, optimum pumping power density and heat transfer density increases sharply as shown in Figure 21(a). This kind of behavior was expected because the increase in mass flow rate increases both pumping power density and heat transfer density.

As α increases, optimum pumping power density and heat transfer density increases as shown in Figure 21(b). Since $\alpha = \frac{W_{chn}}{t_{fin}}$, one can relate variation of α to $t_{fin}$and determine variation of heat transfer and pumping power densities with respect to t_{fin} as shown in Figure 22. Since an increase in α corresponds to a decrease in fin

thickness, minimum fin thickness is preferred for attaining high heat transfer density, The result is contradicting with the idea that increasing fin efficiency by increasing its thickness would enhance heat transfer density. That is because volume is playing a more dominant role in calculating heat transfer density. This is due to the fact that an increase in fin thickness significantly increases the total volume of the heat exchanger which in turn decreases the heat transfer density.

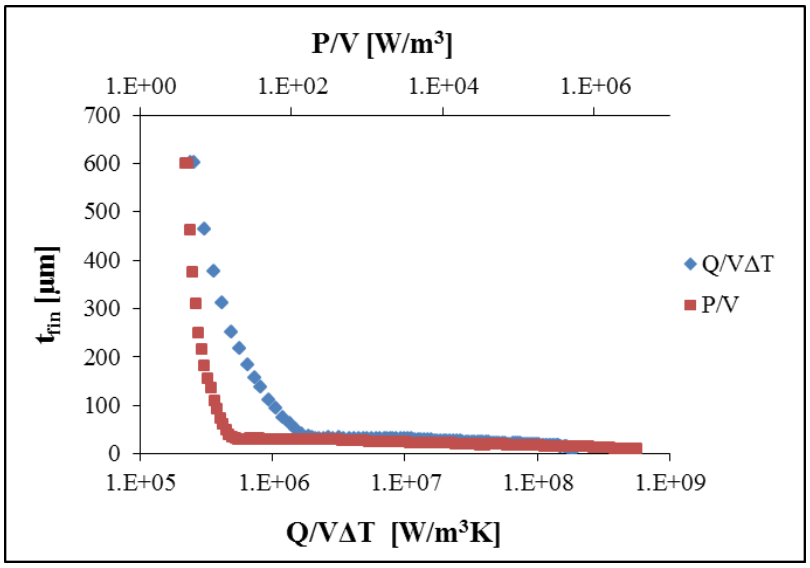

Figure 22: Variation of manifold-microchannel optimum variables with respect to Q/VΔT and P/V for t_{fin}

Unlike Re and α, as manifold height and microchannel height increase, both optimum pumping power density and heat transfer density decrease as shown in Figure 21(c) & (d). This is because increase on manifold and microchannel height increases the flow area which in turn reduce pressure drop. It is expected that an increase in manifold height will not cause significant effect on heat transfer density since the majority of heat transfer happens in the microchannels. On the other hand, an increase in microchannel height can reduce heat transfer density due to an increase in thermal

resistance on the fin. In addition, increase in volume also further reduces both pumping power density and heat transfer density.

Similarly, an increase on microchannel width and inlet width, decrease the optimum pumping power density and heat transfer density as shown in Figure 21(e) & (f). Pumping power density decreases due to an increase in flow area in microchannel. Likewise, an increase in microchannel width and inlet width can enhance heat transfer due to an increase in heat transfer area. However, an increase in size also means an increase in the total volume of the heat exchanger which in turn reduces the heat transfers density since it is a more dominant factor in this case.

An increase on number of microchannels also reduces the optimum pumping power density and heat transfer density as shown in Figure 21(g). This is because as the number of microchannels increases the flow needs to be distributed into more microchannels which reduces mass flow rate entering each microchannel.

The geometrical and flow variables of the optimum design for manifold optimization also behave similarly as shown in Figure 23. The only exception is that the optimum manifold height is always constant at its lower limit for any values of optimum pumping power density and heat transfer density as seen in Figure 23(b). As mention in parametric study, Figure 18(e), there is an optimum manifold high for each given model. Constant manifold height means that the those optimum heights always fall in lower range with respect to the lower limit that is selected for manifold height for all models.

In summary, to achieve high pumping power density and heat transfer density, Re_{mnd} needs to be maximized, Figure 23(a), manifold height needs to be minimized, Figure 23(b), microchannel inlet width needs to be minimized, Figure 23(c), and minimum number of microchannel needs to be implemented, Figure 23(d). For minimum pumping power density and heat transfer density the opposite need to be done except for manifold height which should stay at minimum.

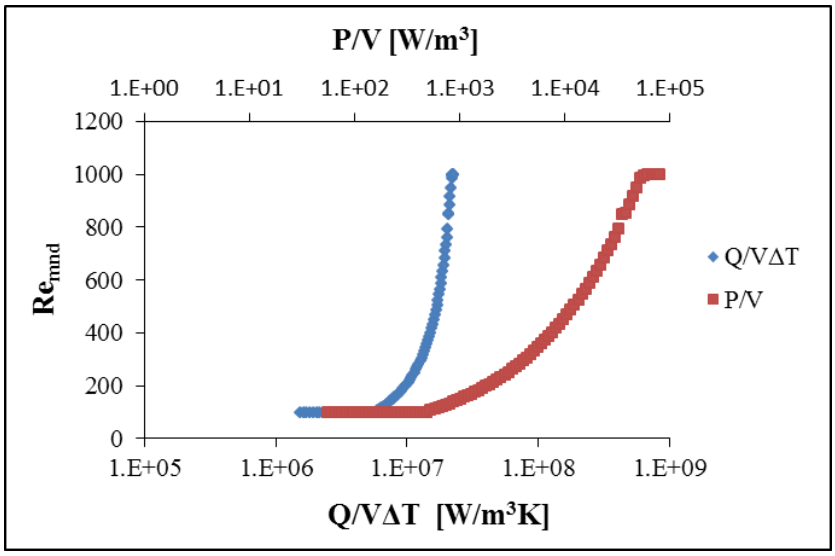

(a)

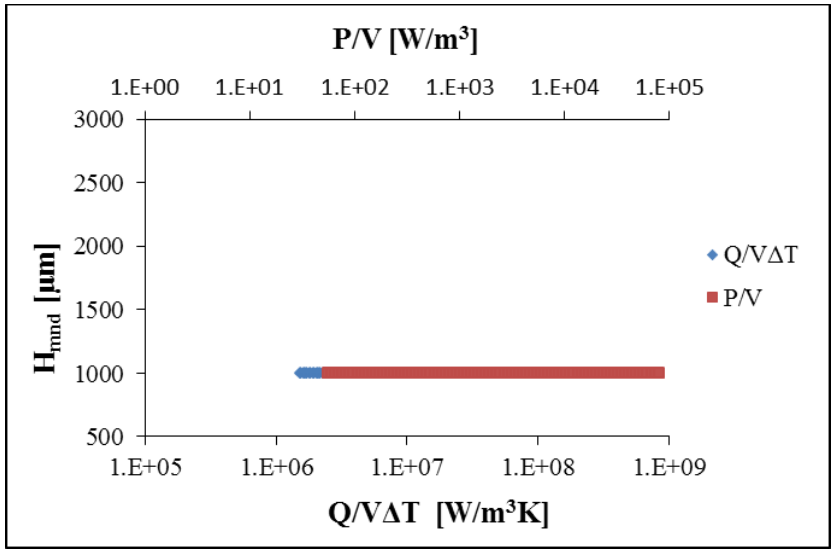

(b)

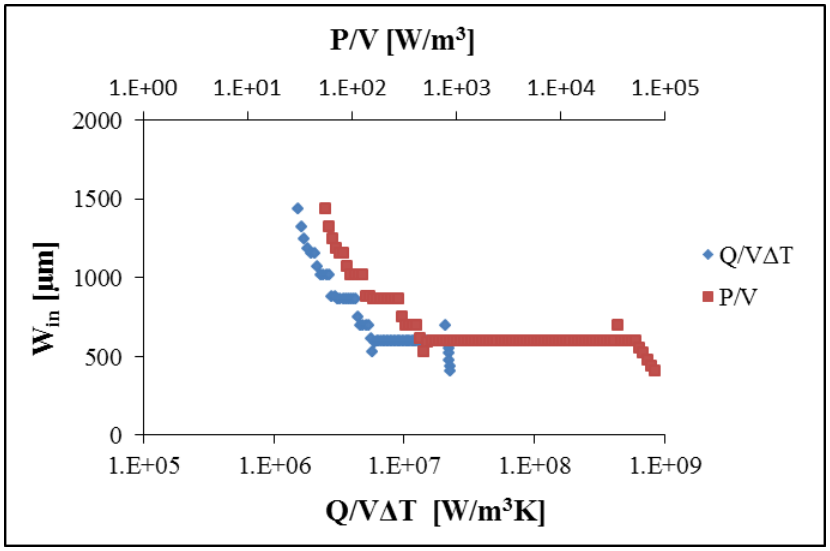

(c)

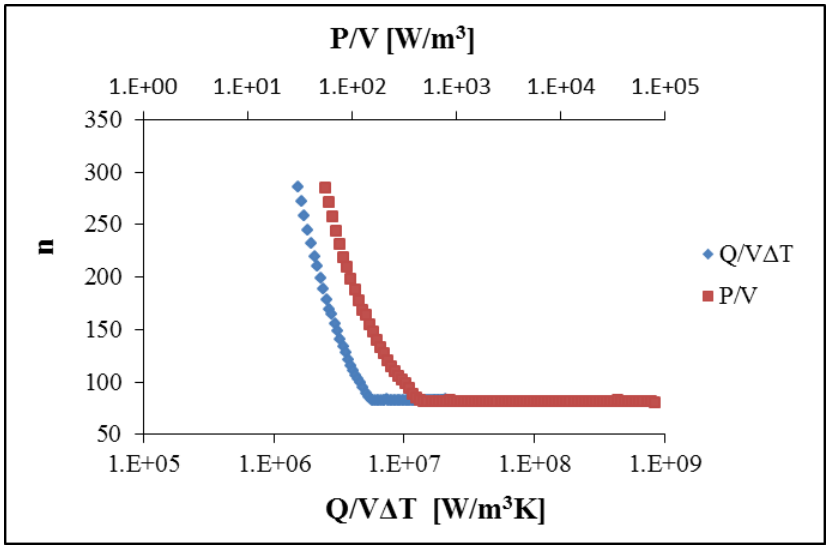

(d)

Figure 23: Variation of manifold optimum variables with respect to Q/VΔT and P/V for: (a) Re_{mnd}, (b) H_{mnd}, (c) W_{in}, and (d) n

5.5. Results Validation

5.5.1. Comparison with Full CFD Model

For validation of the pumping power density calculated using hybrid method and the assumptions made for the heat transfer density calculation, three complete SPSM models with 2,000,000 number of element each, like shown in Figure 24, were

created using Gambit mesh generator and solved numerically in Fluent. The three models represent three points randomly chosen from optimization results in Figure 19(b). The pumping power density and heat transfer density calculated from SPSM model CFD simulation are compared with their corresponding values which calculated from hybrid method. The comparison results are shown in Table 11.

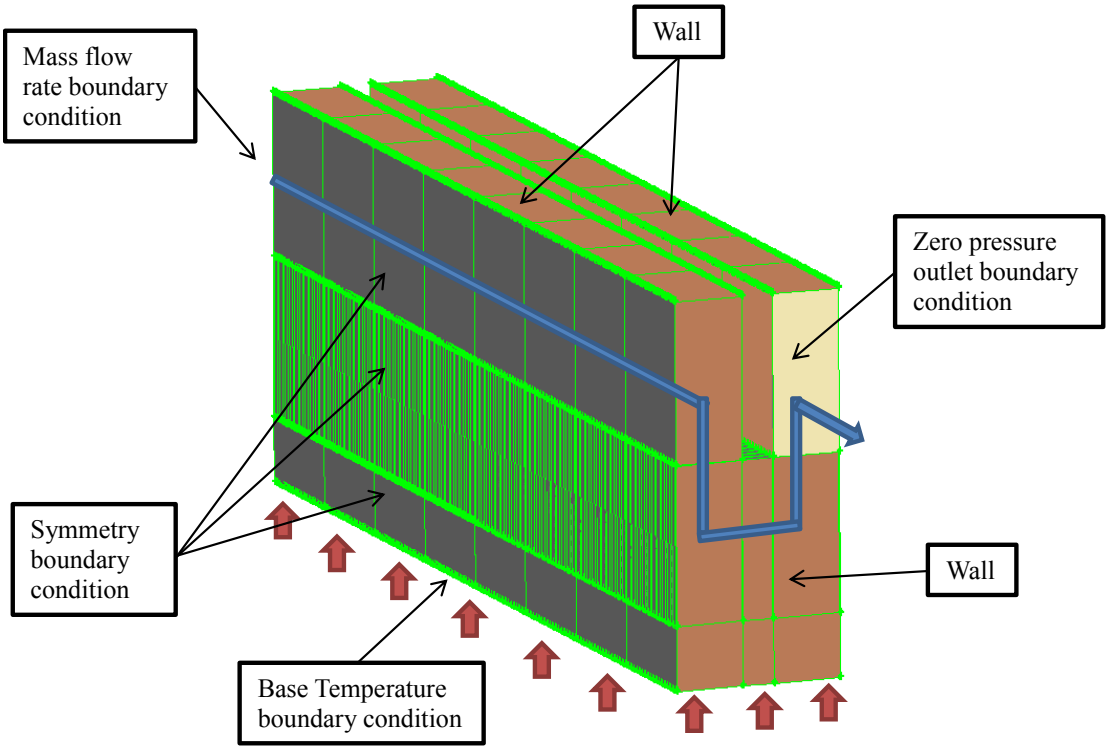

Figure 24: Schematic Drawing for SPSM model

Table 11: Comparison between hybrid method's solution and full model CFD solution

	Full model CFD solution		Hybrid method's solution		% Difference	
	P/V *[kW/m^3]*	*Q/VΔT* *[MW/m^3]*	*P/V* *[kW/m^3]*	*Q/VΔT* *[MW/m^3]*	*P/V* *[%]*	*Q/VΔT* *[%]*
Model 1	0.316	10.546	0.278	10.108	12.109	4.151
Model 2	7.265	39.343	6.551	38.255	9.827	2.765
Model 3	148.316	117.054	134.060	108.030	9.612	7.709
		Average deviation [%]			*10.516*	*4.875*

Based on the comparison results shown in Table 11, in average, the hybrid method's solution underestimate the full scale model CFD solution for pumping power by 10.52% and heat transfer density by 4.88%. Pumping power density has higher error compared to heat transfer density because pumping power calculation is more complex than heat transfer density due to addition pressure drop in manifold while for heat transfer density calculation, there is no heat transfer in the manifold thanks to the fact that the manifold is made of a very low thermal conductivity material. In addition, the hybrid method models the pressure and velocity distribution in manifold as 1-D fluid flow which neglects the effect of flow recirculations at the entrance of microchannels which can cause pumping power underestimation. However, in overall, the hybrid method can predict the pumping power density and heat transfer density of the single pass model with acceptable accuracy and significant lower computational costs.

5.5.2. Comparison with Experimental Work

For further validation of numerical modeling methodology developed under this work, the pumping power density and heat transfer density results are compared with experimental work. A manifold-microchannel plate heat exchanger design which had been fabricated and experimentally tested in our S2TS Laboratory by Andhare was used for this validation [58]. The manifold-microchannel model used for experimental is shown in the Figure 25 which consists of multiple manifold plate, shown in Figure 25(a), and multiple microchannel plates, shown in Figure 25(b), which stack together to form manifold-microchannel plate heat exchanger, shown in

Figure 25(c). The heat exchanger dimension is the same as the one used as baseline comparison with optimization results which is listed in Table 7.

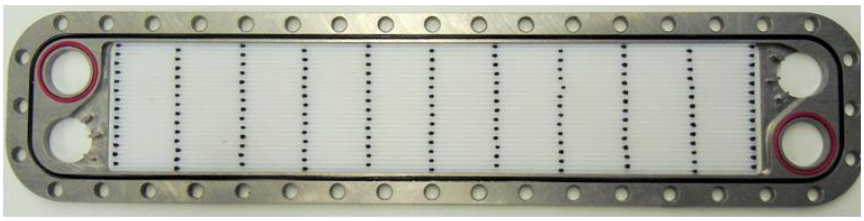

(a)

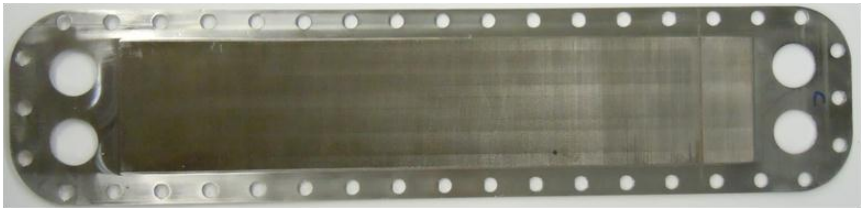

(b)

(c)

Figure 25: Component of the manifold-microchannel plate heat exchanger; (a) Manifold plate, (b) Microchannel plate, and (c) A stacked manifold-microchannel plate heat exchanger

Details of experimental setup and procedure can be found in [58]. The comparison results between the numerical solutions based on hybrid method solutions and experimental data are shown in Figure 26. As seen, in terms of general trend a good

agreement between numerical and experimental results is obtained. However, heat transfer density has been over predicted by numerical modeling when it is compared with experimental data by about 10.9% in average as shown in Figure 26(a). This might be attributed to imperfection in fabrication as there is a possibility that a gap between microchannel and manifold plates exists causing a portion of flow in manifold channel bypasses the microchannels and goes directly to adjacent manifold channel without contributing in heat transfer.

Looking at the pumping power density from numerical modeling and experimental test as shown in Figure 26(b), the numerical solution under predicts the experiment data by 36.8% in average. The main reason for this can be due to the fact that the numerical model only calculates pressure drop in the microchannel and manifold channel while the experimental measurement includes pressure drop in the input and exit pipes of the heat exchanger, pressure drop due to 90^{o} bend when the flow entering and exiting the heat exchanger, and pressure drop due to contraction and expansion when the flow is divided into multiple manifold or it is merged after exiting the manifolds in addition to the pressure drop in the manifold channel and microchannel. Considering all these differences between the numerical model and actual tests, the hybrid method developed here still has been able to predict the behavior of the manifold-microchannel plate heat exchanger in quite reasonable accuracy.

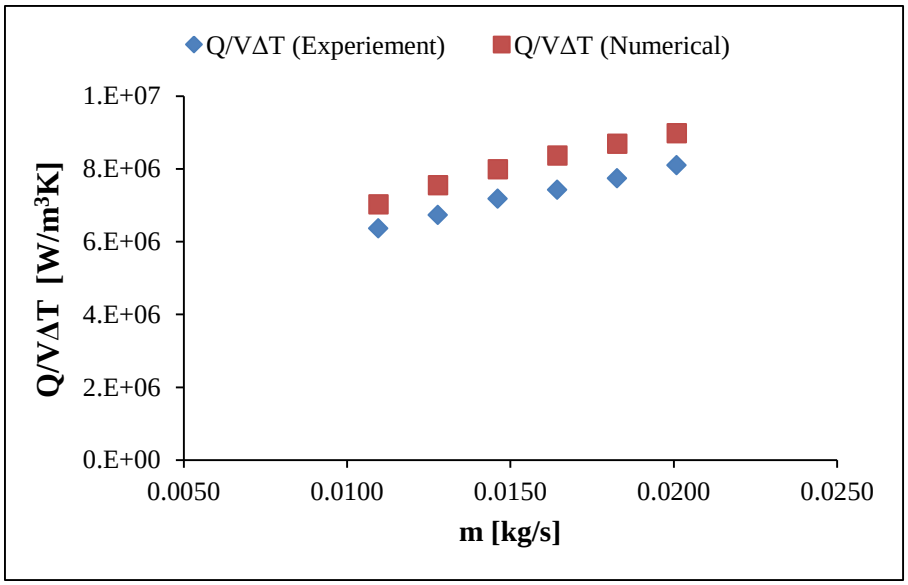

(a)

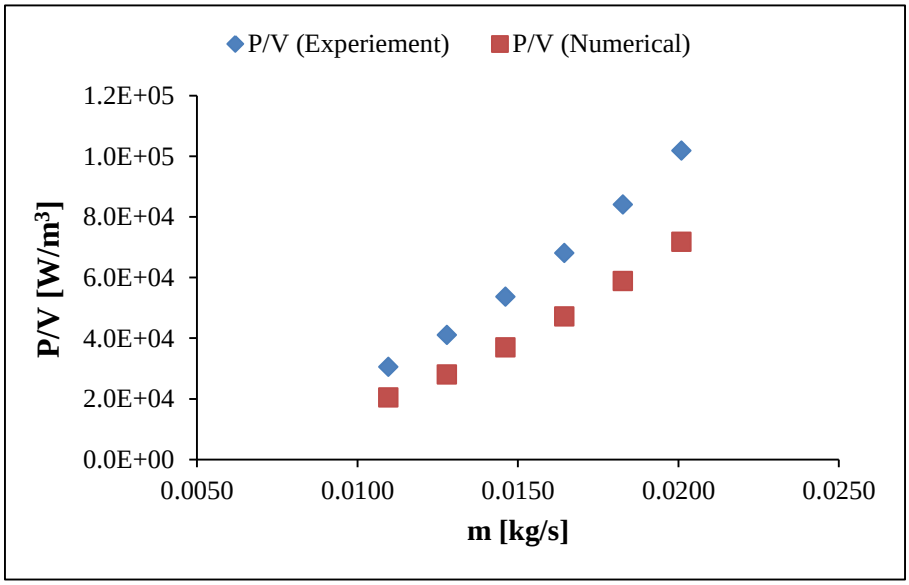

(b)

Figure 26: Comparison between hybrid method's solutions with experimental solution: (a) Q/VΔT and (b) P/V

5.6. Summary

The optimization results were discussed in detail in this chapter. First, grid independency and parametric studies were discussed. In addition to the manufacturability constrains, the results of the parametric study were used to select

the lower and upper limits of the geometrical and flow variables for the optimization process. A baseline design was presented and then the optimization results for two cases, that are manifold optimization and manifold-microchannel optimization, were discussed. The optimization results showed that the performance of the baseline design can be improved to a good extent. However, optimization of both manifold and microchannel can yield much better improvement compared to optimization of the manifold only. The optimization results of manifold-microchannel were compared to the Chevron plate heat exchanger and overall considerable advantage in performance of manifold-microchannel was noted with respect to both heat transfer and pumping power. In addition, the geometrical and flow parameter ranges which yield the optimum pumping power density and heat transfer density were discussed. Lastly, the hybrid method and the assumption used were verified by comparing the result with CFD simulation and experimental work. Both pumping power density and heat transfer density agree pretty well with CFD and experimental results which can validate the hybrid method developed and the assumption made.

Chapter 6: Conclusion and Future Work Recommendations

6.1. Conclusion

Manifold-microchannel heat exchangers have shown promising potentials for a variety of applications. However, the interrelationships among the various geometric and flow parameters in this type of heat exchanger are quite complex. Therefore, to fully utilize the potential that this type of heat exchanger can offer, it is important to find optimum range of operating parameters such that the best performance can be obtained. In this study, for the first time, a hybrid method was developed to predict the performance of a full scale manifold-microchannel heat exchanger with relatively low computational time. The method was based on solving full 3-D Navier-Stokes and energy equations in microchannel segment of the heat exchanger in combination with 1-D momentum and mass balance equations in the manifolds. For solving Navier-Stokes and energy equations a commercial code (ANSYS Fluent) was used. The CFD software was coupled with a MATLAB program to generate the CFD cases that could be evaluated. For fluid flow in manifolds the 1-D governing equations were formulated, programed and solved in Matlab environment. The objective was to determine the pumping power and heat transfer densities for any selected design. The verification of this hybrid method showed good agreement with the results obtained from direct CFD simulation of the full scale model and also from experimental results. The advantage of the hybrid method is that the computational time can be greatly reduced by the need to only model a single microchannel model and extend

the result into full heat exchanger rather than modeling the entire heat exchanger which will require much longer time to construct and simulate.

Next, an approximation based multi-objective optimization was performed base on this hybrid method. The optimization was carried out for two different cases: manifold optimization and combined manifold-microchannel optimization. The optimization results were able to predict the optimum configuration for both cases. The results of both cases were compared with the current prototype design that has been developed and fabricated in our lab. The optimization was able to calculate new designs which yield a better performance compared to the current design. This include being capable of reducing the pumping power density up to a factor of 48 without losing heat transfer density performance. Other design options which are capable of delivering up to four times the heat transfer density without any increase in pumping power density were also examined. In summary, to obtain maximum performance both manifold and microchannel components need to be optimized.

Comparison of the optimized manifold-microchannel with chevron-type plate heat exchanger, showed that manifold-microchannel overally offers superior performance in terms of Nu and f compared to chevron plate for three different chevron angles.

6.2. Future Work Recommendation

In this study, the numerical method is experimentally validated by comparing the results for the case of current manifold-microchannel heat exchanger available on the lab. For future work recommendations, one or more of the optimum geometries

determined under this study should be fabricated and tested for further validation of the numerical method.

Another recommendation is to implement genetic algorithm to solve multi-objective optimization instead of penalty method. Genetic algorithm is based on evolution algorithm instead of gradient based penalty method. Genetic algorithm has higher chance to achieve global optimum results compared to penalty method, although genetic algorithm computational time is typically several times higher than that of penalty method.

In another direction, the hybrid method can be further expanded for two phase flow in heat exchangers, such as condensers and evaporators in manifold-microchannel plate heat exchanger or other geometries. Two-phase flow regimes yield much higher heat transfer than single-phase flow. There is a lack of studies on two-phase flow in manifold-microchannel flat plate heat exchangers. Two-phase flow modeling consumes much more computational time than single-phase flow. Reduction of computational time by utilizing hybrid method can be a very useful contribution in this field. Moreover, the two-phase flow hybrid method than can be farther utilized for two-phase manifold-microchannel heat exchanger optimization, which usually impractical due to the long computational time for two-phase flow simulation, using the approximation assisted optimization method explained in section 4.2.

Another recommendation is to implement approximation-assisted optimization to optimize a straight manifold-microchannel heat exchanger. A straight manifold-microchannel can be either z-shape or u-shape, as shown in Figure 27. For this kind

of problems, the pressure drop between manifold 1 and 2 is much simpler to be calculated due to the absence of the U-shaped flow pattern in the microchannel like the case of manifold-microchannel plate heat exchanger. The pressure drop can be calculated using a developing or fully developed flow correlation for short or long channels, respectively.

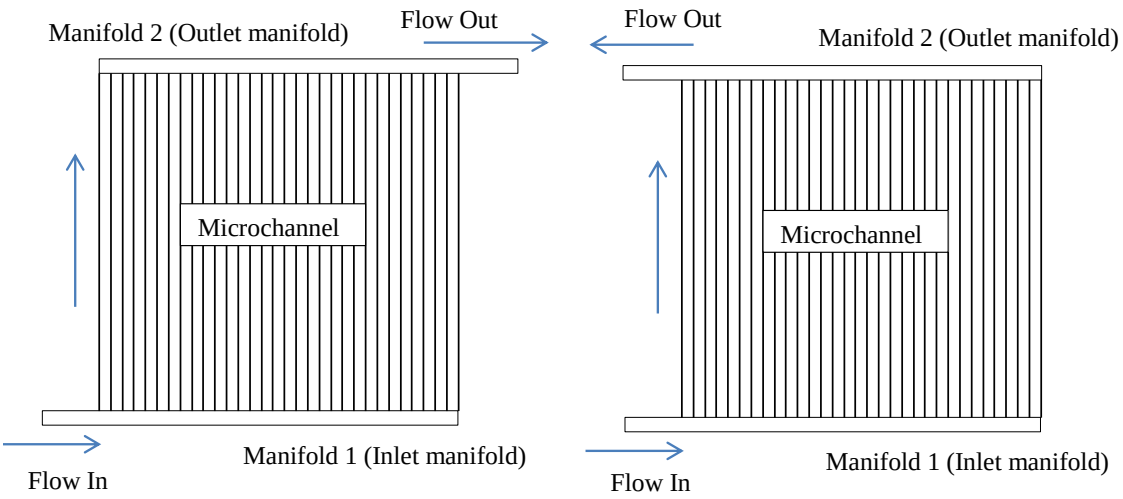

(a) z-shape heat exchanger **(b) u-shape heat exchanger**

Figure 27: z-shape and u-shape heat exchanger

Appendix A: Manifold Optimization Result Data

No.	Re_{mnd}	W_{in} [m]	H_{mnd} [m]	n	Q/VΔT [W/m^3K]	P/V [W/m^3]	F	ΔT [K]	V [mm^3]	Q [W]	P [W]	Δp [kPa]	h [kW/m^2K]
1.	100	1450	1000	295	1452361	52	0.027	258.38	1.24	0.0000010	0.007	0.014	258.38
2.	100	1430	1000	284	1540405	56	0.054	201.86	1.03	0.0000009	0.007	0.014	201.86
3.	100	1320	1000	271	1628610	61	0.060	183.90	1.13	0.0000008	0.007	0.015	183.90
4.	100	1240	1000	257	1730205	66	0.060	168.39	1.22	0.0000008	0.008	0.015	168.39
5.	100	1180	1000	243	1843344	72	0.057	154.95	1.28	0.0000009	0.008	0.016	154.95
6.	100	1150	1000	231	1947924	78	0.055	145.27	1.43	0.0000009	0.008	0.016	145.27
7.	100	1150	1000	218	2054898	84	0.050	137.09	1.54	0.0000009	0.008	0.017	137.09
8.	100	1070	1000	209	2165906	91	0.054	126.54	1.63	0.0000009	0.009	0.018	126.54
9.	100	1020	1000	198	2291835	99	0.053	116.99	1.71	0.0000009	0.009	0.018	116.99
10.	100	1020	1000	187	2414669	107	0.047	110.49	1.81	0.0000010	0.009	0.019	110.49
11.	100	1020	1000	177	2542472	116	0.047	104.58	1.96	0.0000010	0.010	0.020	104.58
12.	100	1010	1000	168	2673114	126	0.043	98.77	2.10	0.0000010	0.010	0.021	98.77
13.	100	880	1000	164	2812186	137	0.052	90.18	2.16	0.0000010	0.011	0.022	90.18
14.	100	880	1000	155	2957633	148	0.048	85.23	2.29	0.0000011	0.011	0.023	85.23
15.	100	870	1000	147	3106402	160	0.044	80.41	2.43	0.0000011	0.012	0.024	80.41
16.	100	870	1000	140	3258297	174	0.041	76.58	2.56	0.0000012	0.012	0.025	76.58
17.	100	870	1000	133	3414174	188	0.038	72.75	2.70	0.0000012	0.013	0.026	72.75
18.	100	870	1000	127	3573235	204	0.036	69.47	2.75	0.0000013	0.013	0.027	69.47
19.	100	870	1000	121	3736304	221	0.033	66.18	2.80	0.0000013	0.014	0.028	66.18
20.	100	870	1000	115	3902974	240	0.031	62.90	2.82	0.0000014	0.015	0.029	62.90

21.	100	870	1000	110	4073732	260	0.032	60.17	2.93	0.0000015	0.016	0.032	60.17
22.	100	870	1000	105	4248202	282	0.029	57.43	3.03	0.0000017	0.018	0.035	57.43
23.	100	750	1000	102	4445992	306	0.047	52.21	3.02	0.0000017	0.020	0.039	52.21
24.	100	700	1000	99	4656298	331	0.052	49.23	3.11	0.0000019	0.022	0.044	49.23
25.	100	700	1000	94	4877927	359	0.046	46.74	3.24	0.0000020	0.024	0.048	46.74
26.	100	700	1000	89	5102546	389	0.041	44.26	3.37	0.0000022	0.026	0.052	44.26
27.	100	700	1000	85	5336865	422	0.034	42.27	3.47	0.0000024	0.029	0.057	42.27
28.	100	610	1000	82	5598404	457	0.041	38.62	3.43	0.0000026	0.032	0.063	38.62
29.	100	530	1000	81	5747140	496	0.051	36.25	3.50	0.0000028	0.036	0.072	36.25
30.	108	590	1000	82	5990496	537	0.047	38.14	3.97	0.0000033	0.039	0.077	38.14
31.	113	600	1000	82	6205318	583	0.049	38.38	4.30	0.0000038	0.042	0.085	38.38
32.	117	600	1000	82	6418540	632	0.050	38.38	4.63	0.0000044	0.047	0.094	38.38
33.	122	600	1000	82	6637064	685	0.051	38.38	4.95	0.0000051	0.052	0.103	38.38
34.	127	600	1000	82	6861286	743	0.053	38.38	5.37	0.0000058	0.057	0.114	38.38
35.	132	600	1000	82	7090871	805	0.054	38.38	5.66	0.0000067	0.063	0.126	38.38
36.	138	600	1000	82	7324704	872	0.056	38.38	6.01	0.0000077	0.069	0.138	38.38
37.	144	600	1000	82	7565522	946	0.057	38.38	6.18	0.0000078	0.068	0.136	38.38
38.	149	600	1000	82	7813224	1025	0.058	38.38	6.55	0.0000090	0.075	0.151	38.38
39.	155	600	1000	82	8062915	1111	0.060	38.38	7.10	0.0000103	0.083	0.166	38.38
40.	162	600	1000	82	8319497	1205	0.061	38.38	7.53	0.0000119	0.091	0.183	38.38
41.	168	600	1000	82	8579711	1305	0.063	38.38	8.09	0.0000136	0.101	0.202	38.38
42.	175	600	1000	82	8846150	1415	0.065	38.38	8.57	0.0000156	0.111	0.223	38.38
43.	182	600	1000	82	9115586	1534	0.066	38.38	9.10	0.0000180	0.123	0.246	38.38
44.	190	600	1000	82	9389919	1662	0.068	38.38	9.63	0.0000206	0.135	0.271	38.38

45.	197	600	1000	82	9664565	1800	0.070	38.38	10.21	0.0000237	0.150	0.300	38.38
46.	205	600	1000	82	9953965	1954	0.070	38.38	10.82	0.0000272	0.165	0.331	38.38
47.	214	600	1000	82	10242444	2117	0.067	38.38	11.44	0.0000312	0.182	0.364	38.38
48.	222	600	1000	82	10533248	2295	0.075	38.38	12.09	0.0000358	0.201	0.403	38.38
49.	231	600	1000	82	10827814	2487	0.070	38.38	12.83	0.0000411	0.222	0.444	38.38
50.	241	600	1000	82	11125542	2695	0.061	38.38	13.53	0.0000472	0.244	0.489	38.38
51.	250	600	1000	82	11427476	2922	0.078	38.38	14.27	0.0000542	0.271	0.541	38.38
52.	260	600	1000	82	11732185	3167	0.076	38.38	15.13	0.0000622	0.299	0.597	38.38
53.	271	600	1000	82	12037773	3433	0.075	38.38	15.95	0.0000715	0.329	0.658	38.38
54.	282	600	1000	82	12345641	3721	0.072	38.38	16.81	0.0000821	0.363	0.726	38.38
55.	293	600	1000	82	12655895	4033	0.068	38.38	17.82	0.0000942	0.401	0.803	38.38
56.	305	600	1000	82	12966934	4371	0.066	38.38	18.83	0.0001082	0.443	0.885	38.38
57.	317	600	1000	82	13277727	4738	0.068	38.38	20.04	0.0001243	0.489	0.978	38.38
58.	330	600	1000	82	13588601	5135	0.071	38.38	21.11	0.0001426	0.539	1.078	38.38
59.	343	600	1000	82	13900260	5566	0.073	38.38	22.31	0.0001638	0.596	1.191	38.38
60.	357	600	1000	82	14211986	6032	0.074	38.38	23.42	0.0001880	0.657	1.314	38.38
61.	371	600	1000	82	14520285	6534	0.064	38.38	24.65	0.0002158	0.726	1.451	38.38
62.	385	600	1000	82	14831727	7082	0.072	38.38	25.89	0.0002478	0.803	1.606	38.38
63.	400	600	1000	82	15135491	7676	0.054	38.38	27.20	0.0002845	0.887	1.775	38.38
64.	416	600	1000	82	15455368	8320	0.057	38.38	28.53	0.0003267	0.980	1.960	38.38
65.	433	600	1000	82	15764972	9018	0.044	38.38	29.83	0.0003752	1.081	2.162	38.38
66.	450	600	1000	82	16078480	9783	0.057	38.38	31.51	0.0004306	1.194	2.388	38.38
67.	467	600	1000	82	16382647	10595	0.056	38.38	32.91	0.0004946	1.321	2.642	38.38
68.	486	600	1000	82	16689730	11485	0.054	38.38	34.71	0.0005678	1.457	2.915	38.38

69.	504	600	1000	82	16984255	12448	0.063	38.38	36.06	0.0006518	1.613	3.227	38.38
70.	524	600	1000	82	17291828	13491	0.093	38.38	37.85	0.0007486	1.782	3.564	38.38
71.	545	600	1000	82	17600883	14625	0.105	38.38	39.84	0.0008594	1.967	3.934	38.38
72.	566	600	1000	82	17884222	15853	0.114	38.38	42.04	0.0009868	2.175	4.350	38.38
73.	588	600	1000	82	18175604	17184	0.125	38.38	43.99	0.0011328	2.403	4.807	38.38
74.	610	600	1000	82	18453646	18625	0.135	38.38	45.67	0.0012140	2.483	4.965	38.38
75.	634	600	1000	82	18748575	20188	0.132	38.38	47.76	0.0013940	2.743	5.486	38.38
76.	658	600	1000	82	19031039	21884	0.133	38.38	50.14	0.0016002	3.034	6.068	38.38
77.	683	600	1000	82	19307955	23718	0.134	38.38	52.53	0.0018377	3.357	6.713	38.38
78.	709	600	1000	82	19582175	25708	0.134	38.38	54.75	0.0021102	3.713	7.426	38.38
79.	735	600	1000	82	19852656	27866	0.135	38.38	57.28	0.0024226	4.112	8.224	38.38
80.	763	600	1000	82	20118785	30207	0.135	38.38	59.65	0.0027806	4.546	9.092	38.38
81.	791	600	1000	82	20371434	32757	0.138	38.38	62.13	0.0031923	5.035	10.069	38.38
82.	848	690	1000	83	20600981	35482	0.114	41.03	68.80	0.0039196	5.459	10.918	41.03
83.	852	600	1000	82	20901588	38466	0.136	38.38	66.83	0.0042089	6.163	12.325	38.38
84.	883	600	1000	82	21157849	41692	0.136	38.38	69.59	0.0048327	6.828	13.655	38.38
85.	916	600	1000	82	21409506	45195	0.137	38.38	72.13	0.0055502	7.559	15.117	38.38
86.	949	600	1000	82	21656702	48987	0.137	38.38	75.07	0.0063697	8.373	16.746	38.38
87.	984	600	1000	82	21896460	53098	0.139	38.38	79.31	0.0073132	9.272	18.543	38.38
88.	995	560	1000	82	22095680	57584	0.155	37.42	80.87	0.0081898	10.531	21.063	37.42
89.	1000	520	1000	81	22224295	62385	0.165	36.01	81.00	0.0090488	11.883	23.765	36.01
90.	1000	480	1000	81	22345471	67622	0.177	35.06	81.02	0.0101156	13.642	27.285	35.06
91.	1000	440	1000	81	22454926	73287	0.189	34.12	81.31	0.0113128	15.681	31.361	34.12
92.	1000	410	1000	81	22538960	79486	0.200	33.41	81.66	0.0127133	17.997	35.994	33.41

Appendix B: Manifold Microchannel Optimization Result Data

No.	Re_{man}	H_{chn} [m]	α	W_{chn} [m]	W_{in} [m]	H_{mnd} [m]	n	Q/VΔT [W/m^3K]	P/V [W/m^3]	F	ΔT [K]	V [mm^3]	Q [W]	P [W]	Δp [kPa]	h [kW/m^2K]
1.	99	1000	0.10	60	2000	2499	293	240562	4	0.112	20	1809.57	8.71	0.0000072	0.065	0.938
2.	100	1000	0.10	60	1992	2499	282	254685	4	0.106	20	1735.83	8.84	0.0000075	0.066	0.993
3.	100	1000	0.13	60	1997	2499	297	306448	5	0.097	20	1447.65	8.87	0.0000067	0.059	1.195
4.	100	1000	0.16	60	1998	2500	298	363288	5	0.084	20	1212.33	8.81	0.0000061	0.054	1.417
5	100	985	0.19	59	2000	2500	300	413178	6	0.065	20	1033.64	8.54	0.0000057	0.050	1.605
6.	100	1000	0.24	60	2000	2499	300	491781	6	0.065	20	870.26	8.56	0.0000052	0.046	1.917
7.	100	1000	0.28	60	1994	2499	300	561581	7	0.060	20	768.07	8.63	0.0000051	0.045	2.190
8.	100	1000	0.33	60	1991	2499	300	645216	7	0.054	20	676.31	8.73	0.0000049	0.043	2.516
9.	100	1000	0.39	60	2000	2489	298	729971	8	0.050	20	594.79	8.68	0.0000047	0.042	2.839
10.	100	1000	0.44	60	1982	2248	296	816886	9	0.053	20	505.07	8.25	0.0000044	0.041	2.980
11.	100	1000	0.55	60	1994	2248	300	936639	10	0.050	20	443.02	8.30	0.0000043	0.040	3.417
12.	100	1000	0.65	60	1976	2233	295	1060998	11	0.040	20	387.84	8.23	0.0000041	0.039	3.855
13.	100	1000	0.82	60	1982	2020	300	1197539	12	0.059	20	325.46	7.80	0.0000037	0.037	4.096
14.	100	1000	0.99	60	1869	2020	300	1344371	13	0.060	20	280.77	7.55	0.0000035	0.036	4.598
15.	100	1000	1.24	60	1871	2010	300	1509871	14	0.059	20	251.81	7.60	0.0000035	0.036	5.149
16.	100	1000	1.50	60	1846	2010	298	1669394	15	0.058	20	228.23	7.62	0.0000034	0.036	5.693
17.	100	1000	1.82	60	1740	1931	292	1853360	17	0.066	20	193.51	7.17	0.0000032	0.035	6.174
18.	100	1000	1.96	60	1739	2008	281	1977244	18	0.049	20	185.61	7.34	0.0000034	0.036	6.738
19.	100	1000	2.00	60	1740	1736	268	2117527	20	0.068	20	161.87	6.86	0.0000032	0.037	6.641
20.	100	1000	2.00	60	1816	1750	246	2242361	22	0.056	20	154.55	6.93	0.0000034	0.038	7.063
21.	100	994	2.00	60	1874	1735	227	2436823	25	0.046	20	145.37	7.08	0.0000036	0.040	7.625
22.	100	994	1.94	60	1672	1736	215	2636340	29	0.051	20	126.79	6.68	0.0000037	0.043	8.252
23.	100	1000	2.00	60	1649	1700	195	2887589	33	0.047	20	111.48	6.44	0.0000037	0.044	8.952
24.	100	1000	1.94	60	1494	1735	183	3156959	38	0.044	20	98.80	6.24	0.0000038	0.046	9.897
25.	100	1000	2.00	60	1376	1736	170	3469993	44	0.022	20	85.21	5.91	0.0000037	0.048	10.882
26.	100	1000	2.00	60	1396	1500	153	3805452	50	0.037	20	71.72	5.46	0.0000036	0.050	11.036

27.	100	994	2.00	60	1375	1500	144	4100767	58	0.034	20	66.57	5.46	0.0000038	0.053	11.868
28.	100	1000	1.97	60	1300	1500	132	4438186	66	0.046	20	58.87	5.23	0.0000039	0.056	12.871
29.	100	1000	2.00	60	1200	1500	125	4831139	76	0.046	20	52.20	5.04	0.0000040	0.059	14.010
30.	100	1000	2.00	60	1200	1500	116	5200997	87	0.040	20	48.44	5.04	0.0000042	0.062	15.083
31.	100	1000	2.00	60	1200	1500	106	5603622	100	0.035	20	44.27	4.96	0.0000044	0.066	16.251
32.	100	1000	1.97	60	1165	1500	98	6028776	115	0.035	20	40.23	4.85	0.0000046	0.069	17.483
33.	100	1000	1.97	60	1035	1500	94	6454837	132	0.039	20	35.39	4.57	0.0000047	0.074	18.719
34.	100	1000	2.00	60	1037	1500	87	6995294	151	0.022	20	32.63	4.57	0.0000049	0.078	20.286
35.	100	994	2.00	60	885	1500	86	7368675	174	0.028	20	28.78	4.24	0.0000050	0.084	21.325
36.	100	983	1.98	59	843	1500	82	7830034	200	0.022	20	26.09	4.09	0.0000052	0.089	22.574
37.	117	984	1.97	59	1035	1302	87	8052164	204	0.038	20	29.83	4.80	0.0000061	0.089	21.628
38.	118	945	2.00	58	1035	1305	87	8530966	235	0.030	20	28.78	4.91	0.0000067	0.097	22.607
39.	123	978	2.00	59	1011	1227	80	9250300	269	0.047	20	26.02	4.81	0.0000070	0.101	24.097
40.	126	943	2.00	57	1035	1198	80	9813622	309	0.045	20	24.94	4.90	0.0000077	0.109	24.936
41.	136	937	1.97	57	1035	1060	80	10537922	355	0.063	20	23.65	4.98	0.0000084	0.117	25.259
42.	140	915	1.97	56	1035	1060	80	11163107	408	0.062	20	23.02	5.14	0.0000094	0.127	26.512
43.	144	885	1.97	55	1013	1061	80	11853528	468	0.058	20	21.99	5.21	0.0000103	0.138	27.808
44.	150	867	1.97	54	1014	1059	80	12546445	537	0.065	20	21.42	5.38	0.0000115	0.148	29.183
45.	154	854	1.97	54	920	1059	80	13299061	617	0.068	20	19.88	5.29	0.0000123	0.161	30.761
46.	159	838	1.97	53	885	1059	80	14096606	709	0.071	20	18.87	5.32	0.0000134	0.173	32.380
47.	165	817	1.97	52	885	1060	80	14904065	813	0.069	20	18.35	5.47	0.0000149	0.186	33.937
48.	171	800	1.97	51	885	1061	80	15755732	934	0.071	20	17.87	5.63	0.0000167	0.200	35.624
49.	175	777	2.00	50	885	1059	80	16717347	1072	0.068	20	17.24	5.76	0.0000185	0.216	37.380
50.	183	773	2.00	50	794	1059	80	17622253	1231	0.081	20	15.99	5.64	0.0000197	0.232	39.333
51.	191	758	1.97	49	788	1059	80	18597426	1413	0.076	20	15.57	5.79	0.0000220	0.249	41.230
52.	199	744	1.94	49	783	1059	80	19718078	1622	0.085	20	15.48	6.11	0.0000251	0.274	43.439
53.	206	729	1.97	48	778	1059	80	20778655	1862	0.092	20	14.92	6.20	0.0000278	0.293	45.464
54.	214	713	2.00	47	785	1060	80	21907737	2139	0.093	20	14.52	6.36	0.0000311	0.314	47.606
55.	229	710	1.94	47	785	1051	80	23222053	2456	0.098	20	14.59	6.78	0.0000358	0.340	50.183
56.	239	699	1.94	47	778	1046	80	24528169	2819	0.099	20	14.40	7.06	0.0000406	0.372	52.613

57.	249	681	1.96	46	760	999	80	26103848	3238	0.106	20	13.41	7.00	0.0000434	0.395	54.296
58.	262	670	1.94	45	785	1000	80	27500114	3716	0.105	20	13.38	7.36	0.0000497	0.424	56.925
59.	274	658	1.95	45	785	1000	80	29065056	4268	0.104	20	13.28	7.72	0.0000567	0.462	59.816
60.	287	648	1.94	44	778	1000	80	30512327	4900	0.111	20	12.87	7.85	0.0000631	0.493	62.489
61.	298	634	1.97	44	778	1000	80	32115017	5624	0.108	20	12.72	8.17	0.0000715	0.539	65.322
62.	316	634	1.94	44	730	1000	80	33737667	6457	0.123	20	12.26	8.27	0.0000792	0.577	68.622
63.	329	617	1.97	43	760	1000	80	35442535	7414	0.115	20	12.13	8.60	0.0000900	0.620	71.488
64.	343	605	1.97	42	760	1000	80	37165478	8514	0.117	20	11.78	8.76	0.0001003	0.663	74.517
65.	357	592	1.94	42	760	1000	80	38871794	9778	0.111	20	11.77	9.15	0.0001151	0.731	77.433
66.	372	584	1.94	41	734	1000	80	41047811	11221	0.120	20	11.18	9.18	0.0001255	0.776	81.439
67.	393	576	1.94	41	742	1000	80	42874164	12888	0.124	20	11.22	9.62	0.0001446	0.844	84.719
68.	400	556	1.97	40	757	1000	80	45219293	14795	0.110	20	10.92	9.87	0.0001615	0.918	88.449
69.	422	549	1.94	40	731	1000	80	46977206	16984	0.119	20	10.69	10.04	0.0001816	0.992	91.559
70.	442	549	1.94	40	681	1000	80	49313538	19507	0.134	20	10.22	10.08	0.0001993	1.071	96.112
71.	443	526	1.91	39	638	1000	80	51910311	22394	0.129	20	9.50	9.87	0.0002128	1.171	99.979
72.	449	502	1.94	38	640	1000	80	54775089	25713	0.112	20	9.11	9.98	0.0002343	1.271	104.182
73.	463	488	1.94	37	639	1000	80	57311663	29519	0.111	20	8.80	10.09	0.0002598	1.367	108.204
74.	410	441	1.97	35	521	1000	80	59503457	31633	0.102	20	7.16	8.52	0.0002264	1.449	109.546
75.	428	434	1.97	35	521	1000	80	62226389	36324	0.091	20	7.13	8.87	0.0002590	1.588	114.123
76.	456	428	1.84	35	521	1000	80	65333745	41699	0.060	20	7.28	9.51	0.0003034	1.747	119.430
77.	469	415	1.84	34	521	1000	80	68442204	47887	0.066	20	7.02	9.61	0.0003361	1.881	124.223
78.	496	410	1.82	34	522	1000	80	71327512	54987	0.094	20	7.03	10.03	0.0003867	2.045	129.103
79.	519	410	1.83	34	465	1000	80	74629786	63127	0.093	20	6.59	9.83	0.0004157	2.183	135.080
80.	549	408	1.82	33	465	1000	80	77718758	72456	0.126	20	6.40	9.94	0.0004635	2.299	140.516
81.	584	400	1.82	33	465	1000	80	80943437	83186	0.132	20	6.37	10.31	0.0005298	2.472	145.698
82.	624	400	1.84	33	466	1000	80	83845331	95534	0.132	20	6.35	10.65	0.0006068	2.648	150.922
83.	609	378	1.84	32	465	1000	80	87076112	109676	0.117	20	6.08	10.58	0.0006665	2.982	154.821
84.	636	368	1.83	32	465	1000	80	90672148	125931	0.116	20	6.05	10.98	0.0007624	3.269	160.308
85.	673	366	1.84	32	465	1000	80	93977090	144626	0.127	20	6.04	11.34	0.0008730	3.536	165.964
86.	673	347	1.94	31	465	1000	80	97807049	165981	0.129	20	5.68	11.11	0.0009427	3.819	170.869

87.	673	321	1.84	30	492	1000	80	103335406	190568	0.090	20	5.69	11.75	0.0010837	4.310	177.840
88.	673	305	1.84	29	465	1000	80	108069088	218882	0.095	20	5.28	11.41	0.0011560	4.682	184.258
89.	673	287	1.84	28	465	1000	80	112457523	251268	0.082	20	5.05	11.35	0.0012677	5.135	189.716
90.	673	287	1.84	27	465	1000	80	115524797	288482	0.078	20	4.87	11.24	0.0014035	5.685	194.890
91.	673	260	1.94	27	465	1000	80	119164235	331585	0.070	20	4.70	11.20	0.0015585	6.313	197.813
92.	706	253	1.95	27	465	1000	80	122225164	380564	0.069	20	4.67	11.42	0.0017781	6.860	202.038
93.	747	252	1.84	26	465	1000	80	126758239	436886	0.066	20	4.59	11.63	0.0020043	7.314	209.405
94.	812	264	1.84	26	450	1000	80	130841578	501335	0.061	20	4.54	11.88	0.0022765	7.715	217.720
95.	857	264	1.84	26	465	1000	80	134914779	575615	0.055	20	4.62	12.47	0.0026599	8.459	224.498
96.	879	264	1.84	25	465	1000	80	138432753	661175	0.052	20	4.44	12.30	0.0029378	9.108	230.352
97.	930	264	1.84	25	465	1000	80	142322982	759513	0.050	20	4.44	12.65	0.0033747	9.889	236.825
98.	990	264	1.84	25	465	1000	80	145724288	871365	0.050	20	4.44	12.95	0.0038717	10.656	242.485
99.	999	264	1.95	25	465	1000	80	148850979	1000748	0.056	20	4.35	12.96	0.0043582	11.890	247.688
100.	999	253	2.00	25	465	1000	80	151902877	1149243	0.073	20	4.29	13.03	0.0049297	13.449	251.095
101.	990	219	2.00	25	363	1000	80	160021076	1230258	0.084	20	3.71	11.86	0.0045592	13.494	259.074
102.	990	218	2.00	24	363	1000	80	164139481	1413619	0.082	20	3.56	11.67	0.0050261	14.868	265.578
103.	999	218	2.00	23	363	1000	80	167893136	1622060	0.068	20	3.41	11.44	0.0055269	16.207	271.651
104.	999	218	2.00	22	363	1000	80	171909603	1863911	0.063	20	3.26	11.21	0.0060748	17.815	278.150
105.	999	218	2.00	21	363	1000	80	176227960	2140471	0.058	20	3.11	10.96	0.0066591	19.528	285.137
106.	999	213	2.00	21	363	1000	80	180503195	2455277	0.049	20	3.10	11.20	0.0076148	22.330	291.152
107.	999	190	2.00	20	363	1000	80	185067304	2817739	0.032	20	2.91	10.78	0.0082042	24.057	294.257
108.	999	155	2.00	20	360	1000	80	190255721	3236210	0.022	20	2.84	10.79	0.0091789	26.975	295.848
109.	999	154	2.00	20	296	1000	80	194738354	3720583	0.044	20	2.60	10.11	0.0096579	29.786	302.623

Reference

[1] Wikipedia, 2010, "An interchangeable plate heat exchanger," http://en.wikipedia.org/wiki/File:Plate_heat_exchanger.png, Retrieve: 10/15/2012

[2] Wikipedia, 2011, "Schematic conceptual diagram of a plate and frame heat exchanger," http://en.wikipedia.org/w/index.php?title=File:Plate_frame_1.svg&page=1, Retrieve: 10/15/2012

[3] Wikipedia, 2005, "An individual plate for a heat exchanger," http://en.wikipedia.org/wiki/File:Plate_frame_2.png, Retrieve: 10/15/2012

[4] Cetegen, E., 2010, "Force Fed Microchannel High Heat Flux Cooling Utilizing Microgrooved Surface," Doctor, University of Maryland College Park.

[5] Maharudrayya, S., Jayanti, S., and Deshpande, A. P., 2005, "Flow distribution and pressure drop in parallel-channel configurations of planar fuel cells," Journal of power sources, 144(1), pp. 94-106.

[6] Brissenden, C. H., 1972, "PLATE HEAT EXCHANGERS THEN AND NOW," International Journal of Dairy Technology, 25(3), pp. 140-147.

[7] Hulbert, G., "Plate and frame heat exchangers," Geo-Heat Cent. Q. Bull.;(United States), 9(3).

[8] McKillop, A. A., and Dunkley, W. L., 1960, "Heat Transfer," Industrial & Engineering Chemistry, 52(9), pp. 740-744.

[9] Tauscher, R., and Mayinger, F., "Enhancement of Heat Transfer in a Plate Heat Exchanger by Turbulence Promotors."

[10] Abu-Khader, M. M., 2012, "Plate heat exchangers: Recent advances," Renewable and Sustainable Energy Reviews, 16(4), pp. 1883-1891.

[11] Muley, A., and Manglik, R. M., 1998, "Investigation of enhanced heat transfer in low Reynolds number flows in a plate heat exchanger," ASME HEAT TRANSFER DIV PUBL HTD, 361, pp. 295-302.

[12] Gherasim, I., Taws, M., Galanis, N., and Nguyen, C. T., 2011, "Heat transfer and fluid flow in a plate heat exchanger part I. Experimental investigation," International Journal of Thermal Sciences, 50(8), pp. 1492-1498.

[13] Gherasim, I., Galanis, N., and Nguyen, C. T., 2011, "Heat transfer and fluid flow in a plate heat exchanger. Part II: Assessment of laminar and two-equation turbulent models," International Journal of Thermal Sciences, 50(8), pp. 1499-1511.

[14] Khan, T. S., Khan, M. S., Chyu, M. C., and Ayub, Z. H., 2010, "Experimental investigation of single phase convective heat transfer coefficient in a corrugated plate heat exchanger for multiple plate configurations," Applied Thermal Engineering, 30(8), pp. 1058-1065.

[15] Luan, Z., Zhang, G., Tian, M., and Fan, M., 2008, "Flow resistance and heat transfer characteristics of a new-type plate heat exchanger," Journal of Hydrodynamics, Ser. B, 20(4), pp. 524-529.

[16] Durmuş, A., Benli, H., Kurtbaş, İ., and Gül, H., 2009, "Investigation of heat transfer and pressure drop in plate heat exchangers having different surface profiles," International Journal of Heat and Mass Transfer, 52(5), pp. 1451-1457.

[17] Ayub, Z. H., 2003, "Plate heat exchanger literature survey and new heat transfer and pressure drop correlations for refrigerant evaporators," Heat transfer engineering, 24(5), pp. 3-16.

[18] Tuckerman, D. B., and Pease, R. F., 1997, "Microcapiliary Thermal Interface Technology for VLSI Packaging," Proc. Symposium on VLSI Technology, IEEE, pp. 60-61.

[19] Phillips, R. J., 1990, "Microchannel Heat Sinks," *Advances in Thermal Modeling of Electronic Components and Systems*New York, pp. 109–184.

[20] Hassan, I., Phutthavong, P., and Abdelgawad, M., 2004, "Microchannel heat sinks: an overview of the state-of-the-art," Microscale Thermophysical Engineering, 8(3), pp. 183-205.

[21] Khan, M. G., and Fartaj, A., 2010, "A review on microchannel heat exchangers and potential applications," International Journal of Energy Research, 35(7), pp. 553-582.

[22] Harpole, G. M., and Eninger, J. E., 1991 "Micro-channel heat exchanger optimization," Seventh IEEE SEMI-THERM™ Symposium, IEEE, pp. 59-63.

[23] Copeland, D., Behnia, M., and Nakayama, W., 1997, "Manifold microchannel heat sinks: isothermal analysis," Components, Packaging, and Manufacturing Technology, Part A, IEEE Transactions on, 20(2), pp. 96-102.

[24] Poh, S. T., and Ng, E. Y. K., 1999, "Investigative study of manifold microchannel heat sinks for electronic cooling design," Journal of Electronics Manufacturing, 9(02), pp. 155-166.

[25] Poh, S. T., and Ng, E. Y. K., 1998, "Heat transfer and flow issues in manifold microchannel heat sinks: a CFD approach," Proceedings of 2nd Electronics Packaging Technology Conference, IEEE, pp. 246-250.

[26] Ryu, J. H., Choi, D. H., and Kim, S. J., 2003, "Three-dimensional numerical optimization of a manifold microchannel heat sink," International journal of heat and mass transfer, 46(9), pp. 1553-1562.

[27] Kim, Y. H., Chun, W. C., Kim, J. T., Pak, B. C., and Baek, B. J., 1998, "Forced air cooling by using manifold microchannel heat sinks," Journal of Mechanical Science and Technology, 12(4), pp. 709-718.

[28] Wang, Y., and Ding, G. F., 2008, "Numerical analysis of heat transfer in a manifold microchannel heat sink with high efficient copper heat spreader," Microsystem Technologies, 14(3), pp. 389-395.

[29] Kermani, E., Dessiatoun, S., Shooshtari, A., and Ohadi, M. M., "Experimental investigation of heat transfer performance of a manifold microchannel heat sink for cooling of concentrated solar cells," IEEE, pp. 453-459.

[30] Escher, W., Brunschwiler, T., Michel, B., and Poulikakos, D., 2010, "Experimental investigation of an ultrathin manifold microchannel heat sink for liquid-cooled chips," Journal of Heat Transfer, 132, pp. 081402-081401.

[31] Boteler, L., Jankowski, N., McCluskey, P., and Morgan, B., 2012, "Numerical investigation and sensitivity analysis of manifold microchannel coolers," International Journal of Heat and Mass Transfer.

[32] Ryu, J. H., Choi, D. H., and Kim, S. J., 2002, "Numerical optimization of the thermal performance of a microchannel heat sink," International Journal of Heat and Mass Transfer, 45(13), pp. 2823-2827.

[33] Gopinath, D., Joshi, Y., and Azarm, S., 2005, "An integrated methodology for multiobjective optimal component placement and heat sink sizing," Components and Packaging Technologies, IEEE Transactions on, 28(4), pp. 869-876.

[34] Sharma, C. S., Zimmermann, S., Tiwari, M. K., Michel, B., and Poulikakos, D., 2011, "Optimal thermal operation of liquid-cooled electronic chips," International Journal of Heat and Mass Transfer.

[35] Türkakar, G., and Okutucu-Özyurt, T., 2012, "Dimensional optimization of microchannel heat sinks with multiple heat sources," International Journal of Thermal Sciences.

[36] Amanifard, N., Nariman-Zadeh, N., Borji, M., Khalkhali, A., and Habibdoust, A., 2008, "Modelling and Pareto optimization of heat transfer and flow coefficients in microchannels using GMDH type neural networks and genetic algorithms," Energy Conversion and Management, 49(2), pp. 311-325.

[37] Husain, A., and Kim, K. Y., 2008, "Optimization of a microchannel heat sink with temperature dependent fluid properties," Applied Thermal Engineering, 28(8), pp. 1101-1107.

[38] Husain, A., and Kim, K. Y., 2010, "Enhanced multi-objective optimization of a microchannel heat sink through evolutionary algorithm coupled with multiple surrogate models," Applied Thermal Engineering, 30(13), pp. 1683-1691.

[39] Saleh, K., Abdelaziz, O., Aute, V., Radermacher, R., and Azarm, S., 2010, "Microchannel Approximation Assisted Design Optimization and CFD Verification."

[40] Shah, R. K., and London, A. L., 1978, Laminar flow forced convection in ducts: a source book for compact heat exchanger analytical data, Academic press New York.

[41] Fluent-Inc, 2012, "FLUENT 6.3 Documentation," http://hpce.iitm.ac.in/website/Manuals/Fluent_6.3/fluent6.3/help/index.htm.

[42] Kim, H. K., Chong, J. K., and Park, K. Y., 2009, "Approximation model-assisted optimization technique to improve capacitive current interrupting performance of gas circuit breaker," Magnetics, IEEE Transactions on, 45(3), pp. 1574-1577.

[43] Farhang-Mehr, A., Azarm, S., Diaz, A., and Ravisekar, A., "Bayesian approximation-assisted optimization applied to crashworthiness design of a pickup truck," ASME.

[44] Abdelaziz, O., Aute, V., Azarm, S., and Radermacher, R., 2010, "Approximation-Assisted Optimization for Novel Compact Heat Exchanger Designs," HVAC&R Research, 16(5), pp. 707-728.

[45] Abdelaziz, O. A., 2009, "Development of Multi-Scale, Multi-Physics, Analysis Capability and its Application to Novel Heat Exchanger Design and Optimizaiton."

[46] Aute, V., Abdelaziz, O., Azarm, S., and Radermacher, R., 2008, "Cross-validation Based Single Response Adaptive Design of Experiments," 12th AIAA/ISSMO Multidisciplinary Analysis and Optimization Conference.

[47] Li, M., Li, G., and Azarm, S., 2008, "A kriging metamodel assisted multi-objective genetic algorithm for design optimization," Journal of Mechanical Design, 130(3), p. 31401.

[48] Mistree, F., Korte, J. J., Mauery, T. M., and Simpson, T. W., 2012, "Kriging models for global approximation in simulation-based multidisciplinary design optimization," AIAA journal, 39(12).

[49] Simpson, T. W., Martin, J. D., Booker, A. J., Giunta, A. A., Haftka, R. T., Renaud, J. E., and Kleijnen, J. P. C., 2005, "Use of kriging models to approximate deterministic computer models," AIAA journal, 43(4), pp. 853-863.

[50] Lophaven, S. N., Nielsen, H. B., and Søndergaard, J., 2002, DACE: A Matlab kriging toolbox, Citeseer.

[51] Sarker, R., and Ray, T., 2009, "An improved evolutionary algorithm for solving multi-objective crop planning models," Computers and Electronics in Agriculture, 68(2), pp. 191-199.

[52] Ziolkowski, M., and Gratkowski, S., 2009, "Genetic algorithm-based multi-objective optimization of an exciter for magnetic induction tomography," COMPEL: The International Journal for Computation and Mathematics in Electrical and Electronic Engineering, 28(5), pp. 1121-1128.

[53] Takahama, T., and Sakai, S., 2009, "Efficient Constrained Optimization by the ε Constrained Differential Evolution Using an Approximation Model with Low Accuracy," Transactions of the Japanese Society for Artificial Intelligence, 24, pp. 34-45.

[54] Ishizuka, Y., and Aiyoshi, E., 1992, "Double penalty method for bilevel optimization problems," Annals of Operations Research, 34(1), pp. 73-88.

[55] Fletcher, R., "An l 1 penalty method for nonlinear constraints," Society for Industrial & Applied, p. 26.

[56] Hu, X. M., and Ralph, D., 2004, "Convergence of a penalty method for mathematical programming with complementarity constraints," Journal of Optimization Theory and Applications, 123(2), pp. 365-390.

[57] Lillo, W. E., Loh, M. H., Hui, S., and Zak, S. H., 1993, "On solving constrained optimization problems with neural networks: A penalty method approach," Neural Networks, IEEE Transactions on, 4(6), pp. 931-940.

[58] Andhare, R. S., Expected 2013, "Experimental Heat Transfer and Pressure Drop Characteristic of A Single Phase Manifold-Microchannel Heat Exchanger," Master, University of Maryland College Park.

[59] Thonon, B., "Design method for plate evaporators and condensers," MECHANICAL ENGINEERING PUBLICATIONS LIMITED, pp. 37-50.

[60] Kovalenko, L. M., and Maslov, A. M., 1970, "Soviet Plate Heat Exchangers," Konservnaya I Ovoshchesushil Naya Promyshlennost (in Russian)(7), pp. 15-17.

[61] Cooper, A., 1974, "Recover more heat with plate heat exchangers," The Chemical Engineer, 285, pp. 280-285.

[62] Kumar, H., "The plate heat exchanger: construction and design," pp. 1275-1288.

[63] Focke, W. W., Zachariades, J., and Olivier, I., 1985, "The effect of the corrugation inclination angle on the thermohydraulic performance of plate heat exchangers," International Journal of Heat and Mass Transfer, 28(8), pp. 1469-1479.